Knudsen effusion mass spectrometry: Current and future approaches

Nathan Jacobson, Jean-yves Colle, Valentina Stolyarova, Torsten Markus, Ioana Nuta

Received: 12 October 2023 | Revised: 7 February 2024 | Accepted: 7 March 2024

DOI: 10.1002/rcm.9744

REVIEW ARTICLE

Rapid Communications in Mass Spectrometry WILEY

Knudsen effusion mass spectrometry: Current and future approaches

Nathan S. Jacobson[1] | Jean-Yves Colle[2] | Valentina Stolyarova[3,4] | Torsten Markus[5] | Ioana Nuta[6]

[1]Material and Structures Division, NASA Glenn Research Center/HX5, LLC, Cleveland, Ohio, USA

[2]European Commission, Joint Research Centre (JRC), Karlsruhe, Germany

[3]Saint Petersburg State University, Saint Petersburg, Russian Federation

[4]Institute of Silicate Chemistry of the Russian Academy of Sciences, Saint Petersburg, Russian Federation

[5]Institute for Materials Science and Engineering, Mannheim University of Applied Sciences, Mannheim, Germany

[6]University Grenoble Alpes, CNRS, Grenoble INP-SIMaP, Grenoble, France

Correspondence
N. S. Jacobson, Material and Structures Division, NASA Glenn Research Center/HX5, LLC, Cleveland, OH 44135, USA.
Email: njacobson248@gmail.com

Jean-Yves Colle, European Commission, Joint Research Centre (JRC), Karlsruhe, Germany.
Email: jean-yves.colle@ec.europa.eu

Funding information
NASA Transformative Tools and Technologies

Rationale: Knudsen effusion mass spectrometry (KEMS) has been a powerful tool in physical chemistry since 1954. There are many excellent reviews of the basic principles of KEMS in the literature. In this review, we focus on the current status and potential growth areas for this instrumental technique.

Methods: We discuss (1) instrumentation, (2) measurement techniques, and (3) selected novel applications of the technique. Improved heating methods and temperature measurement allow for better control of the Knudsen cell effusive source. Accurate computer models of the effusive beam and its introduction to the ionizer allow optimization of such parameters as sensitivity and removal of background signals. Computer models of the ionizer allow for optimized sensitivity and resolution. Additionally, data acquisition systems specifically tailored to a KEMS system permit improved quantity and quality of data.

Results: KEMS is traditionally utilized for thermodynamic measurements of pure compounds and solutions. These measurements can now be strengthened using first principles and model-based computational thermochemistry. First principles can be used to calculate accurate Gibbs energy functions (*gefs*) for improving third law calculations. Calculated enthalpies of formation and dissociation energies from ab initio methods can be compared to those measured using KEMS. For model-based thermochemistry, solution parameters can be derived from measured thermochemical data on metallic and nonmetallic solutions. Beyond thermodynamic measurements, KEMS has been used for many specific applications. We select examples for discussion: measurements of phase changes, measurement/control of low-oxygen potential systems, thermochemistry of ultrahigh-temperature ceramics, geological applications, nuclear applications, applications to organic and organometallic compounds, and thermochemistry of functional room temperature materials, such as lithium ion batteries.

Conclusions: We present an overview of the current status of KEMS and discuss ideas for improving KEMS instrumentation and measurements. We discuss selected KEMS studies to illustrate future directions of KEMS.

1 | INTRODUCTION

Knudsen effusion mass spectrometry (KEMS) has long been an important experimental tool in physical chemistry. The Knudsen cell is a small enclosure in which a near-condensed phase/vapor equilibria is established. A well-defined orifice directs a molecular beam (nearly collision free, directed flow), representative of the vapor at low pressures, to a mass spectrometer operating at pressures near the ultrahigh vacuum (UHV) range. This technique has found numerous applications in thermochemistry, geology, metallurgy, ceramics, nuclear materials, and a range of other fields.[1–11] Although the use of this technique peaked in the 1960s–1970s, the need for KEMS data continues today. There are currently about 10 active groups using this method. At the time of writing, the authors are aware of several groups in Europe, several in Russia, one in the United States, and one in India.

There are many excellent reviews on the KEMS technique[1–11] that provide the relevant background and explain the development of the technique. We shall not repeat such information here but rather focus on new and fundamental developments in the field and the importance of the technique to current and future research in the physical sciences.

We first discuss instrumentation in a typical KEMS setup. We pay particular attention to the advances in sample introduction, which include accurate positioning of the Knudsen cell, precise temperature measurements, attaining equilibrium in the cell, and molecular beam collimation. Advances in the actual instrumentation include computer simulation of the molecular beam into the ionizer and the actual ionizer, which allow optimization of the instrument geometry and tuning of the ionizer for improved sensitivity and resolution. Overall system performance is also improved with advanced data acquisition systems, which allow better instrument control and signal averaging/signal collection.

Next, we discuss actual measurements obtained using KEMS, highlighting several areas for potential growth of this technique. Traditionally, KEMS has been used for precision thermochemical measurements of both pure compounds and solutions. We review these measurements as well as the methods used to make them. An exciting growth area for KEMS is the integration of these methods with computational chemistry. Computational chemistry can be divided into two categories: first principles-based calculations (which are most often applied to gaseous species) and model-based solution calculations (which are most often applied to complex condensed-phase systems with many components). Bond energy measurements using KEMS can verify or refute ab initio calculations. Gibbs energy functions (*gefs*) derived from first principles allow more accurate KEMS determinations of the enthalpy of formation via the third law. In regard to model-based computations of solutions, the KEMS measurements can directly provide the constants for the fitted polynomials.

As previously noted, KEMS has been used in such diverse fields as thermochemistry, geology, ceramics, metallurgy, nuclear materials, and more recently organic chemistry. We discuss some selected areas that are currently of interest. These include phase change measurements, control/measurement in processes with low $P(O_2)$, thermochemistry of ultrahigh-temperature materials, applications to geochemistry, cosmochemistry, nuclear applications, thermodynamics of organic and organometallic compounds, and thermodynamics of lithium ion batteries.

2 | INSTRUMENTATION

Figure 1 shows the basic layout of a KEMS instrument. We shall discuss each component as it relates to the unique case of effusate vapor sampling from a Knudsen cell.

1. Vapor source (Knudsen cell) and furnace.
2. Molecular beam sampling and shutter design.
3. Ionizer and subsequent ion focusing plate assembly. Due to the high temperatures, electron impact is nearly universally used in KEMS. The classic design has remained unchanged for many years. However, as will be discussed, there is now room for much improvement in the ionizer and focusing plate assembly.
4. Ion sorter/mass filter—could be magnetic, electrostatic, or time of flight. Generally, a magnetic sector is preferred due to its high resolution and lack of mass discrimination. However, modern quadrupole mass filters exhibit much better resolution and limited mass discrimination compared to their early counterparts. Most of the active KEMS groups use magnetic sector instruments; however, there are several using quadrupole instruments.
5. Detector—involves an electron multiplier with discrete dynodes or a continuous dynode channeltron. Both types are typically used with a Faraday cup for comparison to the raw signal or in the case of high signals when using pulse counting.
6. Vacuum system—great strides have been made in vacuum technology in recent years. It is possible to build an entirely oil-free system at a reasonable price now. A clean vacuum system leads to less background peaks, lower intensities for the background peaks that remain, and clarity in identifying signals from the Knudsen cell.

The heart of any KEMS machine is the Knudsen cell and furnace, which generates the vapor to examine. We shall discuss this first.

2.1 | Knudsen cell and furnace flange

2.1.1 | Knudsen cells

As described in other publications,[3,12] the Knudsen cell is a small enclosure in which, ideally, a condensed phase equilibrates with its vapor. A small, well-defined orifice allows a representative small portion of the vapor to escape under vacuum as a molecular beam that is directed into the mass spectrometer. The required condition is that the escaping vapor does not perturb the vapor phase/condensed

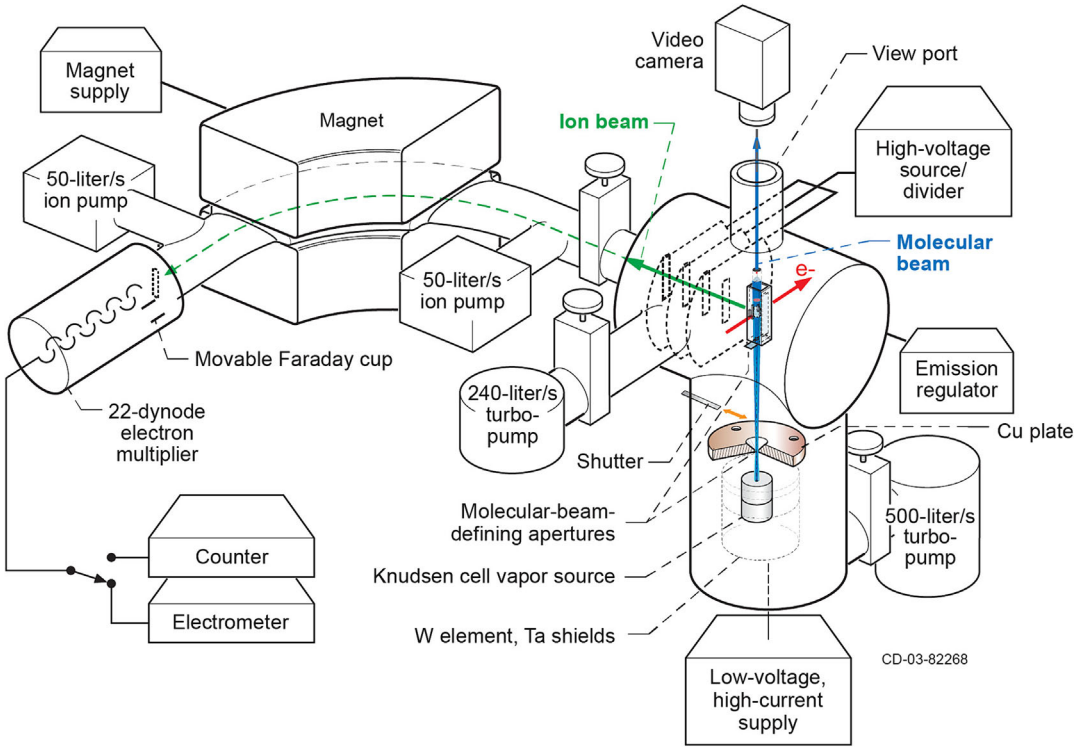

FIGURE 1 NASA Glenn magnetic sector KEMS (Knudsen effusion mass spectrometry) instrument. [Color figure can be viewed at wileyonlinelibrary.com]

phase equilibrium in the cell. This is generally indicated by the relationship:

$$BW_B/S \leq 10^{-2} \quad (1)$$

Here B is the surface area of the cell orifice; W_B is the Clausing or transmission factor for the cell orifice,[13] which will be discussed later; and S is the vaporizing surface area of the condensed phase sample that may be often reduced to the cell section.

Different types of cells are shown in Figure 2. The cell should ideally be chemically inert to the contained condensed phase and the vapor; however, in practice there is likely to be some reaction, particularly at high temperatures. For some sample/cell systems, material interactions above a certain temperature impose a use limit. A wide range of cell materials have been used, including refractory metals, refractory oxides, graphite, and various ceramics. Improved processing and machining methods allow the possibility of more exotic cell materials and cell liners. Sample/cell material chemical reactions are the most obvious concern, but structural issues may also be a problem. For example, liquid Au in Al_2O_3 appears to penetrate only grain boundaries, and the system performs well for several runs until the cell walls are weakened. Another approach is to use the cell as a reactant. For example, a Mo cell has been used to study Mo (powder) mixed with rare-earth silicates.[14] Additionally, a Hf liner has been used to study the reaction of Hf and HfO_2.[15] Silicon in dense graphite forms a compact SiC layer inside the cell, which limits further reaction.[16]

There are many variations in the simple cell in Figure 2A,B. These include a gas-leak cell (Figure 2C),[17] a multiple cell (Figure 2D),[18,19] an electrochemical cell (Figure 2E),[20] and a tandem cell with a cracker (Figure 2F).[21] The gas-leak cell allows another vapor or gas to be introduced to the cell and reacted with the contained sample, and the resulting gas species can be studied. The multiple cell consists of two or more cells in an isothermal block that can be translated in and out of the sampling region to compare a measured ion intensity in a sample under study to a reference ion intensity in a short time period; it is an instantaneous calibration. This will be discussed in detail later in this paper. An electrochemical cell allows the chemical potential of a species (e.g., O_2 or S_2) to be fixed above the sample.[20] The tandem cell with a cracker is a specially designed cell for studying reactions of air-sensitive organometallics. This will be discussed later in this paper.

2.1.2 | Furnace and temperature measurements

A variety of methods have been used to heat Knudsen cells. Figure 3A,B shows resistance heating: Figure 3A shows the system at NASA Glenn, USA[18]; Figure 3B shows the system at SIMaP, France[19]; Figure 3C shows electron bombardment at Saint Petersburg State University, Russia; and Figure 3D shows laser heating at JRC Karlsruhe, Germany. It is essential that the cell is heated uniformly—thermodynamic measurements require a constant temperature throughout the cell. The challenge is to design a compact furnace with a tight heat shield pack, in which the cell orifice is as close as possible to the ionizer.

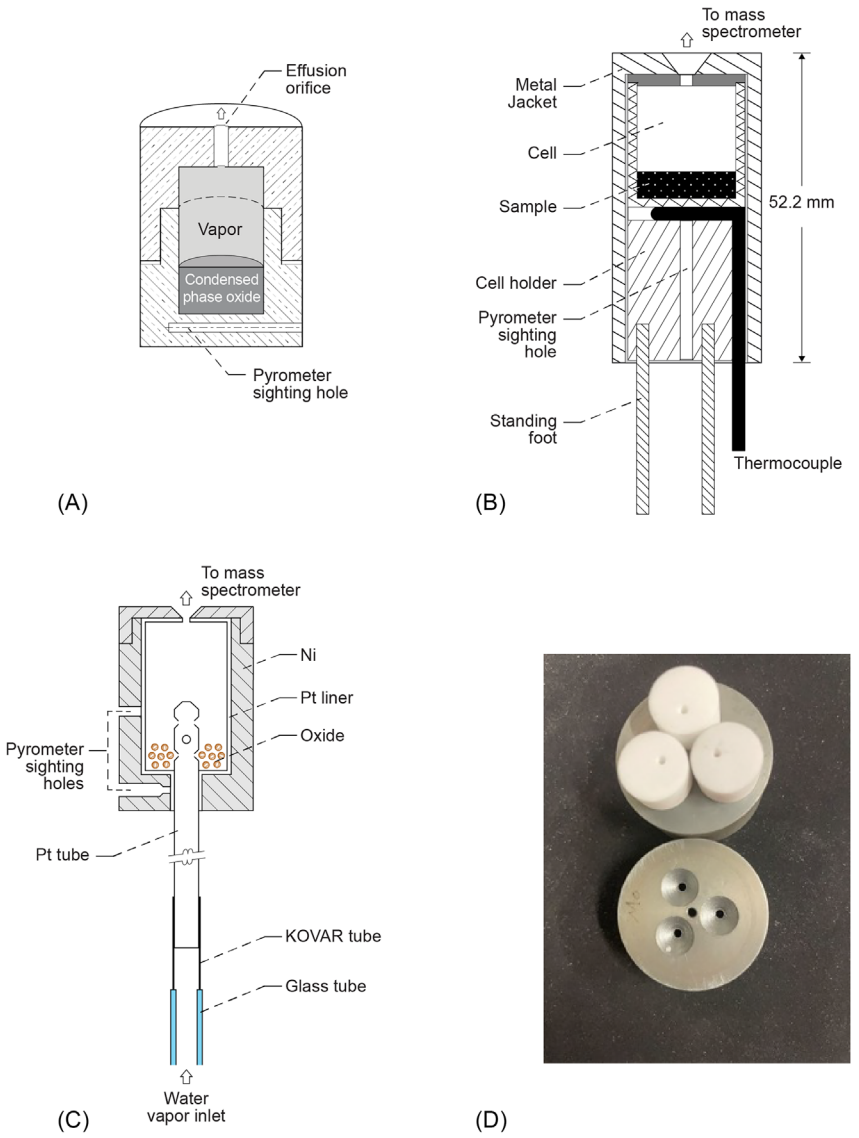

FIGURE 2 Types of Knudsen cells. (A) Basic Knudsen cell. (B) Knudsen cell with isothermal metal jacket. (C) Gas-leak Knudsen cell where the external gases admitted to the cell may be from either a secondary cell or an external connection to a permanent gas. *Source* Adapted from Meschi et al.[17] with permission from AIP Publishing. (D) Multiple cell with two or more cells in an isothermal block. (E) Electrochemical cell where an external chemical potential (e.g., O_2, S_2) is imposed on the sample under study. *Source*: Reprinted from Hilpert[7] with permission from John Wiley and Sons. (F) Tandem cell with a cracker. *Source*: Reprinted with permission from Violet et al.[21] with permission from John Wiley and Sons. [Color figure can be viewed at wileyonlinelibrary.com]

Resistance heating requires large power feedthroughs to handle the high currents needed to obtain the high temperatures; electron bombardment requires less current as only the cell is heated, but arcing from the high voltage may be a problem. Newer designs utilize laser heating of the Knudsen cell.[22] Figure 3B and 3D show that the furnace is surrounded by a tight heat shield pack (Ta, Mo, or W). Contamination of the effusing molecular beam from the trapped vapor in the heat shield cavity is an important issue, and corrections must be applied.[23] The restricted collimation scheme, which will be described, helps minimize this effect.

The importance of accurate temperature measurements to the KEMS method cannot be emphasized enough. Because vapor pressure is an exponential function of temperature, small errors in temperature can lead to large errors in vapor pressure and resultant thermodynamic parameters. Cater[24] describes the significant errors that can result from small temperature variations. Thermocouple and pyrometer measurements are the two most common temperature measurement methods used with KEMS. Both methods offer a high degree of accuracy when used properly and have advanced in recent years.

A thermocouple must be firmly attached to a Knudsen cell with clear contact with the cell's surface. This can be accomplished using a metal strap either placed to the side of the cell or clamped in a well at the bottom of the cell. It is easily connected to a data collection system, which automatically adds corrections for the "cold" junction.

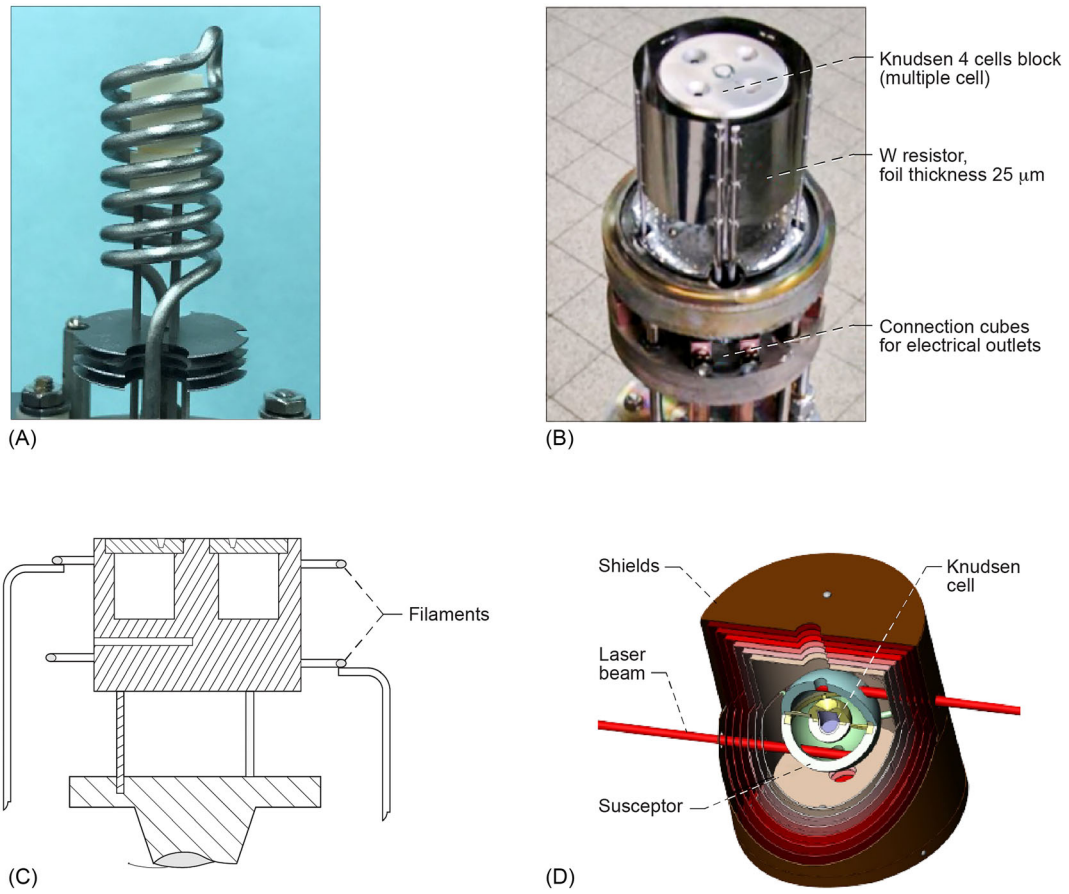

FIGURE 3 Knudsen cell heating configurations: (A) resistance heating with helix element, (B) resistance heating with sheet element, (C) electron bombardment heating, and (D) laser heating at JRC Karlsruhe. [Color figure can be viewed at wileyonlinelibrary.com]

The drawbacks of a thermocouple are that it draws heat away from the cell, so its location adjacent to the sample and in the homogeneous temperature portion of the sample is critical. Further, thermocouples can easily be degraded by the vacuum and/or vapor environment after repetitive experiments.

Pyrometry is a noncontact temperature measurement. Sighting is generally on a dead-end black body hole drilled into the body (side or bottom) of the Knudsen cell, as shown in Figure 2A. This should have a length-to-diameter ratio ≥10. It may be necessary to put a shield around the hole to prevent reflected light from the heating element from interfering with the measurement. Note that due to the imperfections of optics and the presence of windows (vacuum interface), a phenomenon known as the size-of-source effect may appear.[25] This phenomenon has the effect that light slightly outside of the measurement field may partially be measured. To avoid this, it is preferable to have a measurement spot clearly smaller than the image of the black body hole. At NASA Glenn, we have used a tube around the hole to limit the effect of spurious light. This is particularly true in the case of Knudsen cell temperature measurement where the surface of the cell may appear brighter (reflection from heating element) than the black body hole.

Ideally, one could see into the Knudsen cell orifice, which is itself a black body. However, in practice, the vapor emerging from the cell will interfere with the measurement and quickly deposit on the pyrometer window. Also, when temperature is measured on a liquid surface through the effusion orifice, the pyrometer records the brightness of the observed orifice. This results from the addition of two emissivities—that of the liquid in the effusion cell and that of the reflected image of the effusion orifice. If the surface of the liquid is concave, a darker image of the orifice is observed insider a brighter corona; this is the true temperature of the black body. However, if the surface of the liquid is convex, the darker image is larger than the effusion orifice, and the temperature measured will necessarily be lower. Errors of 30 K were noted in calibration runs at CEA-Saclay (S. Chatain and E. Lizon, private communication). Ackerman et al.,[26] Bhatt et al.,[27] and Balakrishnan et al.[28] used the appearance of the dark spot to determine the liquidus temperature in metal/metal–carbide systems. Thus, it is best not to use the effusion orifice as a black body hole for temperature measurements.

Older pyrometers measured radiance/brightness using a "disappearing filament" where the operator would match the color of a filament in the pyrometer to that of the black body hole. Modern pyrometers measure the bright spot with a photon counting device. With a rigid mount, such an automatic device is suitable for repeated measurements and computer data acquisition. A critical issue with pyrometry is keeping the optical path clear and window clean.

Corrections for the window may be made using a separate calibration stand or an in situ calibration. It has been found that single-wavelength pyrometers work best for the small hole machined in a Knudsen cell; multiwavelength pyrometers require a larger sample emitting more energy. However, this requirement may be changing given the rapid development of commercial pyrometers and increasing cell size and sighting hole in improved mass spectrometers.

With both methods, frequent calibrations are a must. Generally, Ag, Au, or Pt melting point is used in appropriate cell materials where no eutectic forms. The first two are ITS-90 standards,[29] but container materials and compatibility are often not discussed. A typical melting point calibration for Au is shown in Figure 4, with a ramp rate of 1 K/min. These data were obtained from an automatic brightness pyrometer and during repeated scanning of the Au peak with signal averaging. The region with constant intensity versus temperature is the three-phase solid–liquid–gas invariant. The melting temperature can be derived from a mean value, when using heating and freezing ramps to evaluate the temperature lag between the thermocouple (or pyrometric cavity) and the sample. This time lag is rate dependent. With a slow ramp rate, the calibration point is generally taken as the onset of melting. It is best to use a consistent ramp rate for every calibration. It should be noted that there are no ITS melting point standards above that of Au, and various high-temperature eutectics have been proposed. The use of high-temperature eutectics as fixed points for calibration to high temperature is a growing area in metrology[30] with applications to KEMS.

Other methods of temperature calibration include the complete vaporization method, in which a small amount of a known vapor pressure standard (Au, Ag, and CaF_2) is vaporized and the net vapor flux is compared to a known value for different temperatures.[5]

2.1.3 | Attaining equilibrium in a Knudsen cell

It is critical that chemical equilibrium be attained in the cell for reliable thermodynamic measurements.[3,31–33] The immediate issue is the presence of the orifice, which means that the system is not truly a closed system because molecules rebounding from cell lid collisions do not equal the vapor flux from the sample. Whitman[32] and Motzfeld[33] have developed an expression to extrapolate to zero orifice size, based on balancing the upward and downward fluxes in a Knudsen cell; a good derivation is provided in the chapter by Paule and Margrave.[34] Extrapolation to zero orifice size is generally used in torsion effusion[35] and weight loss measurements[34] but has more recently been applied to KEMS.[36] The central equation is

$$P_m\left[1+f\left(\frac{1}{\alpha_c}+\frac{1}{W_A}-2\right)\right]=\frac{\alpha_L}{\alpha_c}P_{eq}\quad f=\frac{W_B B}{A} \tag{2}$$

In this equation, the subscripts A and B indicate the cell body and orifice cross sections, respectively, P_m is the measured vapor pressure, W_A is the transmission factor (Clausing coefficient between 0 and 1) for the cell body, W_B is the transmission factor (Clausing coefficient between 0 and 1) for the orifice, P_{eq} is the equilibrium pressure, α_c is the condensation coefficient (fraction of molecules that stick to the sample surface on striking), and α_L is the vaporization coefficient (fraction of molecules leaving the vaporizing surface toward the vapor compared to equilibrium flow). Transmission or Clausing factors represent the fraction of molecules that go through a given geometric opening; they may be calculated analytically[13,37,38] or using a Monte Carlo method.[39] This will be discussed in detail later. Generally, the condensation coefficient is taken as equal to the vaporization coefficient; this is correct only for molecules that obey "micro-reversibility" (evaporation and condensation paths are the same) but can be taken as a reasonable assumption. Now apply Equation (2) to a cylindrical cell with the orifice on top and an evaporation coefficient of unity (no kinetic barrier to vaporization) and dimensions such that $f = 1/100$. Equation (2) then indicates that the measured equilibrium pressure is 0.99 of the equilibrium pressure, an error less than other uncertainties in KEMS.

A plot of P_m versus $P_m\left[f\left(\frac{1}{\alpha_c}+\frac{1}{W_A}-2\right)\right]$ should yield a line with intercept of P_{eq}. Furthermore, the vaporization coefficient, which

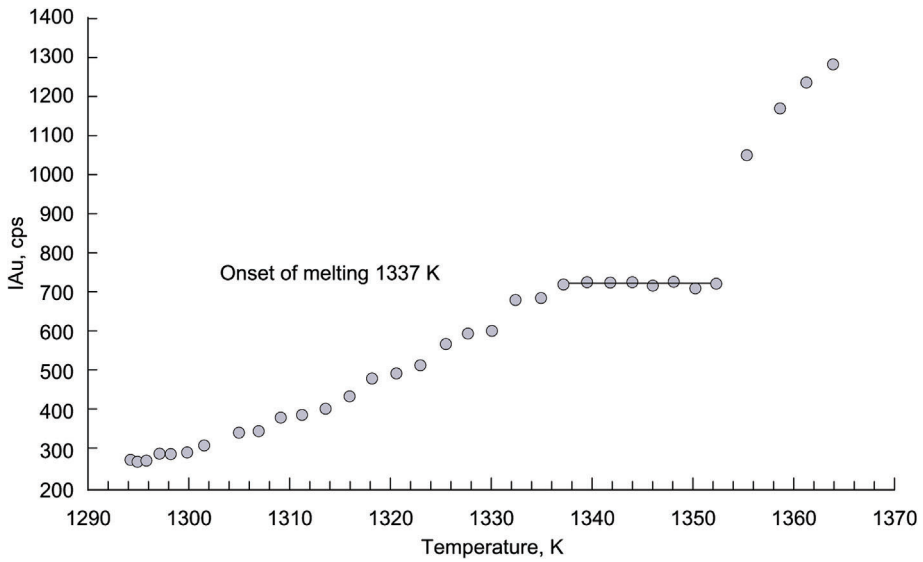

FIGURE 4 Melting of gold temperature and pressure calibration. Ramp rate of 1 K/min (Copland and Jacobson[18]). [Color figure can be viewed at wileyonlinelibrary.com]

gives a measure of the kinetic barrier to equilibrium, can be extracted from the slope of such a line. Note that the use of this equation to determine the evaporation coefficient requires that the same retarded mechanism occur in the range of chosen orifice sizes and is related to the saturation degree of the surface with vapor, as stated by Rosenblatt.[40] Thus, vaporization coefficients measured this way depend on the selected orifice sizes and degree of saturation of the vapor.[40,41] In general, metals have vaporization coefficients close to unity. Compounds, such as oxides, carbides, and nitrides, may have vaporization coefficients much less than unity.[42] A Knudsen cell study of the reactions of SiC and SiO_2 indicated measured vapor pressures had a strong dependence on orifice size and hence a small vaporization coefficient and high kinetic barrier to equilibration.[43] Note also that Equation (2) can be used to design a cell geometry that is best for studying a system with a low vaporization coefficient. In summary, Equation (2) makes corrections to the measured vapor pressure and provides information on the vaporization coefficient.[44] More details on vaporization coefficients can be found in Stolyarova and Semenov[5] and Rosenblatt.[40,45]

Hildenbrand[31] has discussed the problem of equilibria in Knudsen cells in some detail. He further references the study of Golden et al.,[46] which discusses the importance of collision number, that is, the number of collisions a molecule undergoes in the cell. To obtain sufficient internal energy for a unimolecular reaction, about 50 collisions are needed. Golden et al. estimates that 10 000 or more collisions are needed for full thermodynamic equilibrium, with these numbers from the ratio of the orifice area to sample surface area. A Monte Carlo simulation of Knudsen or molecular flow can provide better values for collision numbers.[47] Hildenbrand discusses the special case of a gas-leak cell, where the secondary vapor is leaked into a reaction cell. The secondary vapor can be from either a vessel outside the vacuum system or a second Knudsen cell at a different temperature (see Figure 2C,F).[17] Hildenbrand proposes two tests to check for equilibrium in such a system: either the reactant flow or pressure is changed while maintaining the reaction cell at the same temperature, or equilibrium is approached from the reverse direction. In either case, the change should not alter the measured equilibrium constant. In their studies with a gas-leak Knudsen cell, Gorokhov et al.[48] have used the method based on changing H vapor pressure to study the reactions:

$$CrOH(g) + O(g) = CrO_2(g) + H(g) \quad (3a)$$

$$CrOH(g) + Cr(g) + O(g) = 2CrO(g) + H(g) \quad (3b)$$

Varying P(H) resulted in very little change in equilibrium constant for these reactions, verifying that equilibrium was reached.

In summary, the best test for equilibrium in the cell is to measure an equilibrium constant and check that it is truly constant with changes in reactant flow or pressure. Note that for some compounds with very low vaporization coefficients, like silica, it may be very hard to attain equilibrium in the cell. This will be discussed in more detail later in this paper.

Related to a check for equilibrium is the necessity to completely characterize the system. Important tools are X-ray diffraction (XRD) and electron optical/microanalysis methods. Careful characterization of the solid reactants before and after a KEMS vaporization study is critical. It should be noted that the reactants cannot be truly quenched in a KEMS experiment, and it might be best to supplement KEMS studies with hot-stage XRD.

2.1.4 | Positioning of the Knudsen cell

The Knudsen cell and furnace are typically mounted on a vacuum flange. The cell must be rigidly mounted on the furnace yet be able to be translated so that the emerging molecular beam can be directed into the mass spectrometer to maintain a constant ionization volume. This is important in a single-cell instrument (Figure 5A) but essential in a multiple-cell instrument (Figure 5B,C). Chatillon et al.[50] have developed a system that holds five cells in an isothermal block. This isothermal block is held by an elastic rod, and each cell is pulled into the sampling region by jacks controlled from outside the vacuum. This system has been more recently refined by Heyrman et al.,[49,51] as shown in Figure 5C. The flange is fitted with a large bellow assembly and positioned by x and y jacks, located outside the vacuum system, which tilt the cell into position. This system has a reported positioning accuracy of better than 0.05 mm. The system at JRC Karlsruhe uses a similar system to that of Chatillon et al. but with a smaller bellow and mounting on a vertical door. Johnston and Burley[52] have used a rotatable block holding four cells. Other investigators have used an x–y table, either inside or outside of the vacuum chamber.[53] Figure 5B shows this configuration as used on the NASA Glenn KEMS.[18]

2.1.5 | Molecular beam

The essence of the KEMS method is the well-defined molecular beam that emerges from the Knudsen cell orifice. The diameter of the orifice must be such that Knudsen or molecular flow through the orifice is assured. This is typically taken as the mean free path of the gas escaping from the cell ≥10 times the orifice diameter. Generally, the smallest orifice has a diameter of 0.1 mm, so the maximum useable pressure for this technique is $\sim 1 \times 10^{-4}$ bar. Some investigators have extended the method beyond the molecular flow region into the continuum region and developed correction formulae.[54] The lower limit for the KEMS method typically depends on the sensitivity of the instrument. Some highly sensitive instruments can measure into the 10^{-12} bar region. This very large dynamic range is one of the many advantages of KEMS.

We have thus far implicitly assumed molecular flow through the Knudsen cell orifice. This means the vapor species strikes the orifice wall and is reemitted in a completely random direction. Molecular flow can be modeled analytically[55,56] or simulated using a Monte Carlo technique.[39,57–61] Today, Monte Carlo is probably the most useful technique. A valid simulation can be run on a desktop

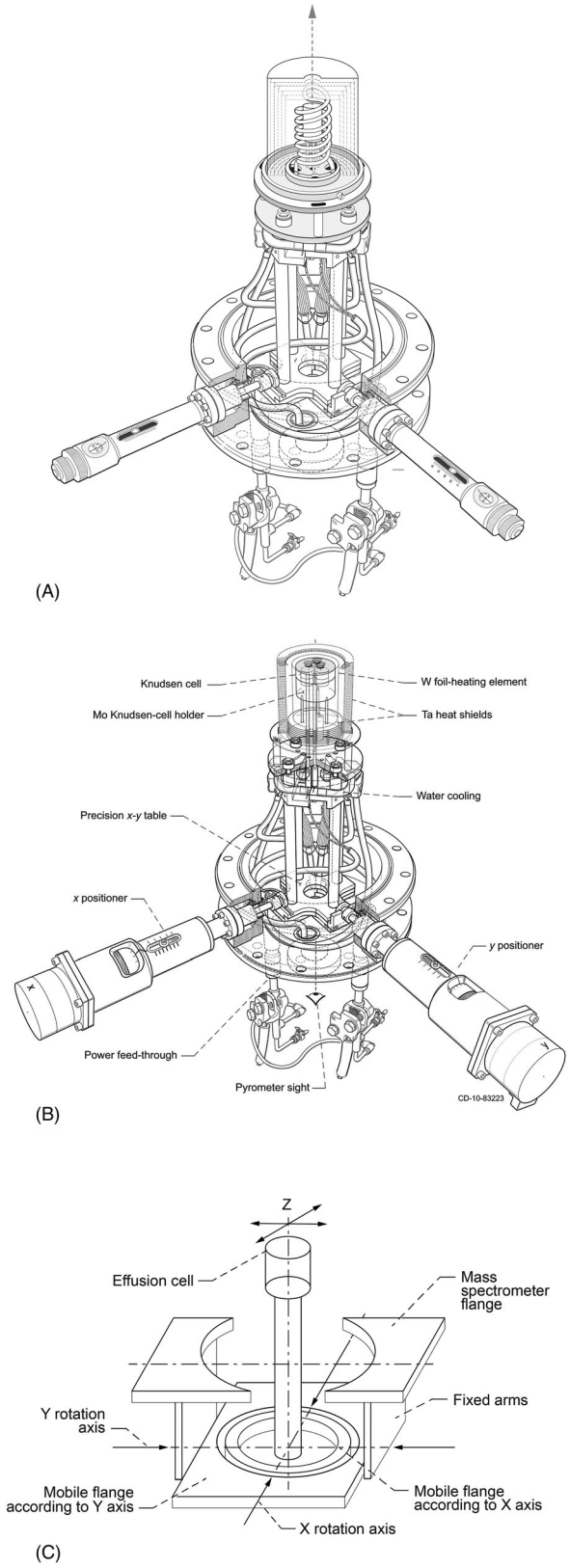

FIGURE 5 (A) Typical single-cell flange with resistance heating furnace; (B) multi-cell furnace/Knudsen cell positioner at NASA Glenn. The computer-controlled x and y stepper motors position the cell and furnace assembly. Note the foil heating element that can be W or Ta. (C) Multi-cell positioner at SiMaP. *Source*: Reprinted from Heyrman et al.[49] with permission from John Wiley and Sons.

computer, and a number of factors can be easily explored. Both methods allow calculation of the transmission or Clausing factor through the orifice. This factor is defined as the number of molecules that escape from the orifice divided by the total number of molecules that enter the orifice. More details on Clausing factors can be found in Margrave.[62] Tabulations and equations for Clausing factors for cylinders with different length-to-radius ratios are given in Santeler.[13]

Of particular interest in KEMS is the distribution of the effusate or molecules emerging from the orifice. This is shown in Figure 6, calculated by sorting the number of molecules emerging at a specific angle relative to the surface of the cell. The solid black-lined sphere is for a very thin-channel or a knife-edged orifice. This is the classical cosine distribution, which means the fraction of molecules is proportional to the cosine of the angle that a molecule's trajectory makes with the surface. Thus, the largest fraction of molecules emerges from the orifice at 0° from the normal. Note that as the channel becomes more elongated (length-to-radius ratio increases), the distribution becomes an ovoid. Thus, the effusate is more directed. The elongation may not increase the axial flux, but it would (1) limit contamination of the furnace/heat shield assembly and (2) decrease the escaping flux from the cell and force equilibrium in the cell.

The Monte Carlo simulations allow counting collisions with the wall and design Knudsen cell orifices accordingly. Some investigators prefer a thin channel or knife edge that gives a near-unity transmission factor and a few molecule wall collisions. Other investigators prefer a channel that gives a lower transmission factor and several wall collisions for each emerging molecule, but a more directed beam toward the ionizing chamber. Monte Carlo simulations additionally allow the investigator to trace the history of each vaporizing species. It can be shown, as discussed by Cater,[3] that for a cell with the orifice on top and a near-unity transmission coefficient for that orifice, most of the molecules that escape are vaporized from the sample surface and travel directly out of the orifice. This is particularly true for low pressures ($<10^{-7}$ bar) and is a desirable situation for directly probing a vaporization process.

This discussion assumes no interaction with the cell surface and no movement along the cell surface (surface diffusion of adsorbed molecules or atoms). In application, there are likely deviations from this behavior because the interior surface of the cell is likely covered by adsorbed molecules that play a role in the condensed phase/vapor equilibria. As noted in Section 2.1.1, no two materials are truly "inert" to each other. Cater[3] has discussed the effects of surface diffusion on Knudsen effusion in some detail. We shall briefly summarize his important conclusions here. In some cases, the molecule may strike the wall and move along this wall before desorbing near the orifice edge. This surface diffusion would necessarily change the net flux, add a contribution to material loss, and also alter the vapor composition emerging from the cell orifice. It is difficult to correct for surface diffusion, as the needed parameters of diffusion path lengths and surface diffusion coefficient are very system specific and not generally available. Monte Carlo simulations offer some insight into

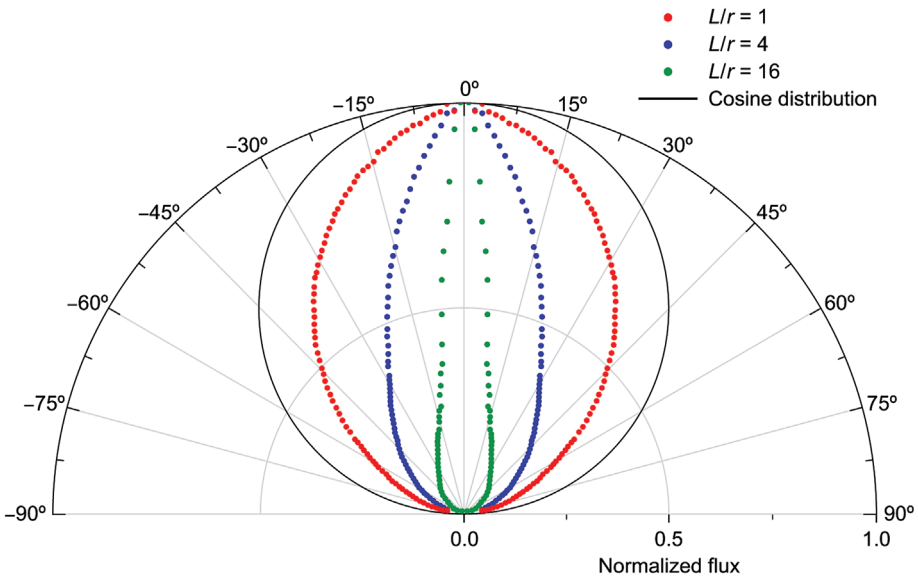

FIGURE 6 Monte Carlo–generated distributions of molecules emerging from orifices of different geometry. Note that *L* is the length of the cylindrical orifice and *r* is the radius. [Color figure can be viewed at wileyonlinelibrary.com]

this phenomena, and Ward et al.[59] have derived a general expression to correct transmission factors for surface diffusion. However, it is best to avoid such material combinations that lead to surface diffusion if possible. According to Ward et al.[59] surface diffusion can be minimized using larger cylindrical orifices instead of thin-edged orifices.

An extreme case of surface diffusion is the phenomenon of liquid creeping up the edges of a cell. This is particularly troublesome with glasses and some salts, and the volume of material that escapes renders a KEMS experiment impossible. Cater[3] recommends the use of cells with sharp-edged orifices or an inner crucible with a sharp edge that cuts the creeping film, the use of single-crystal cell materials, and the avoidance systems where the sample wets the cell material. This is a big problem in studying glasses; the selection of cell material becomes very important.

Coupling of the Knudsen cell to the mass spectrometer is a critical aspect in a KEMS instrument. This coupling has a major effect on the sensitivity of the instrument, the degree of background interference, and the general stability. Recent instruments show considerable advances in this area. Figure 1 shows that a copper plate separates the Knudsen cell vacuum chamber and the ionizer. The copper plate is typically cooled by water or even liquid nitrogen. The basic function of the plate is to shield the ionizer from the high temperatures of the Knudsen cell furnace. Nearly all instruments contain a moveable shutter to help distinguish the beam emerging from the Knudsen cell from the background.[1] This is simply a moveable plate to interrupt the beam emerging from the cell. It may be a part of the copper plate or a separate smaller moveable plate. The shape and location of the shutter is important, particularly in the case of permanent gases (e.g., N_2, O_2, and CO) that exist in the vacuum, as analyzed by Froment et al.[63] It should not act as a valve between the Knudsen cell vacuum chamber and the ionizer chamber, which would interfere with pumping patterns and would lead to erroneous measurements for permanent gases. A small free-standing plate is best, to interrupt only the useful molecular beam.

The copper plate is also used to collimate the full molecular beam emerging from the cell and limit effusing gases from reaching and contaminating ionizer walls. Chatillon et al.[19,64,65] have developed the "restricted collimation method" to direct the effusing vapor into the ionization region. Other groups have applied this method as well.[18,66,67] An aperture in the copper plate with a diameter smaller than the diameter of the Knudsen cell orifice coupled to a second ionization chamber aperture effectively allows the ionizer to only "see" inside the Knudsen cell, allowing only the vapors from the inner-cell gas phase to reach the ionization region. This is shown in Figure 7. According to the nomenclature of Chatillon, the aperture in the copper plate is the "field aperture," and the aperture adjacent to the ionizing region is the "source aperture." The geometry of the NASA Glenn system is shown in Figure 8A, and modeling parameters (aperture spacing and orifice diameters) are shown in Figure 8B.[61] Chatillon et al. have derived equations for the flux through these different apertures based on the analogy of light transmission between two disks, which decreases inversely with the square of the distance between the two disks.[68,69] The fraction of molecules that leave a radiating disc and arrive at a receiving disk is given by

$$F(r_1,r_2,a) = \frac{\left(r_1^2+r_2^2+a^2\right) - \sqrt{\left(r_1^2+r_2^2+a^2\right) - 4r_1^2r_2^2}}{2r_1^2} \quad (4)$$

Here a is the distance between the two disks, r_1 is the radius of the radiating disk, and r_2 is the radius of the receiving disk. This fraction is the unit of solid angle that reaches the second aperture. The flux reaching the second aperture is given as

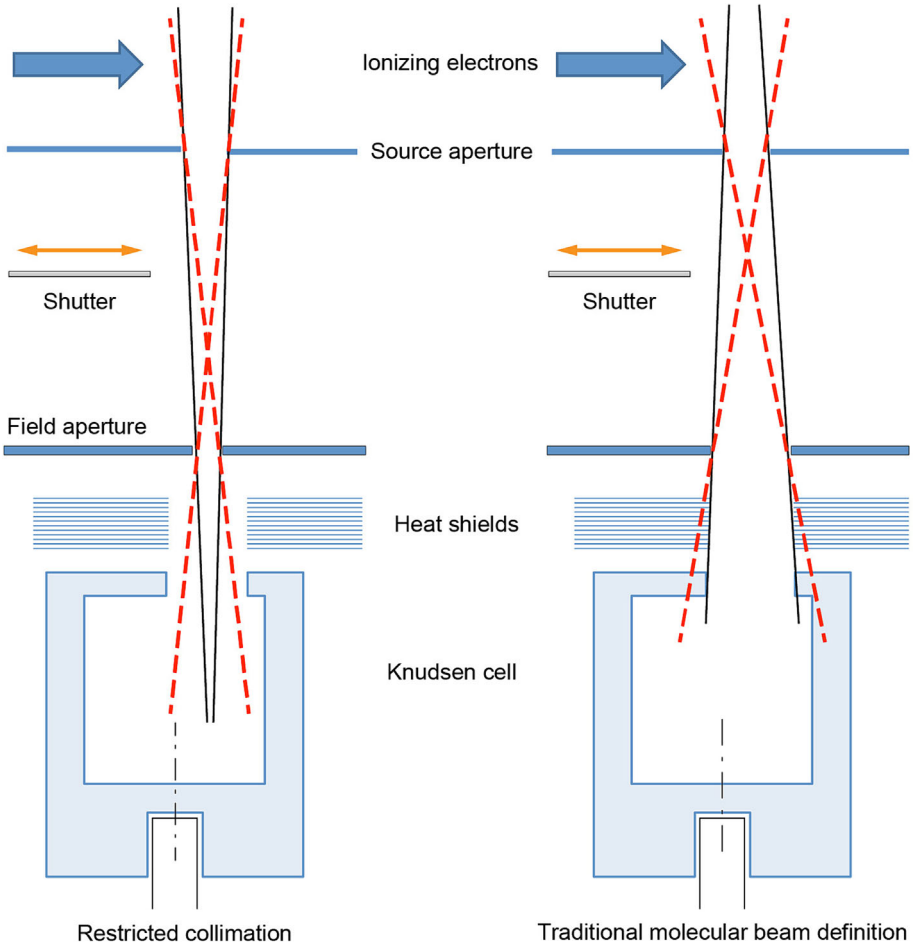

FIGURE 7 "Ray diagram" illustrating the advantages of restricted collimation. [Color figure can be viewed at wileyonlinelibrary.com]

$$J_A = \left(\frac{p_A}{\sqrt{2\pi M_A RT}}\right) F(r_1, r_2, a) \tag{5}$$

Factor F is the proportion of molecules exchanged between the surfaces of the two apertures. The cross section of the orifice, which is larger than the source (Figure 7), is replaced by the surface of the field aperture. The $F(r_1,r_2,a)$ term contains the emitted surface (field aperture) emitting into the vacuum. Nuta and Chatillon[65,70] have performed calculations using different distances between the sample and field apertures and showed the flow, J_A, from the surface of the sample (the surface that is viewed by the detector in the restricted molecular beam device) is constant, even when tilting the sample. This means the resulting flow arriving at the ionizer remains the same. Thus, the restricted collimation device is (1) really the sampling of the useful molecular beam in place of the effusion orifice and (2) independent of the cell (tilting, distance, orifice, etc.) and sample.

Chatillon and Nuta[65,71] use their derived equations to optimize the distances between apertures and diameters of apertures. This problem can also be handled utilizing the Monte Carlo simulations discussed earlier.[61] A direct comparison of the Monte Carlo simulation of flux transmission to the analytical simulation results of Chatillon et al.[65,70] gives qualitatively similar results from both approaches, as shown in Figure 8C.

Another relatively recent advancement at the Knudsen cell–ionizer interface is the introduction of a valve between the Knudsen cell furnace chamber and the ionizer chamber.[7,72] The inclusion of this valve is technically challenging, as it must be able to withstand very high temperatures and also be a "low profile," in that it does not add unnecessary distance between the Knudsen cell and the ionizer. However, such a valve has many advantages. It allows the ionizer and detector to remain powered at all times. This results in improved filament and detector longevity and, most importantly, constant sensitivity and calibration constants for successive experiments. Additionally, it allows rapid changing of specimens.

2.2 | Ionizer

2.2.1 | Ionizer/ion extraction and acceleration

The next major section of a KEMS instrument is the ionizer. Novel ionization methods allow removal of electrons from a large molecule without fragmentation. However, many of these novel methods are not applicable to high-temperature vapors; as such electron impact continues to be the predominant method of ionization in most instruments, because ionization yields (~1 in 10^4) are quite constant

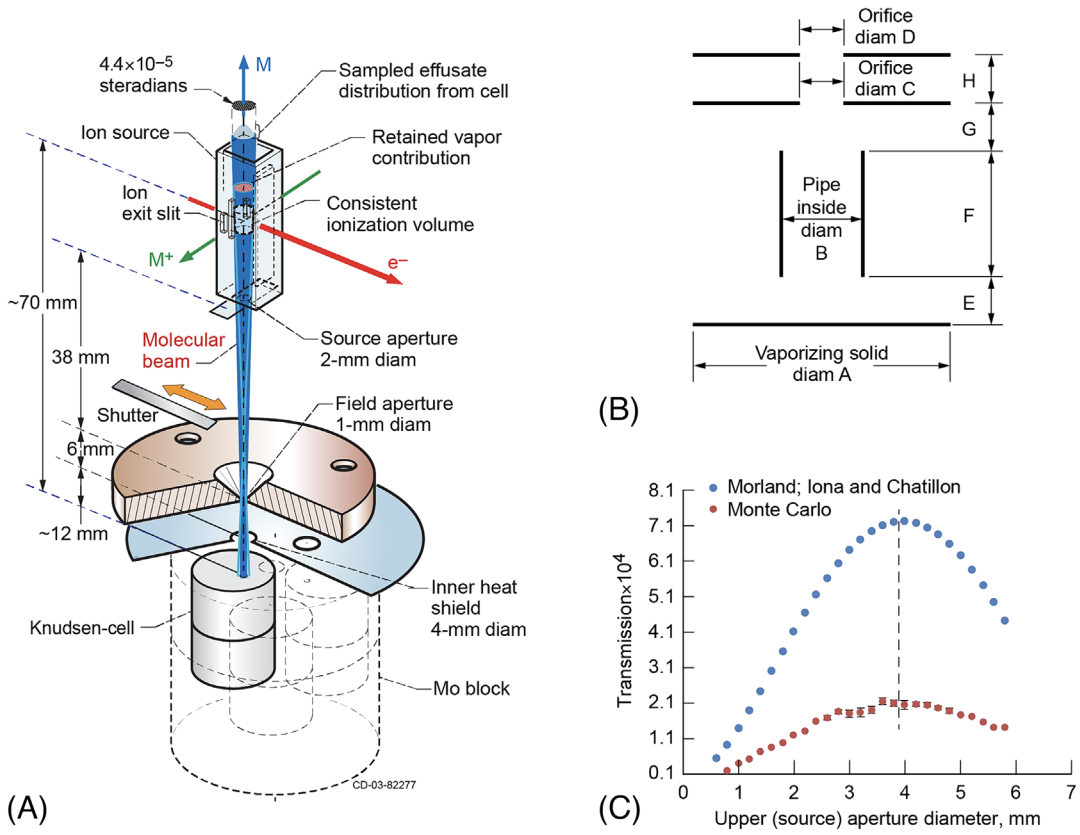

FIGURE 8 (A) Knudsen cell–generated molecular beam introduction to ionizer in NASA Glenn KEMS (Knudsen effusion mass spectrometry) instrument. (B) Geometry for computer model of above. (C) Results of Monte Carlo simulation and analytical formulation for optimizing dimensions. *Source*: Reprinted with permission from Radke et al.,[61] John Wiley and Sons. [Color figure can be viewed at wileyonlinelibrary.com]

for different species (i.e., with cross sections in the same range). Figure 9A,B shows the classic design of the ionizer filament and the high-voltage focusing plates used in the NASA Glenn magnetic sector instrument (modified Nuclide/MAAS/PATCO 12-90-HT). The apex of the filament emits the electrons toward the ionization box under a fixed voltage. These electrons are collimated as a quasi-monoenergetic beam to a well-defined ionization (but unknown) volume (Figure 8A). Note that the entire ionization assembly is at a high voltage, typically 5–10 kV. Typically, the filament is heated with a few volts and several amperes up to 2000–3000 K for emission to start.[73] The relationship between the electron current density, i_e, and temperature, T, and the properties of the filament are given by the Richardson equation[73]:

$$i_e \propto T^2 \exp\left(-\frac{\beta\phi}{T}\right) \quad (6)$$

Here β is a proportionality constant, and Φ is the work function. The high-kinetic-energy electrons collide with the incoming molecular beam to form ions:

$$A + e^- = A^+ + 2e^- \quad (7)$$

The trap collects a small portion (usually ~5%) of the electrons that do not interact with the molecular beam. The filament current is controlled by maintaining either a constant trap current or, more commonly, a constant emission. The energy of ionizing electrons (or electron-accelerating potential) is important and, in a well-designed ionizing chamber, controlled to ±0.1 eV. At low electron energies and constant emission, high filament current is necessary. Typically, ionizer circuits have an adjustable current limit control to protect the filament from burning out.

It should be noted that thermal ionization may be important at very high temperatures. Kudin and colleagues[74,75] have studied thermal ionization of a number of metal halides by turning off the electron impact ionizer and carefully examining the thermal ions produced in the Knudsen cell.

The filament box, including the filament, filament aperture, trap, and repeller (Figure 9A), and the ion entrance aperture and focusing lenses (Figure 9B) are all at different potentials. Klemperer and Barnett[76] present a useful discussion of the fields formed when two plane conductors are placed on either side of an aperture and the penetration of the fields through that aperture. Figure 10A,B show this situation with equipotential lines. Figure 10A is for the ionization box where the two conductors are the filament and the filament box. Because the filament is negative relative to the box, the conductors are at opposite potentials and the equipotential lines show a saddle-point-shaped pattern. This imparts a bent trajectory to the electrons. Further additional energy is added to the electrons. Figure 10B is for

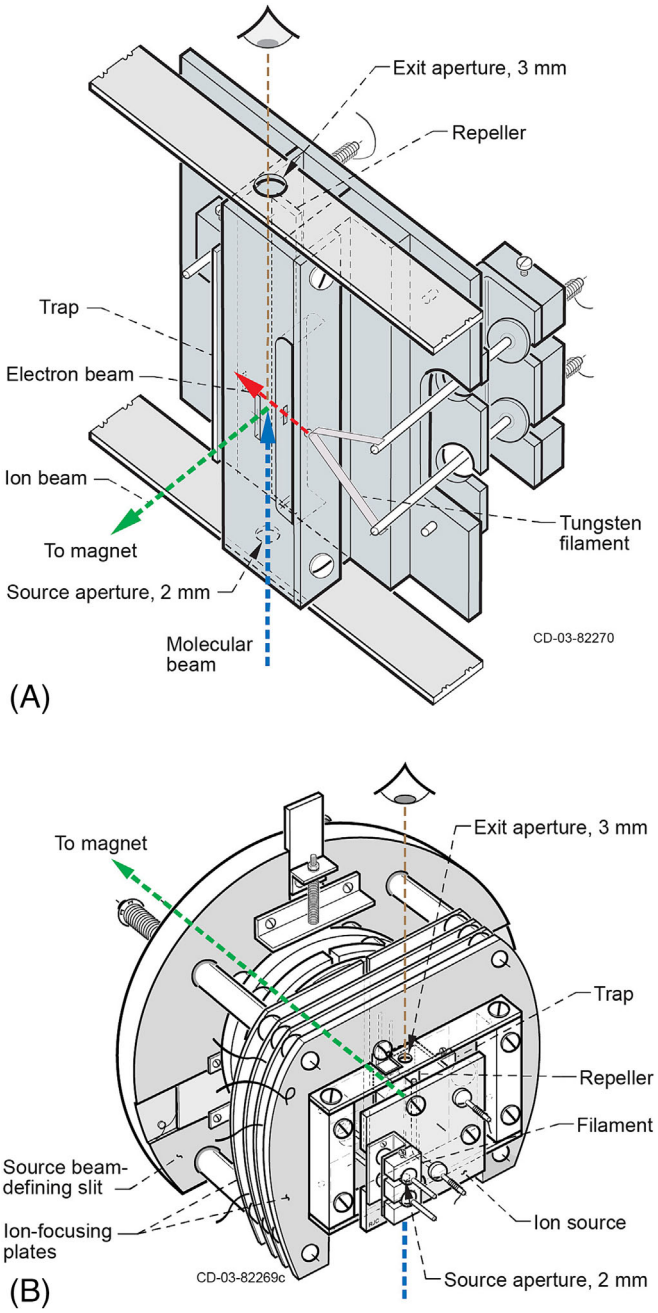

FIGURE 9 Ionizer and ion beam focusing plates for NASA Glenn KEMS instrument: (A) electron impact ionizer and (B) ion beam focusing plates. [Color figure can be viewed at wileyonlinelibrary.com]

the formed ions, and two conductors are now the repeller plate and the extraction plate. These fields are both in the same direction, and the equipotential lines are now all in the same direction. This directs the positive ions through the ion entrance aperture. The important points are as follows: (1) the unavoidable nonuniform fields in the filament box necessarily change the energy of the ionizing electrons and must be corrected for, and (2) those fields set the formed ions on different trajectories and lead to crossover in the ion beam. To correct for the changes in the energy of ionizing electrons, background species (N_2 or CO, H_2O, Ar) can be used to calibrate the electron energy scale.[77]

Figure 10C is a plot of positive ion intensity versus repeller potential. Note the repeller is typically 10 000 ± 10 V. Ideally at 0 V (10 000 V) the ion intensity reaches a sharp maximum. The maximum is also obtained with a positive "push" of the ions into the extractor. The repeller together with the extractor is termed the "immersion lens." Improvements to the ionizer and immersion lens can lead to improved ionization efficiency and sensitivity.[78] Some investigators have added magnets to their ionizers, which increases sensitivity but may introduce some mass dependence on sensitivity.

Current modeling tools allow design of the ionizer with regard to the physical arrangement of the focusing plates and their potentials.[78,79] The design and optimization of ionizers have been revolutionized by computer simulation software, most notably SIMION.[79] This software has been in use for over 30 years and allows the physical and electrical characteristics of an ionizer to be optimized with respect to sensitivity, ion yield, and other desired parameters. SIMION models of the ionizer in the NASA Glenn instrument and resultant electron and ion trajectories are shown in Figures 11A–C. Figure 11B shows the electrons in the box set for maximum intersection with the ion beam. Note that the repeller is often at a nonzero potential for maximum signal, and this may impart additional energy to the electrons. The electron energy thus needs to be calibrated with known gases.[80] Figure 11C shows the optimum ion beam through the focusing plates. Note the ideal, thin ion beam and the crossover points.

2.2.2 | Ionization efficiency curves

The ionization of a neutral species by an energetic electron is rarely as simple as that depicted in Equation (7). Often, ionization is accompanied by bond breaking (fragmentation), multiple ionization processes, and kinetic energy gain of the resultant ions or neutrals. These processes can, at least partially, be separated according to their ionization efficiency curve, shown in Figure 12. Ionization efficiency curves are described in detail in the reviews of Drowart and Goldfinger[2] and Grimley.[4] The appearance potential can be extracted from this curve by using one of several methods.[18] The linear extrapolation method has been used for many years and is shown in Figure 12. The linear portion of the curve is simply extrapolated to the *x*-axis. This *x*-axis intercept is the appearance potential, which may be calibrated by comparison to the well-established appearance potentials of known vapors.[81,82] The curvature of the ionization efficiency curve (Figure 12) may be due to several reasons: (1) non-monoenergetic electrons, ~0.1 eV, spread from the temperature distribution along the emitting filament, which increases at low electron energies due to a loss of emission regulation, as discussed earlier; (2) different ionization locations in the immersion lens region;

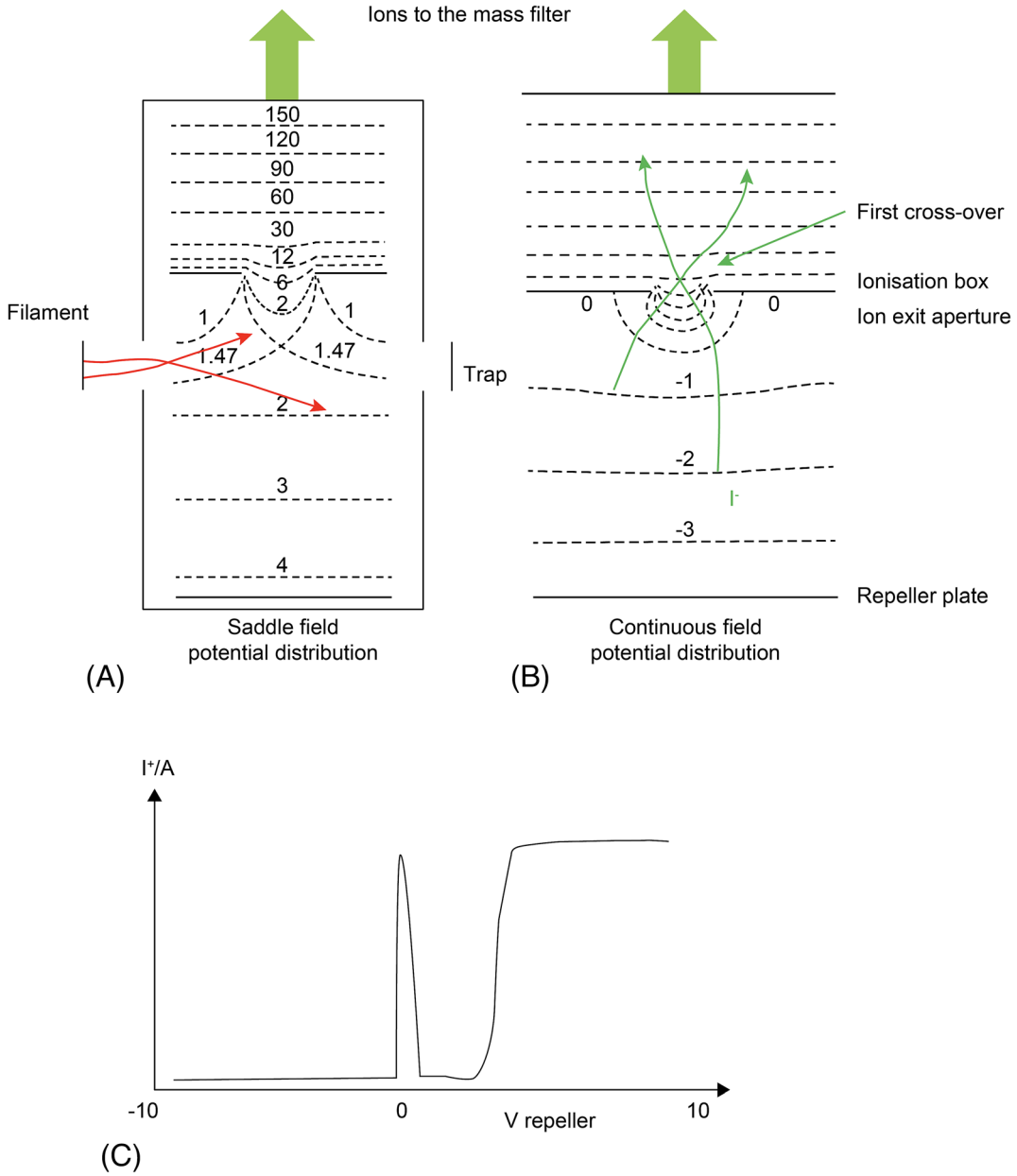

FIGURE 10 Diagram of filament box with lines showing relative magnitude of electric field and trajectories of (A) ionizing electrons and (B) formed ions. *Source*: Adapted from Klemperer and Barnett.[76] (C) A plot of ion current versus repeller voltage. [Color figure can be viewed at wileyonlinelibrary.com]

and (3) molecules/species with closely spaced energy levels. Note that in Figure 12, the measured appearance potential for Al is 6.83 eV, compared to tabulated ionization potentials of 5.77–5.98 eV. Al does not have closely spaced electronic levels, but other issues that form the curvature may explain the difference between the tabulated ionization potential of 5.77–5.98 and the measured appearance potential of 6.83 eV.

Drowart and Goldfinger[2] and Grimley[4] have shown the various ionization efficiency curves that result from fragmentation. These ionization efficiency curves are a valuable tool in understanding the ionization process. In some cases, when formation energies are known and no kinetic energy exchange occurs, Born–Haber cycles can be used to calculate dissociative ionization thresholds.[83]

Often, fragmentation of a simple molecule can be minimized by working at an electron energy between the appearance potential and the summation of the appearance potential and dissociation energy of that molecule. For example, the appearance potential of SO_2^+ is 12.32 eV[82] and the bond energy of the S=O bond is 5.51 eV.[84] Thus

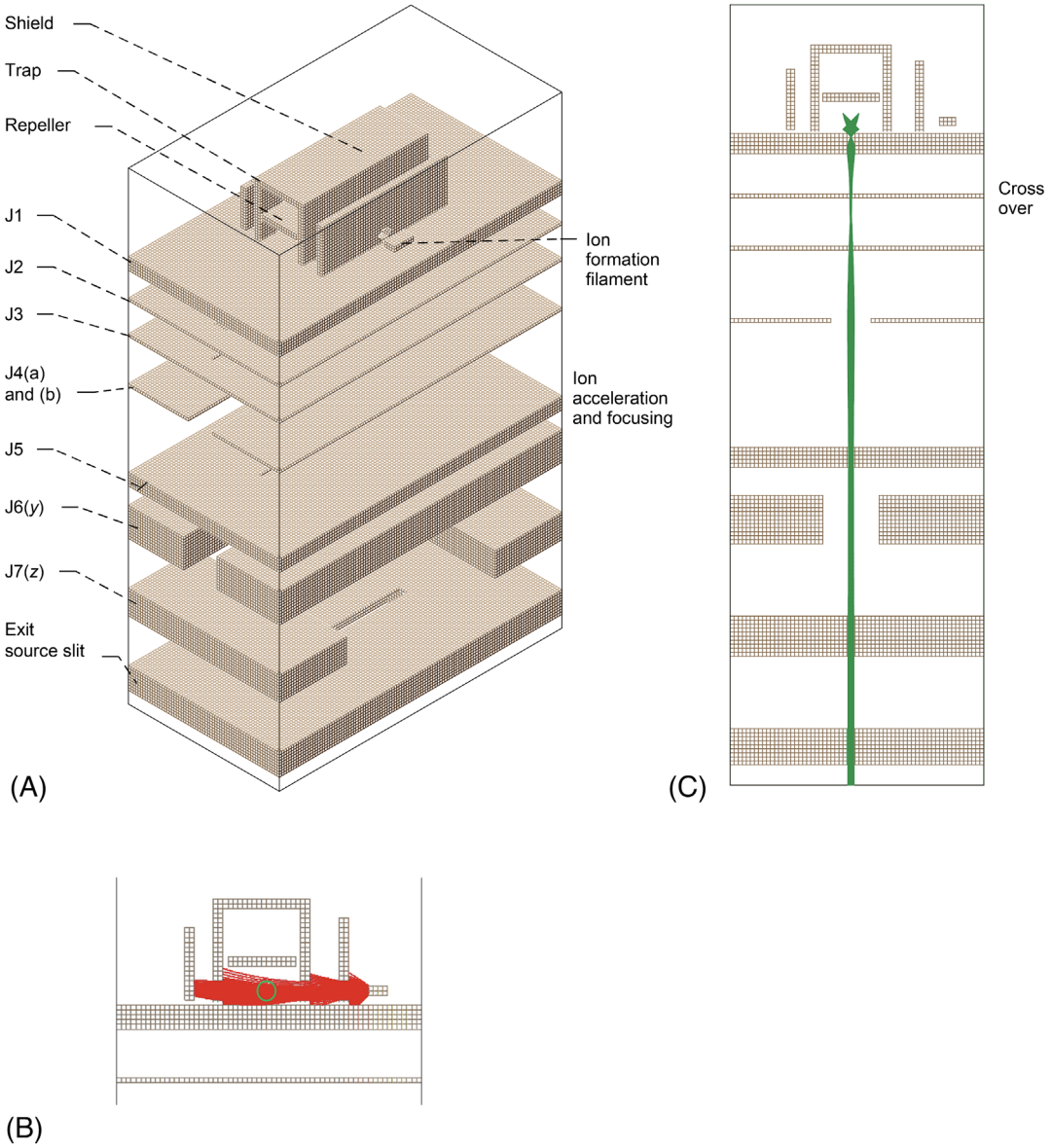

FIGURE 11 SIMION model of ionizer and ion beam focusing plates: (A) three-dimensional view; (B) electron beam intersection with molecular beam (green circle); (C) cross section showing optimized beam shape, with repeller at 10 000 V, J2 9560 V, J3 9390 V, and J4 6500 V (Copland and Jacobson[18]). [Color figure can be viewed at wileyonlinelibrary.com]

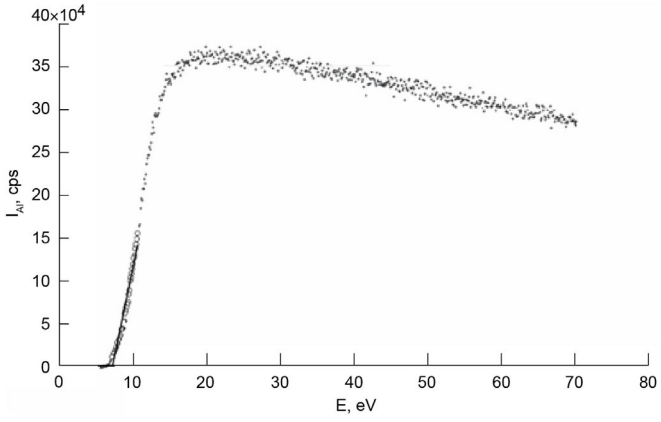

FIGURE 12 Ionization efficiency plot for Al.[19]

it would be best to work with an electron energy of 12.32–17.83 to avoid fragmentation of SO_2.[85,86] A similar method may be used to distinguish O^+ from O(g) and not from O_2(g) dissociation.

Conversely, some investigators choose to use a high electron energy to maximize signal strength. In such cases, fragmentation occurs, and therefore the fragmentation pattern must be known. An example is studies on Am, U, and Pu oxide vapors.[77,80]

In summary, electron impact ionization of molecules is the sum of several different processes:

$$AB + e^- \rightarrow AB^* + e^- \rightarrow AB^+ + 2e^- \qquad \sigma_{AB^+/AB} \qquad \text{IP} — \text{ionization potential} \tag{8a}$$

$$\rightarrow A^+ + B(g) + 2e^- \qquad \sigma_{A^+/AB} \qquad \text{AP} — \text{appearance potential} \tag{8b}$$

$$\rightarrow B^+ + A(g) + 2e^- \qquad \sigma_{B^+/AB} \qquad AP \text{—appearance potential} \quad (8c)$$

Here σ is the ionization cross section, which will be discussed in subsequent sections of this paper and are covered in detailed in Drowart et al.[87]

2.2.3 | Relationship between ion intensity and partial pressure of vapor species

The relationship between partial pressure in the cell and measured ion intensity is central to KEMS. This relationship has been derived in Drowart and Goldfinger,[2] Grimley,[4] and Chatillon et al.,[19,88] and will be briefly summarized[18] here due to its importance. The number of ions in an infinitesimal unit of volume is given by the following expression:

$$N_A^+(E)d\nu = I_e^-(E)l_e\rho_A\sigma_A(E)d\nu = I_e^-(E)l_e\sigma_A(E)\frac{j_A}{\overline{c_A}}d\nu \quad (9)$$

Here $I_e^-(E)$ is the intensity of the ionizing electrons, which is a function of their energy, E; l_e is the electrons' path length; ρ_A is the density of neutral atoms A in the ionization volume $d\nu$; and $\sigma_A(E)$ is the ionization cross section, which is a function of the ionizing electron energy, E. The instantaneous density of the neutral atoms is given by the flux of atoms A from the Knudsen cell orifice, j_A, divided by the average molecular speed, $\overline{c_A}$. This flux reaching the ionizer is scaled by the inverse of distance from the orifice to the ionizer, as discussed previously, and given by the following integral over the surface of the molecular beam entering the ionizer:

$$j_A = \int_S \left(\frac{W_C p_A}{\sqrt{2\pi M_A RT}}\right)\frac{1}{a^2}ds \quad (10)$$

Here a is the distance from the cell orifice to the ionization region. Equation (10) can be substituted into Equation (9) and integrated over the ionization volume to give

$$N_A^+(E) = \int_V\int_S \left(\frac{W_C p_A}{\sqrt{2\pi M_A RT}}\right)\frac{1}{a^2}\sigma_A(E)\sqrt{\frac{\pi M_A}{8RT}}dsd\nu \quad (11)$$

In practice, the volume and surface integrals are absorbed into a constant, and the density of ionized A^+ species is written as

$$N_A^+(E) = \frac{k p_A \sigma_A(E)}{T} \quad (12)$$

The measured ion intensity can be expressed in terms of the ionizer and detector parameters:

$$I_A(E) = N_A^+(E)\varepsilon(x,y,z)\tau_{ion}\gamma_A f_A \quad (13)$$

Here $\varepsilon(x,y,z)$ is the ion-extraction efficiency, τ_{ion} is the transmission probability of the mass analyzer (to be discussed in the next section), γ_A is the detector efficiency (to be discussed in subsequent sections), and f_A is the isotopic abundance. Combining Equations (12) and (13) gives

$$I_A(E) = \frac{k p_A \sigma_A(E)}{T}\varepsilon(x,y,z)\tau_{ion}\gamma_A f_A \quad (14)$$

This can be rearranged to

$$p_A = \frac{k' I_A(E) T}{\gamma_A f_A \sigma_A(E)} \quad (15)$$

The factors $\varepsilon(x,y,z)$ and τ_{ion} are absorbed into k'. In this expression, k' is commonly referred to as the machine constant and is generally determined from a well-known standard material, such as Au or Ag. Equation (15) is the central equation in KEMS, which relates partial pressure in the Knudsen cell to measured ion intensity.

2.2.4 | Ionization cross sections of vapor species

An important quantity in Equation (15) is the $\sigma_A(E)$, the ionization cross section. Since the beginnings of MS, the accuracy of cross sections has been the limiting factor in determining absolute pressure. They are not known with accuracy, and their dependency on parameters such as temperature and ionizing electron energy is not clearly established. Drowart et al.[87] discuss both atomic and molecular cross sections in detail in their 2005 review of KEMS. Here we shall briefly summarize calculations and measurements of atomic and molecular cross sections and current quantum methods of calculation. Atomic cross sections are better known than molecular cross sections. There are several datasets of atomic cross sections in the literature.[89–92] The early calculations of atomic cross sections of Otvos and Stevenson[89] and Mann[90,91]—mainly at their maximum near 70 eV—are based on Bethe's results of cross-sectional proportionality of mean square electron shell radius.[93] They use hydrogen-like wave functions to calculate that radius. Then these calculations were scaled using measured ionization cross sections. Bell et al.[94] have developed an expression to describe the dependence of atomic cross section on ionizing electron energy:

$$\sigma_j(E) = \frac{1}{EE_{i+j}}\left[A_j \ln\left(\frac{E}{E_{ij}}\right) + \sum_{i=1}^{5} B_{jk}\left(1 - \frac{E_{ij}}{E}\right)^k\right] \quad (16)$$

Here, E is the electron energy, E_{ij} is the binding energy for orbital j, and A_j and B_{jk} are constants. Bonnell and Hastie have developed a computer program based on Mann's atomic cross sections to calculate the cross section as a function of ionizing electron energy.[87] This program is currently available on the KEMS web page.[95] An example of the calculated cross section of Au as a function of electron energy is shown in Figure 13. Many measured cross sections are given in the literature,[87,96] which can be compared to the calculations.

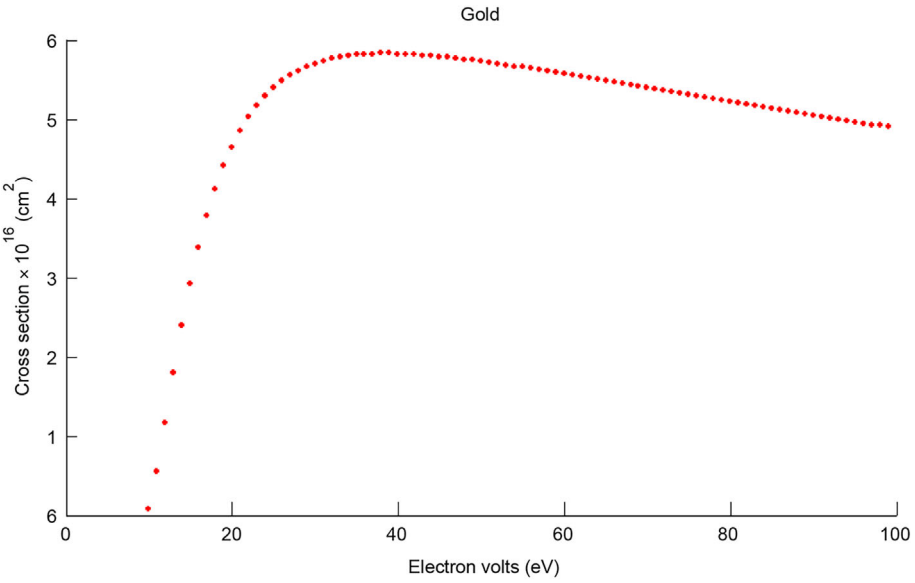

FIGURE 13 Calculated cross section as a function of electron energy. [Color figure can be viewed at wileyonlinelibrary.com]

The ionization cross sections of molecules are much less well understood. Otvos and Stevenson[89] first proposed the "additivity rule" where ionization cross sections are summed, and then some investigators have applied a "correction factor" for a particular molecule. The "correction factor" is based on measurements of dimer to monomer ratios. Most commonly, a factor of 0.75 is used.[5] However other factors have been used.[87] Drowart et al.[87] have discussed the additivity in regard to known molecules and particularly saturated hydrocarbons and found that it is likely correct and may be related to fragmentation patterns. Younés et al.[97] and Gotcu-Freis et al.[77,98] have successfully utilized the additivity rule with a full knowledge of the fragmentation pattern in their studies on UO_2 and Pu–Am–O vapors, respectively.

The eventual solution to these uncertainties in both atomic and molecular cross sections may lie in refining the description of the electron–neutral species collision and the application of modern quantum methods to calculations of total and partial cross sections. Kim and Rudd[99] have developed the binary encounter theory to more accurately describe the interaction between the atom/molecule and an electron. This was further developed by Deutsch and Märk[100–102] in a series of papers. Their approach improves on the "correction" factor in molecular cross sections by using Mulliken orbital population distributions.[103] These concepts continue to evolve and show promise for resolving this "weak link" in many types of MS.

2.3 | Ion filtering/mass analysis

Once a beam of ionized species has been produced and accelerated, the species are sorted based on their mass-to-charge ratio. Three types of ion sorters have been used to analyze high-temperature inorganic vapors: magnetic sector, quadrupole mass filters, and time-of-flight mass filters. Details of these different types of systems can be found in the literature.[73,104] In the past, magnetic sector instruments have been preferred due to their mass-independent transmission and high resolution. Time-of-flight mass spectrometers do not have mass-dependent sensitivity; however, their overall sensitivity is lower than that of magnetic sector instruments. Ionization efficiency curves can be obtained with accuracy on these instruments due to null electric fields. In regard to quadrupole mass spectrometers, recent improvements have led to instruments with much less mass-dependent sensitivity and higher resolution. Many excellent KEMS studies have been reported using quadrupole mass spectrometers.[105–108]

2.4 | Ion detectors and signal measurement

2.4.1 | Ion detectors

Generally, ions are detected by either a Faraday cup or an electron multiplier. Electron multipliers may be in discrete dynode form or continuous dynode form. The output of either may be measured as ion current or ion counts.

First, consider a Faraday cup.[73,109,110] This is simply a cup or cage (typically several millimeters) that collects ions from the ion sorter, generally with a front electrode to prevent the generated electrons on impact from escaping. The ions hitting the metal produce a small current as they neutralize. This current is the ion intensity and is measured as a potential drop across a precision resistor. A simple Faraday cup provides the raw signal with no amplification.

Most instruments use some type of electron multiplier.[73,109] A conventional electron multiplier contains a conversion dynode, which converts the stream of ions to electrons. This is followed by a series of dynodes (usually 16–20) set up for a "cascading" effect where each dynode ejects more electrons than strike it. Typically, the dynodes are arranged as coupled opened cylinders or as coupled slats in a "venetian blind" arrangement. Cu–Be alloys were the most commonly used dynode materials in the past. The gain, γ, from the multiplier can be calculated as

$$\gamma = CD^n \quad (17)$$

Here C is the conversion efficiency of the first dynode, D is the conversion efficiency of subsequent dynodes, and n is the number of dynodes. If C is taken as 1 and D as 2, for a 20-dynode multiplier the resultant gain is on the order of 10^6. The output of the multiplier is measured as a voltage drop across a precision resistor measured using an electrometer. The usual maximum multiplier gain is $\sim 10^6$ and is reached by increasing the applied high voltage until the appearance of a "dark" or background current at the most sensitive setting when no ions impinge on the multiplier. The experimental gain is measured for a high-incident ionic current by comparing the Faraday cup signal with the multiplier signal. Degradation of the multiplier, which is typically due to oxidation of the Cu–Be dynodes, is indicated by a loss in gain, that is, the appearance of the "dark" current at lower applied voltages. Ag–Mg dynodes have replaced Cu–Be dynodes on many multipliers due their superior oxidation resistance.[111]

Continuous dynode multipliers are used in many quadrupole instruments.[104] They are constructed of a semiconducting material that is generally more oxidation resistant than the Cu–Be dynodes of a discrete dynode multiplier. They are also more compact and less expensive than discrete dynode multipliers.

Sensitivity independence of mass in multipliers can be achieved using ion counting. Each ion impact produces an electron pulse that is recorded by a counting chain (preamplifier and counter). The height of the pulses is maximized using a high-voltage limit, which sets a gain of $\sim 10^8$. The counting chain can be set to minimize pulses from the dark current, which are often referred to as "electronic ripple." The "dark" current, which consists of low-amplitude pulses, is eliminated by an amplitude threshold that must be set. Most Ag–Mg multipliers have a dark current of <1 cps. The counted pulses are the number of ions that impact the first dynode of the multiplier. For optimum performance the multiplier should be protected with shields of Cu, Armco iron, and magnetic μ-metal. As mentioned, the multiplier should be in a portion of the spectrometer that is under UHV.

2.4.2 | Ion current and ion counting measurements in the mass spectrum of a vapor

As noted, the multiplier output can be measured as the voltage drop across a precision resistor using an electrometer. The major disadvantage of this method is that the multiplier gain, γ_A, is dependent on mass number, M_A. This is expressed for mass numbers greater than ~10 as[112]

$$\gamma_A = K\sqrt{M_A} \quad (18)$$

Here K is a constant. This dependence on mass number needs to be considered when converting ion intensity to partial pressure (Equation 15).

Many modern KEMS instruments use ion counting[113,114] as described in the previous section. This is primarily due to high sensitivity of the ion counting and lack of mass dependence on counting sensitivity. Ion counters typically operate at high speed ($\geq 10^8$ Hz), and impedances of the ion counting chain–multiplier connections, vacuum flange feedthroughs, preamplifier, and counter have to be matched and suited to high-speed operation. As noted, when plotting gain versus voltage for a multiplier, there is typically a plateau. This is the "counting plateau." At this voltage counts can be measured. Ion counting has a large dynamic range. In theory, very low count numbers (1 cps) can be accurately measured by extending the counting interval to long times. At the other extreme, high count rates must be corrected for dead time. This is related to the amount of time needed for the counter to process an event or pile-up limit. It is defined as

$$R_T = \frac{R_m}{(1 - \tau R_m)} \quad (19)$$

Here R_T and R_m are the true count rate and measured count rate, respectively. τ is the dead time. In practice the dead time is determined from different isotopes of the same material[18,110] and using the known isotopic ratio to determine the dead time correction. Note that the highest count rates should be measured using the Faraday cup.

2.5 | Assignment of ion peaks in the mass spectra of a vapor to parent molecules

The assignment of an ion signal to its parent molecule is a critical issue in every application of MS. KEMS has many tools for assigning an ion signal to a particular parent:

1. The ion signal's mass-to-charge ratio. This is the basic mass spectrometric analysis.
2. The isotope distribution of a collected ion. Commercially available computer codes can calculate the isotopic distribution for a species containing atoms with several stable isotopes. This is particularly useful for species with several abundant isotopes, such as Cl or Mo.
3. The "shutterability" of a particular signal. "Shutterability" indicates how much of a signal is background and how much is from the cell. Permanent gases, such as O_2, CO_2, and N_2, tend to be less "shutterable." Nonetheless, in a well-designed system, a permanent gas whose intensity decreases on closing the shutter emerges from the cell. As noted earlier, this shutter must be a "free plate" that does not valve off the Knudsen cell chamber from the ionization chamber in any way.[63]
4. The appearance potential. These are tabulated and can be compared to the unknown.

5. The fragmentation pattern, which is known for some types of species. If the fragmentation pattern is not known, it must be studied by monitoring the ionization efficiency curves for all the ions in the system. Changes in these curves must be known with changes in the system composition.
6. Comparison to calculated/estimated vapor pressures for the condensed phase in the Knudsen cell. For a complex system with multiple vapor species, a Gibbs free energy minimization code can predict many of the expected species. FactSage[115] and ThermoCalc[116] include extensive solution databases and therefore give good approximations for complex alloys and oxide systems. It should be noted that these calculated compositions are for a perfect equilibrium, which does exist in a Knudsen cell. Nonetheless, these calculations provide a good guideline for which species might be observed. As an example, take a complex lunar basalt[117] and calculate the expected vapor species using the SLAG database in FactSage[115] at 2500 K. The results are presented in Table 1. The experimental study of De Maria et al.[118] reports observations of many of the predicted vapor species.

2.6 | Vacuum system

KEMS experiments necessarily must be conducted under high vacuum.[119] KEMS instruments have at least two differentially pumped stages—one for the Knudsen cell and furnace and one for the ionizer. The Knudsen cell chamber should have a higher-speed pump and, as noted, is separated by a Cu plate and/or cold trap. The speed of this pump is determined by the necessity to pump away effusing permanent gases from the Knudsen cell. Condensates from the Knudsen cell should collect in this chamber and not the ionizer chamber, which limits any "memory" effects. The ionizer chamber is typically much cleaner.

The significant advances made in vacuum technology over recent years have enhanced modern KEMS instruments.[120] Vacuum systems—including the high-vacuum and fore-vacuum pumps—are now available as completely oil free, which will minimize background in a sensitive mass spectrometer. The pumping system shown in Figure 1 is illustrative of the number of pumps needed for a magnetic sector instrument: there is a large turbomolecular pump (500 L/s) in

TABLE 1 Predicted vapor species of a lunar basalt at 2500 K (from FactSage[115] calculations) compared to experimentally observed species reported by De Maria et al.[118]

			Predicted and observed species from lunar basalt sample 12022	
Chemical analysis (Snyder et al.[117])[a]		Species	Partial pressure (bar)	Vapors observed (De Maria et al.[118])
SiO_2	43.2	PO_2(g)	0.004569408	
TiO_2	5.16	SiO(g)	0.004541139	✓
Al_2O_3	9.04	Fe(g)	0.003317841	✓
FeO	21.44	Na(g)	0.002800994	✓
MnO	0.25	PO(g)	0.001925179	
MgO	10.43	K(g)	0.000794608	✓
CaO	9.56	FeO(g)	0.00031189	
Na_2O	0.47	O(g)	0.000156368	✓
K_2O	0.07	O_2(g)	0.000116427	✓
P_2O_5	0.13	Mg(g)	0.000107833	✓
		SiO_2(g)	6.14219E-05	✓
		TiO_2(g)	7.34285E-06	✓
		P(g)	3.85922E-06	
		KO(g)	1.08059E-06	
		TiO(g)	2.00284E-07	✓
		Ca(g)	1.0955E-07	✓
		CaO(g)	1.8925E-08	
		Al(g)	3.66595E-09	✓
		Si(g)	3.17871E-09	
		K_2(g)	8.01489E-10	
		Ti(g)	1.85167E-11	
				Cr
				AlO
				Al_2O

[a]3300 ppm by weight Cr (form not clear and not included in calculations).

the Knudsen cell/furnace chamber, another turbomolecular pump (240 L/s) in the ionization chamber, an ion pump (50 L/s) in the ion sorting region, and an ion pump (50 L/s) in the detector.

Most newer systems use turbomolecular pumps. However, modern diffusion pumps and oils are still less expensive and offer the advantage of uniform pumping speeds for all gases. With proper liquid nitrogen traps and a liquid nitrogen cold finger, the background is minimal due to only normal outgassing of the housing materials. As noted, pumping speed in the Knudsen cell chamber is dictated by the requirement to pump permanent gases from the effusion cells. The SIMaP installation uses 800-L/s diffusion pumps each in the Knudsen cell and the ionization chamber. With a multiple cell effusing 4×10^{-4} mbar (Knudsen limit), the pressure in the Knudsen cell chamber reaches 4×10^{-5} mbar, and the ionization chamber remains undisturbed at 2×10^{-8} mbar. Note that the restricted collimation strongly limits gas exchange between the Knudsen cell chamber and the ionization chamber.

Many systems also have liquid nitrogen cold fingers in the ionization chamber that provide additional local pumping. High-speed, ultraclean cryo-pumps have been used in some KEMS systems with good success (Hildenbrand, private communication). Cryo-pumps may help with improving background gas pressures to obtain a larger range in the measurements of permanent gases such as oxygen and nitrogen effusing from within the Knudsen cell. A special case for trapping background gases in use is at SIMaP. Here a liquid nitrogen cold finger is in contact with the μ-metal ionization box. This setup, in association with restricted collimation, allows (1) the trapping of any high volatile vapors from the molecular beam, for example, P_4(g) and P_2(g) molecules in the vapor of InP,[121,122] and (2) the pumping of residual vapors that enter the ionization zone; for example, it was found that the addition of liquid nitrogen to this device decreases the peak at mass 28 by a factor of 80, and no peaks were detectable above mass 80.

Additionally, chambers of the instrument can be valved off and remain under clean vacuum when the rest of the system is opened to air; the system at NASA Glenn allows the ion sorting and detector regions to be valved off. As discussed earlier, other systems allow the region from the ionizer to the detector to be fully valved off and kept under vacuum at all times. This not only keeps the system cleaner and lowers the background spectrum but also allows the electronics to remain on and gives the instrument enhanced stability.

2.7 | KEMS systems in glove boxes

As previously noted, KEMS is particularly useful in nuclear applications, which necessarily involve the handling of radioactive materials. Several KEMS instruments in glove boxes exist worldwide.[72,123–125] A glove box can be used to either protect an air-sensitive sample from exposure before and during loading in the mass spectrometer or protect the user and environment from a hazardous sample. Glove boxes for the former are widely commercially available. Generally the glove box operates at a slight overpressure so that any gas flows outside and thus avoids glove box atmosphere contamination in case of leak or accidental opening of the confinement. Usually, an inert gas like nitrogen or argon circulates in a loop in the glove box and through passive or active filters cleaning the circulating gas from contaminants such as oxygen, water vapor, and solvent.

Next consider nuclear applications in which the glove box is necessary to protect the user from inhalation or ingestion of hazards. Nuclear-safe glove boxes are manufactured by specialized companies. These glove boxes are typically kept at a pressure that is lower than the laboratory environment. The under-pressure results in flow to inside the box in case of leak or accidental opening of the box and avoids the contamination of the outside atmosphere. As previously described for sample-protecting glove boxes, a cover gas circulates through the glove box with passive or active filters. It has been demonstrated that such systems can keep atmosphere to ppm levels for O_2 and H_2O.[126] Those glove boxes protect both users and samples.

Figure 14 shows the coupling of a glove box with a mass spectrometer. There are several things to consider in such a configuration:

1. The stability of the gas circulation system may have an impact on the stability of auxiliary instruments such as balances.
2. The use of a glove box induces severe limitations in terms of physical manipulation. The use of gloves limits operator dexterity in loading/unloading delicate samples and servicing the precision components, such as the ionizer.
3. The introduction of tools and instrumentation into the glove box may render them no longer useable for other tasks.
4. Some spectrometers may not be compatible with the glove box atmosphere. A very dry atmosphere can lead to electrostatic loading issues that would not occur at room humidity levels. This may affect electronics. Atmospheres such as argon may lead to insufficient cooling of the spectrometer due to the low thermal conductivity of argon. Very low oxygen potentials can even have an impact on spectrometer construction materials.

Points 1 and 4 can be addressed by monitoring and improving the stability of the circulating system as well as auxiliary cooling of the mass spectrometer. Alarms are especially important for contaminants in the circulating gas and for overtemperature.

2.8 | Data acquisition systems in KEMS

Data acquisition systems have developed rapidly in recent years. Many control aspects of a KEMS system can be automated, and data analysis can be run using a computer. Given the unique aspects of each system, KEMS systems tend to have custom-written software.[18,127,128]

Computer control of vacuum systems is well established. Many vacuum systems have automated pump-down procedures and alarms/

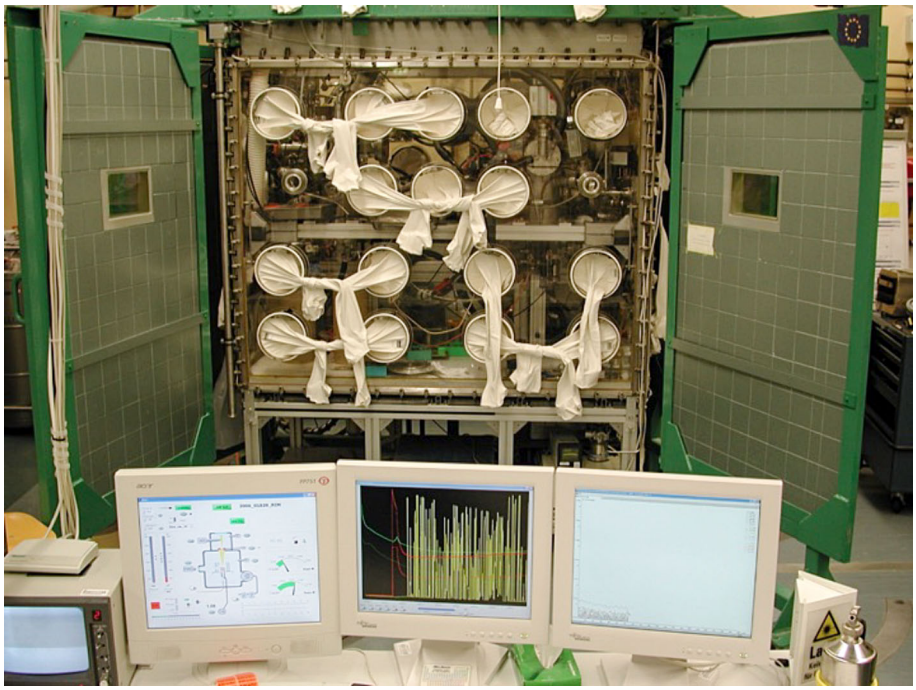

FIGURE 14 KEMS system in a nuclearized glove box with lead shields. [Color figure can be viewed at wileyonlinelibrary.com]

set points controlled by a computer. Commercial quadrupoles today nearly always include computer control of ion optics, the mass filter, and the detector. This can be combined with KEMS-specific software that controls the furnace, reads temperature from a thermocouple or pyrometer, controls cell position, and operates the shutter.[129] Most data systems transfer the data to a text file for analysis using commercially available spreadsheet and/or graphing programs.

Larger systems may use a single custom-written code. The data system for the NASA Glenn system has been described in Copland and Jacobson.[18] The current code is written in LabView (National Instruments, Austin, TX, USA), which offers much flexibility in the control of the instrumentation. In the NASA Glenn system, the following devices are controlled/monitored via computer:

1. Furnace. The control voltage and current to a resistively heated furnace can be controlled. Ramping of temperature is also possible.
2. Temperature measurement via pyrometer or thermocouple.
3. Stepper motors—for opening/closing the shutter and positioning cells.
4. Electron energy selector.
5. Magnet for selecting mass. The mass-to-charge ratio is

$$\frac{m}{q} = \frac{r^2 \tilde{B}^2}{2V} \tag{20}$$

Here m is the mass, q is the charge, r is the radius of the drift tube, $\tilde{B}$ is the magnetic field strength, and V is the accelerating voltage. Note that this equation is for an ideal situation; in practice the expression is more complex due to magnetic leaks. Generally the mass-to-charge scale is calibrated using standards of known mass numbers (e.g., inert gases) and fitted to a polynomial. Some instruments first select an approximate mass-to-charge ratio (m/q) with the magnetic field and then scan over a particular mass range with voltage. Care must be taken to scan over only a narrow voltage range to avoid sensitivity changes.
6. Electrometer for ion current signal measurement.
7. Ion counting for signal measurement. This includes control of the count interval (an accurate clock is part of the counting chain) and number of repetitive counts.

A KEMS/LabView application has also been developed at JRC Karlsruhe.[127] It is available in open source on GitHub (https://github.com). It includes the following:

- A user interface for live overview, experiment management, equipment configuration and control, metadata management, and text file saving.
- Instrument acquisition/control loops—simple acquisition, synchronized acquisition, complex control acquisition (e.g., furnace temperature control with furnace movement), and a mass spectrometer management loop.
- Full documentation of software.

The newly designed KEMS device which is currently developed at Mannheim University of Applied Sciences will use a software based on Siemens SPS System. The goal besides the aforementioned is to meet some standard procedures which can be reused for other groups who want to build up own slightly modified devices based on our experiences. The software allows maintenance from a distance as well as live demonstrations of the experiments which are advantageous also for teaching and academia.

In principle, many KEMS measurements can be fully automated. The instrument at KFA-Juelich has this capability for second law enthalpies. However, KEMS remains a research technique with many measurements that are quite system specific. Every thermochemical experiment must be run by the experimenter as a function of successive observations. Automation would be based on elementary actions specifically selected at each run. Full automation for every experiment remains elusive because these actions are specific to each experiment.

3 | MEASUREMENTS OF PARTIAL PRESSURES AND THERMODYNAMIC PROPERTIES USING KEMS

In this section we discuss actual KEMS measurements. The primary application of KEMS has been in physical chemistry, specifically the chemical thermodynamics of inorganic and some organic compounds. This is summarized in Figure 15. Chemical thermodynamics has changed in recent years due to the dramatic advances in computational quantum chemistry. We will show how modern quantum chemical calculations can be used in conjunction with KEMS to generate better data. In addition, KEMS can be a powerful tool in solution thermodynamics and used to generate model parameters.

3.1 | Thermochemistry of pure compounds

The principal reaction under study in KEMS is the transformation of a condensed phase into a vapor phase. Consider, for example, the vaporization of a solid pure element or compound A into its gas, with partial pressure, p_A. We assume congruent vaporization, in which the vapor has the same composition as the solid:

$$A(s) = A(g) \tag{21}$$

$$\Delta_v G_T^o = -RT\ln K_p = -RT\ln p_A = \Delta_v H_T^o - T\Delta_v S_T^o \tag{22}$$

Here $\Delta_v G_T^o$ is the free energy of vaporization, R is the gas constant, T is the absolute temperature, K_p is the equilibrium constant for reaction (21), $\Delta_v H_T^o$ is the enthalpy change associated with vaporization, and $\Delta_v S_T^o$ is the entropy change associated with vaporization. Thus a variety of thermodynamic quantities can be extracted from measurements of partial pressures of each species in the vapor. There are two primary methods to do this, the "second law" and the "third law" method. We shall discuss each of these.

3.1.1 | Second law thermodynamic method

The second law thermodynamic method to obtain an enthalpy of vaporization is probably the most common method used in KEMS. Taking the differential of Equation (22) gives the van't Hoff equation:

$$\frac{d\ln p_A}{d(1/T)} = -\frac{\Delta_v H_T^o}{R} \tag{23a}$$

Equation (15) can be combined with Equation (23a) leading to

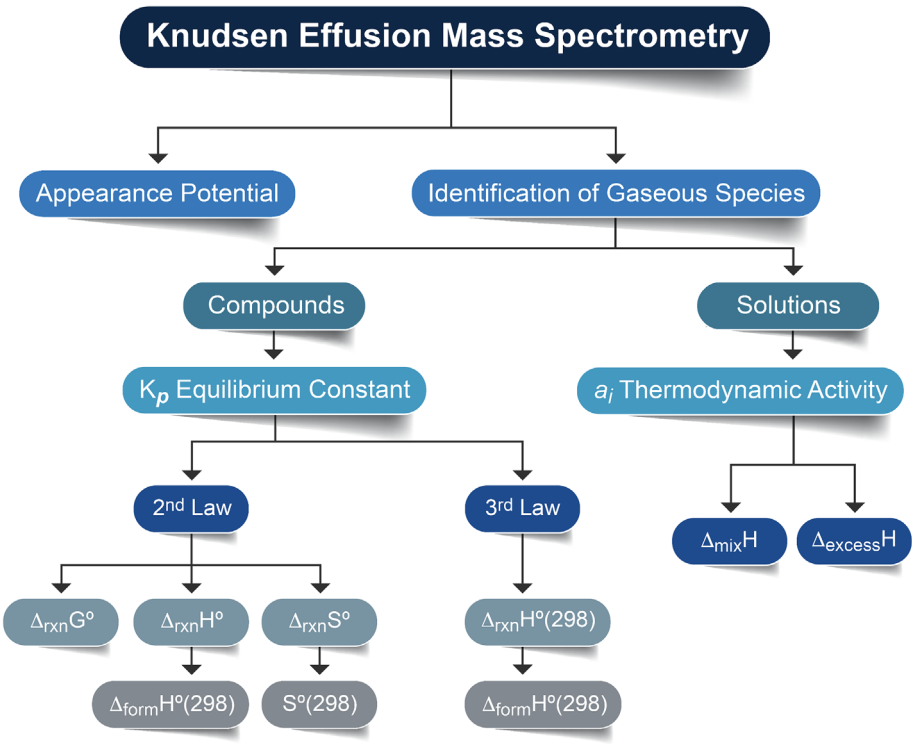

FIGURE 15 Thermodynamic properties commonly measured using KEMS (Knudsen effusion mass spectrometry). [Color figure can be viewed at wileyonlinelibrary.com]

$$\frac{d\ln I_A T}{d(1/T)} = -\frac{\Delta_v H_T^o}{R} \tag{23b}$$

Thus, the machine constant and ionization cross section become unnecessary to obtain an enthalpy of vaporization. Note the reliability of the slope is related to the stability of the slope and that depends on the constancy of MS sensitivity. If the machine constant and ionization cross section are known to sufficient accuracy that a vapor pressure can be accurately determined, then the *y*-intercept will give $\Delta_v S_T^o/R$.

Note that the enthalpy of vaporization is determined at the average temperature of the particular dataset. For comparison to other measurements and use in databanks, we need the enthalpy of vaporization at 298.15 K, $\Delta_v H_{298}^o$. This is the heat capacity correction:

$$\Delta_v H_{298}^o = \Delta_v H_T^o - \int_T^{298.15} \Delta_v C_p dT \tag{24}$$

Here, C_p is the heat capacity, which must be known for the gas and condensed phases.

Cater[24] describes the sigma method,[130] and other investigators have used a modified sigma method[131,132] as ways to extract $\Delta_v H_{298}^o$ from a dataset at higher temperatures. In the sigma method, a heat capacity change must be known as a polynomial. Consider a linear polynomial:

$$\Delta C_p = \Delta a + \Delta b T \tag{25}$$

Here Δa and Δb are symbols that define the heat capacity polynomial. A sigma function is then defined as

$$\Sigma = -R\ln K_p + \Delta a \ln T + \Delta b T/2 \tag{26}$$

A plot of Σ versus $1/T$ leads to a line with slope ΔH_I and intercept I. Then enthalpy and entropy at T can be calculated from

$$\Delta_v H_T^o = \Delta H_I + T\Delta a + \Delta b T^2/2 \qquad \Delta_v S_T^o = -I + \Delta a(1 - \ln T) + \Delta b T \tag{27}$$

Cubiciotti introduced a "modified sigma method,"[131] which is based on *gefs*.

$$gef_{298} = \left(\frac{G_T^o - H_{298}^T}{T}\right) \tag{28}$$

Thus, the equation can be written

$$\Delta[-(gef_{298})] - R\ln(p_A) = P + \frac{Q}{T} \tag{29}$$

Thus, a plot of the left-hand side of Equation (29) versus $1/T$ gives a slope Q equal to $\Delta_v H_{298}^o$ and intercept P equal to $\Delta_v S_{298}^o$.

These methods require heat capacities and/or *gefs*. In the earlier days of KEMS, many investigators obtained very good results by estimating heat capacities and *gefs* from estimated spectroscopic constants.[133,134] However, today these values are almost universally calculated using quantum chemistry.[135] In many cases the geometry, vibrational frequencies, and electronic states of the gas phase molecule in question[135] can be calculated using a relatively low level of theory. These are used to calculate the partition functions, which in turn are used to calculate heat capacities and *gefs*.[130] It was found that the *gefs* for metal hydroxide vapors were adequately calculated with density functional theory (DFT) using the B3LYP functional and augmented correlation consistent triple-ζ (aug-cc-pVTZ) basis sets.[136–138] More computationally intensive methods are required to directly calculate enthalpies of reaction and enthalpies of formation.

The best example of the second law thermodynamic method is the simple vaporization of a pure metal, as shown in Figure 16. The vaporization of Au and second law enthalpy is used as a frequent check for instrument operation—stability, temperature correction, and linearity of instrument between vapor pressure and the product of intensity and absolute temperature.

3.1.2 | Third law thermodynamic method

gefs are also necessary for the third law method. In essence, the third law thermodynamic method involves calculating the Gibbs free energy change at each temperature and subtracting the entropy to get an enthalpy. This can be written as

$$T\{\Delta[-(gef_{298})] - R\ln(p_A)\} = \Delta_v H_{298}^o \tag{30}$$

The major advantage of this method is that for every vapor pressure data point measured a $\Delta_v H_{298}^o$ is generated and that enthalpy is at 298 K. Typically, there are numerous measurements of $\Delta_v H_{298}^o$, which establish error limits. The quality of a third law measurement is, of course, dependent on the accuracy of the vapor pressure and temperature measured. It is also dependent on the quality of the *gef*. As previously noted, early studies would estimate *gefs* for molecules where spectroscopic data were not available. However, today these can be derived from quantum chemistry calculations with relative ease. A recent transpiration study on $CrO_2(OH)_2(g)$ shows that consistent second law, third law, and ab initio enthalpies were obtained using only *gefs* rigorously derived from current ab initio methods.[139]

It is best to do a second law thermodynamic analysis and a third law thermodynamic analysis. Standard deviations for both methods are generally published as proposed by Drowart et al.[87] However, these deviations do not reflect the total uncertainty that has to be analyzed and added to this standard deviation for the final results.

The results of a recent study are presented in Table 2.[15] In this study the following reaction was studied:

$$0.5Hf(s) + 0.5HfO_2(s) = HfO(g) \tag{31}$$

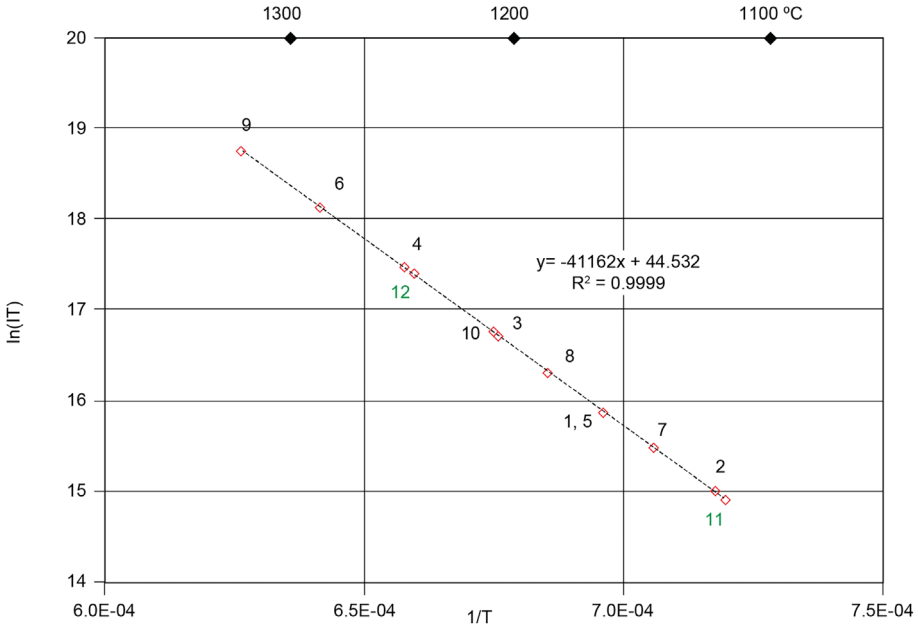

FIGURE 16 van't Hoff plot for enthalpy of vaporization of Au. [Color figure can be viewed at wileyonlinelibrary.com]

TABLE 2 Third law thermodynamic calculations for the reaction ½Hf(s) + ½HfO_2(s) = HfO(g), using $\sigma = 8.2 \times 10^{-10}$ m^2 and $k = 1.68 \times 10^{-23}$ bar-m^2/cps-K.

T (K)	*I* (cps)	Standard deviation	*IT* (cps K)	*kIT*/*σ* (bar)	−*RT* ln *Kp* (J/mol)	Δ*gef* (J/mol K)	Δ$_r$*H*°(298) = −*RT* ln *Kp* − *T* Δ*gef* (J/mol)
1934	170.4	8.3	329,553.6	6.75E-09	302,506.7	−162.57	616,914.8
1986	457.6	14.5	908,753.9	1.86E-08	293,891.9	−162.22	616,051.4
1957	296.1	18.7	579,448.1	1.19E-08	296,922.2	−162.41	614,763.3
1945	228.0	11.6	443,460.0	9.09E-09	299,426.7	−162.49	615,477.5
1994	519.9	25.7	1,036,640.7	2.12E-08	292,893.1	−162.16	616,241.7
2034	896.0	21.4	1,822,464.0	3.73E-08	289,227.5	−161.89	618,509.3
1952	264.5	14.4	516,245.4	1.06E-08	298,037.9	−162.45	615,133.3
2004	622.2	18.1	1,246,848.7	2.55E-08	291,285.7	−162.09	616,119.7

Ion intensities of HfO^+ were recorded from 1934 to 2034 K. A second law plot of ln(*IT*) versus 1/*T* yielded an enthalpy at 1976 K of −548.5 ± 22 kJ/mol. Using Equation (24) and the calculated heat capacity for HfO[15] and the tabulated heat capacity for Hf[115,140] and HfO_2,[115,141] an enthalpy of reaction at 298.15 K was calculated to be −633.0 ± 22 kJ/mol. The average of the third law enthalpies of reaction (taken at each temperature) was −616.2 ± 1.2 kJ/mol. Agreement is with 2.7%; however, the third law thermodynamic measurement is preferred as there are not sufficient data points or temperature range for a reliable second law enthalpy of reaction.

The enthalpy of reaction (31) can be combined with a reliable enthalpy of formation of HfO_2(s)[141] to calculate an enthalpy of formation of HfO(g). This can be compared to other measurements and theoretical calculations. The computed enthalpy of formation of HfO(g) using CCSD(T) (coupled cluster, single, doubles, with approximate triples) methods is 63.19 ± 10 kJ/mol compared to 58.4 ± 12.3 kJ/mol using third law methods with KEMS.[15]

3.1.3 | Dissociation energy of diatomic vapor species

One of the most useful thermochemical parameters derived from KEMS is the bond dissociation energy or simply the dissociation energy.[142–144] Consider the simple case of an element forming both a monomer (M) and a dimer (D) in the gaseous phase:

$$M(s) = M(g)\Delta_v H^o_0(M) \quad (32a)$$

$$2M(s) = M2(g)\Delta_v H^o_0(D) \quad (32b)$$

The enthalpies can be determined using either the second or third thermodynamic law methods described earlier. The dissociation energy, D^o_0, is thus given by

$$M2(g) = 2M(g) \qquad D_0^o = 2\Delta_v H_0^o(M) - \Delta_v H_0^o(D) \tag{33}$$

Similar equations can be written for gaseous molecules, AB(g). For example, consider the dissociation energy of SiO(g):

$$SiO_2(s) = SiO(g) + ½O_2(g) \text{ KEMS study} \tag{34}$$

$$Si(s) + O_2(g) = SiO_2(s) \text{ tabulated calorimetric data} \tag{35}$$

$$Si(g) = Si(s) \text{ tabulated or KEMS study} \tag{36}$$

$$Si(g) + ½O_2(g) = SiO(g) \qquad -D_0^o(SiO) \tag{37}$$

Drowart and colleagues have made use of isomolecular-exchange reactions to determine dissociation energies,[145] such as

$$YO(g) + Sc(g) = Y(g) + ScO(g) \tag{38}$$

This reaction was set up with mixtures of $Sc_2O_3 + Y$ in the Knudsen cell. The dissociation of YO(g) is known, and thus the dissociation energy of ScO(g) could be measured.

There are many KEMS studies on dissociation energies in the literature that report dissociation energies.[143,146,147] These can be directly compared to the values obtained using various computational methods.[148,149] In the case of CsI(g) and its dimer, Roki et al.[150] compiled experimental enthalpy values, assessed these values, and compared to different ab initio calculations. The evaluated experimental uncertainty is within the range of values for the calculations.

3.2 | Thermochemistry of solutions

Vapor pressure measurements lead to fundamental solution properties. We shall first discuss these measurements for metallic alloys. There are several reviews specifically on this topic.[6,18,151,152]

The primary solution parameter to be measured is the thermodynamic activity of components. Activity of component A(a_A) is defined as the change in chemical potential of component A(μ_A) as component A moves from solution phase β to its pure phase, designated by superscript ^{o}:

$$\Delta_{mix}\overline{G}_A^\beta = \Delta_{mix}\overline{H}_A^\beta - T\Delta_{mix}\overline{S}_A^\beta = \mu_A^\beta - \mu_A^o = RT\ln\frac{f_A^\beta}{f_A^o} = RT\ln\frac{p_A^\beta}{p_A^o} = RT\ln a_A^\beta \tag{39}$$

The reference state is arbitrary but must be clearly defined. It is often in the form of the pure element at the temperature of interest, which may be a particular crystalline structure (e.g., face-centered cubic Ni) or liquid (e.g., Al(*l*)). For the component A in a mixture (A,B), let us assume the reference state as the A(δ phase). We can write the appropriate chemical reactions as follows. For the pure component,

$$A(\delta) = A(g) \qquad \Delta_{vap}G^o(\delta) = -RT\ln\frac{p_A^o}{a_A(\delta)} = -RT\ln p_A^o \tag{40}$$

For the mixture at the same temperature, we have

$$A(\text{in}\,A,B,\gamma) = A(g) \qquad \Delta_{vap}\overline{G}^o(A(\gamma)) = -RT\ln K_p(T) = -RT\ln\frac{p_A}{a_A} \tag{41}$$

Combining Equations (39)–(41) gives

$$a_A(\text{in}\,A,B,\gamma,\text{wrt}\,\gamma) = \frac{p_A}{p_A^o} \tag{42}$$

Thus, any measurement of the A(g) species partial pressure over a mixture must be reported with a convenient reference to determine the activity of A. Applying thermodynamic relations, the variation in the logarithm of a_A versus $1/T$ leads to the partial mixing enthalpy of A, $\Delta_{mix}\overline{H}_A^\gamma$:

$$\frac{d\ln a_i}{d(1/T)} = -\frac{\Delta_{mix}\overline{H}_A^\gamma}{R} \tag{43}$$

This relation is similar to the second thermodynamic law equation for enthalpy of reaction of a pure substance, as discussed earlier. The calculated partial enthalpy of mixing, together with its uncertainty, may be compared to other types of measurements (e.g., calorimetry). Note that in optimizing procedures for phase diagram and associated data calculation, the activities of components and their derivatives cannot be used together as they are not independent.

If the partial molar enthalpy of mixing is known for all n components, the integral molar enthalpy of mixing may be derived:

$$\Delta_{mix}H^\beta = \sum_{k=1}^{n} x_i\Delta_{mix}\overline{H}_i^\beta \tag{44}$$

Note that the excess partial enthalpy is given by[153]

$$\Delta_{exc}\overline{G}_A^\beta = RT\ln\gamma_A^\beta = \Delta_{exc}\overline{H}_A^\beta - T\Delta_{exc}\overline{S}_A^\beta \tag{45}$$

Here γ_A^β is the activity coefficient of A in phase β, defined as $\gamma_A^\beta = a_A^\beta/x_A^\beta$. The partial molar excess enthalpy of component A can be determined from

$$\frac{d\ln\gamma_A}{d(1/T)} = -\frac{\Delta_{exc}\overline{H}_A^\beta}{R} \tag{46}$$

The integral molar excess enthalpy is thus given by

$$\Delta_{exc}H^\beta = \sum_{k=1}^{n} x_i\Delta_{exc}\overline{H}_i^\beta \tag{47}$$

Equations (42)–(47) show the range of key solution data that can be obtained via KEMS. Further, Equations (44) and (47) show that

partial molar quantities of components can be combined to determine integral molar quantities. These can be compared to integral quantities measured using other techniques (e.g., calorimetry). The most reliable thermodynamic data are verified via several methods as well as theoretical calculations. For example, the Ti–Al system has been studied using KEMS, and the derived integral molar enthalpy compares favorably to calorimetry measurements.[154,155] Similar favorable comparisons between KEMS and calorimetry measurements have been reported for some rare-earth oxide–silica systems.[14,156]

3.2.1 | Thermochemistry of solutions: Direct measurements of thermodynamic activity of components

From Equation (42), it follows that the most direct measurement of the component activity is simply to compare the vapor pressure of a component over the alloy to the vapor pressure of the pure component:

$$a_A = \frac{p_A}{p_A^o} = \frac{I_A T S_A}{I_A^o T S_A^o} \frac{C_I}{C_{II}^o} = \frac{I_A}{I_A^o} \mathrm{GFR} \tag{48}$$

The terms a_A, I_A, and T have been described previously. GFR is the geometry factor ratio from the geometry factors of the two cells, c_I and c_{II}. Although the two cells are machined to the same dimensions, there are still microscopic orifice differences; these are accounted in the GFR. The GFR is determined by comparing ion intensity measurements in the mass spectra of the vapor for an identical substance held in each cell and should be 0.98 or better. The key parameter determining the effectiveness of the direct comparison method is the ratio of the machine constants, $\frac{S_A}{S_A^o}$. Ideally this should be constant across multiple measurements. In reality, the machine constant will change when the sample is changed due to such factors as the size and location of the ionization volume, the position of the molecular beam in the region that is sampled by the mass spectrometer, and the exact position of and heat distribution at the orifice of the Knudsen cell. Note that there is a possible surface contribution to the flux from surface diffusion through the orifice. This would depend on the alloy composition, so that one GFR may not fully correct for surface diffusion across the alloy composition range.

The general problem of varying machine constant from run to run has been circumvented in several ways. The first approach is to design the instrument for stability between runs, which includes rigidly fixing cell position for a fixed ionization volume.[157] A special valve between the chamber with Knudsen cell furnace[7,72] also leads to enhanced stability. This has been described in Section 2.1.4. However, note that a unity value for the ratio $\frac{S_A}{S_A^o}$ cannot be strictly assumed because the ionization volume is defined by the entire device and not cell positioning alone.

Another method to limit the issue of variation in the machine constants is to use a multiple-cell system, as discussed in Section 2.1.4. A multiple-cell system involves two or more cells in a constant temperature holder within the furnace. The cells are translated to/from the mass spectrometer sampling region via controls external to the vacuum system. The physical form of a multiple-cell system was discussed in the first part (Figure 5) of this review. Such systems have the advantage of an in situ temperature calibration and vapor pressure calibrant/standard state. The component activity is the ratio of the ion intensities, as given in Equation (48) with a GFR correction near unity. When using a restricted collimation device associated with a multiple cell, the only parameter that can lead to a different pressure reading is a different temperature. This should be minimal in a properly designed isothermal heating block.[158]

Often, it is not possible to have the exact reference state present in an adjacent cell. An example of this is pure aluminum, which has a vapor pressure too high at the temperature necessary to study some aluminum-containing alloys. In this case, a similar metal, such as gold, would be used. Equation (48) becomes

$$a_A = \left[\frac{p_A}{p_{Au}^o}\right]_T \left[\frac{p_{Au}^o}{p_A^o}\right]_T = \left[\frac{I_A}{I_A^o}\right]_T \left[\frac{\sigma_{Au}}{\sigma_A}\right] \frac{C_I}{C_{II}^o} \left[\frac{p_{Au}^o}{p_A^o}\right]_T \tag{49}$$

The subscript T indicates that both quantities in the brackets are determined at the same temperature. In this approach, the ratio of the vapor pressure of gold to the vapor pressure of the pure component is determined from the appropriate data tables.[140,141,159,160] In a mass spectrometer free from mass discrimination effects in the ionizer, ion sorter, and detector, the only instrument sensitivity changes are due to the ionization cross sections, which can also be taken from tabulations and corrected for the particular electron energy used.[87,91]

A third method of circumventing the problem of varying machine constants is to combine a KEMS instrument with another type of technique, for example, target collection or thermogravimetric analysis.[161] In this case, the in situ weight loss measurement gives an independent calibration method. In situ calibration by target collection of part of the molecular beam in the mass spectrometer has been used by Drowart et al.[162] for U-O, U-C, and U-N studies. Calibration via target collection or thermogravimetric measurement needs to correct for the effects of surface diffusion and vaporization from surfaces other than the effusion orifice.

3.2.2 | Thermodynamics of solutions: Ion current ratio method in mass spectra of a vapor over an alloy

There are several methods that circumvent this problem of nonreproducible calibration constants using a single cell. The ion current ratio technique was developed by Lyubimov,[163] Neckel and Wagner,[164] and Belton and Fruehan.[165,166] Belton and Fruehan[166] have extended the method from binary to ternary alloys; Korobov et al.[167] extended the method to include intermediate line compounds. The method is based on the Gibbs–Duhem relationship. Consider a system of n components:

$$0 = \sum_{i=0}^{n} x_i d\overline{G}_i \tag{50}$$

For a two-component system, this becomes

$$0 = x_1 d\overline{G}_1 + x_2 d\overline{G}_2 = x_1 d\ln a_1 + x_2 d\ln a_2 = x_1 d\ln a_1 + (1 - x_1) d\ln a_2$$
$$= d\ln a_2 + x_1 d\ln \frac{a_1}{a_2} = d\ln a_2 + x_1 d\ln\left(\frac{I_1}{I_2}\right) \tag{51}$$

Note that the ratio of the component activities in principle cancels the ionization cross section and machine geometrical constant terms. Integrating gives the component activity and activity coefficient of that component:

$$\ln a_2 = -\int_{x_1=1}^{x_1=x_1} x_1 d\ln\left(\frac{I_1}{I_2}\right) \tag{52}$$

This can be converted to the following expression, which can be readily graphically integrated[165]:

$$\ln \gamma_1 = -\int_{x_1=1}^{x_1=x_1} x_1 d\left[\ln\left(\frac{I_1}{I_2}\right) - \ln\left(\frac{x_1}{x_2}\right)\right] \tag{53}$$

Analogous to Equation (43), the partial molar enthalpy of component 1 can be derived as

$$\Delta_{mix}\overline{H}_1^{\beta} = -R \int_{x_1=1}^{x_1=x_1} x_1 d\left[\frac{\ln\left(\frac{I_1}{I_2}\right)}{d\left(\frac{1}{T}\right)}\right] \tag{54}$$

This method involves the preparation of a series of alloys across a composition range and then measurement of ion current ratios in the mass spectra of a vapor over an alloy as a function of temperature for each alloy. It has proven to be an accurate method, and many systems have been reported in the literature.

As noted earlier, these equations can be extended to ternary systems as well.[166,168] The Gibbs–Duhem relation leads to two graphical integrations with expressions similar to Equation (53) for components 1 and 2, 2 and 3, and 1 and 3. Integrations are along lines of constant molar ratio of components.

3.2.3 | Thermodynamics of solutions: Dimer–monomer vapor species ratio method

Another single-cell method that circumvents the problem of nonconstant machine constants is the dimer–monomer vapor species ratio method. Berkowitz and Chupka[169] developed this method for salt mixtures; however, it applies to metallic alloys and oxide systems as well. Many materials have a monomer–dimer equilibrium in the gaseous phase:

$$A_2(g) = 2A(g) \tag{55}$$

$$K_p = \left(\frac{P_A^2}{P_{A_2}}\right) = P_A\left(\frac{P_A}{P_{A_2}}\right) \tag{56}$$

This equilibrium can be measured for both the pure component A and an alloy containing A. The gas phase equilibrium (Equation 55) must, of course, have the same equilibrium constant for both pure A and an alloy containing A at the same temperature. The activity of component A in an alloy containing A becomes

$$a(A) = \frac{P_A^{alloy}}{P_A^o} = \frac{\left(\frac{P_A}{P_{A_2}}\right)^o}{\left(\frac{P_A}{P_{A_2}}\right)^{alloy}} = \frac{\left(\frac{I_A}{I_{A_2}}\right)^o}{\left(\frac{I_A}{I_{A_2}}\right)^{alloy}} \tag{57}$$

Note that the ionization cross sections of the vapor species and the geometrical constants all cancel, so that only the ratios of ion intensities from the mass spectra of the vapor over the alloy and pure compound are needed.

3.2.4 | Alloy thermodynamics via KEMS: General considerations

Many considerations must be taken into account for reliable component activity measurements of alloys. In principle, if the component under study generates a vapor pressure within the KEMS measurement range, a component activity can be measured. KEMS also has the unique advantage of permitting multiple component activities to be measured simultaneously.

Complications arise from component loss through the cell orifice. This, of course, is a bigger issue when considering narrow phase widths and line compounds. Weight, composition, and XRD measurements should be conducted before and after every run to verify that all measurements are taken in the same phase region. In this case isothermal runs are conducted, and the instantaneous composition is determined by integration of the products $I_i^+\sqrt{T}dt$ associated with the mass loss of the sample. Pattoret et al.[170] have conducted such a study for the nonstoichiometric domain of $UO_{2\pm x}$. Note the evolution of the gaseous phase yield information on the variance of the system and consequently the number of phases throughout the mass spectrometric analysis.[171]

Experiments can be modified to utilize the component activity changes with composition in the system under study. A proposed instrument with an integral hot-stage XRD system to monitor phase changes would help with this. There would obviously be many complexities in such a system, but it would also offer the advantage of monitoring vapor pressures with simultaneous identification of the phases.

Howard[172] and Oktay[173] have developed a "valved Knudsen cell mass spectrometer." This instrument allows alloying elements to be added to the Knudsen cell and the component activities in the resulting liquid alloy to be measured as a function of composition. This is similar to the phase changes observed by Drowart et al.[171] over long times.

It is possible to leverage the phase rule to create a univariant system, which is easy to study. The phase rule is generally written as

$$f = c + 2 - p \tag{58a}$$

Here, f is the degrees of freedom, c is the number components, "2" comes from the fixed pressure and temperature, and p is the number of phases, which is typically two for the solid and vapor. In a KEMS experiment the temperature is fixed, so Equation (58a) for a single phase becomes

$$f = c + 1 - p \tag{58b}$$

Thus, a simple unary system ($c = 1$, $p = 2$) has all degrees of freedom set with a constant temperature. For a binary system, all degrees of freedom are set with two solid phases (or solid + liquid) and the vapor phase ($p = 3$):

$$f = 2 + 1 - 3 = 0 \tag{58c}$$

This method has been used in the ceramic systems Y_2O_3-SiO_2[14] and Yb_2O_3-SiO_2.[156] In these cases, there are two distinct solid phases and a gas phase. For a solid solution $p = 2$ and $f = 1$. The degrees of freedom can be reduced to zero if there is an additional relationship that links the solid and gas compositions. This is the case if a pseudo-congruent relationship fixes the pressure of each gaseous species. This relationship is known as the "effusion flow composition," which must be the same in the pseudo-binary section as in the condensed phase.[174] For ternary systems, all degrees of freedom are set with three solid phases and a vapor phase ($p = 4$):

$$f = 3 + 1 - 4 = 0 \tag{58d}$$

A Ni–Al–O ternary study led to highly reliable data[175] as a function of temperature, as long as the system remained univariant.

A wide range of metallic alloys have been studied using KEMS. For the aforementioned reasons, most of these are binary alloys, although some are ternary alloys. The techniques discussed previously have all been used to generate this range of data. The studies on nickel alloys have important applications to superalloys. Today's complex CALPHAD (calculation of phase diagrams) nickel alloy databases are built on robust assessments of the binary and ternary systems.[176] The Ni–Al system is interesting from both a practical point of view and a basic science point of view. The β-NiAl phase exhibits dramatic changes in activities of Ni and Al over a narrow composition range[177–180] (Figure 17), and the γ′ Ni_3Al phase is the basis for superalloys. Recent measurements of component activities for complex alloys have been reported.[181,182] These are very useful as long as the phase of the measured alloy is known.

Other aluminide binaries acting as the basis for currently developed or potentially useful alloys are Ti–Al, Fe–Al, and Nb–Al. Oxygen solubility is a big issue with Ti and its alloys. Copland et al.[183] have examined Ti–Al–O alloys to study the effect of oxygen concentration on the activity of Ti and Al (see Figure 18). These results provide inferences about the structure.[183]

3.2.5 | Oxide systems: Compounds and solutions

Oxide compounds and solutions are important in a variety of metallurgical (e.g., slags in steel making), processing (e.g., glasses), and geological (e.g., magmas) applications.

KEMS can be used to obtain a component activity in an oxide mixture. Activities of components in the system under consideration are measured using methods like those discussed for alloys. For an oxide component that vaporizes congruently with the same vapor molecule as the compound, the component activity is simply the ratio of the vapor pressure of the vapor species above the solution to that above the pure oxide. For a decomposing oxide, the component activity can be determined from the equivalency of the equilibrium constants. In a multiple-cell experiment,[184] consider alumina, Al_2O_3, which decomposes primarily to Al(g) and O(g) at high temperatures:

$$Al_2O_3(\text{pure}) = 2Al(g) + 3O(g) \qquad K_p(T) = \frac{P^2_{Al}(\text{pure})\,P^3_O(\text{soln})}{1} \tag{59a}$$

$$Al_2O_3(\text{soln}) = 2Al(g) + 3O(g) \qquad K_p(T) = \frac{P^2_{Al}(\text{soln})\,P^3_O(\text{soln})}{a(Al_2O_3)} \tag{59b}$$

$$a(Al_2O_3) = \frac{P^2_{Al}(\text{soln})\,P^3_O(\text{soln})}{P^2_{Al}(\text{pure})\,P^3_O(\text{pure})} = \frac{I^2_{Al}(\text{soln})\,I^3_O(\text{soln})}{I^2_{Al}(\text{pure})\,I^3_O(\text{pure})} \tag{59c}$$

Here, $K_p(T)$ is the equilibrium constant for both reactions, which are equal at constant temperature; $P_i(\text{pure})$ is the partial pressure of the species i over pure Al_2O_3; $P_i(\text{soln})$ is the partial pressure of the species i over Al_2O_3 in solution; $I_i(\text{pure})$ is the ion intensity of the species i over pure Al_2O_3; $I_i(\text{soln})$ is the ion intensity of the species i over Al_2O_3 in solution; and (Al_2O_3) is the activity of Al_2O_3. In these equations, instrument sensitivities to the different species have been omitted as they are equal in the multiple-cell instrument. Note that, as with metallic alloys, component activities can be measured in complex, multicomponent oxide systems and glasses and that a convenient reference state must be selected.

Following the publication of the monograph by Stolyarova and Semenov,[5] a number of reviews dealing with the vaporization and thermodynamic properties of oxide systems studied using KEMS at high temperatures have been completed.[185–202] The general overview in this area was presented in the series of publications from decade to

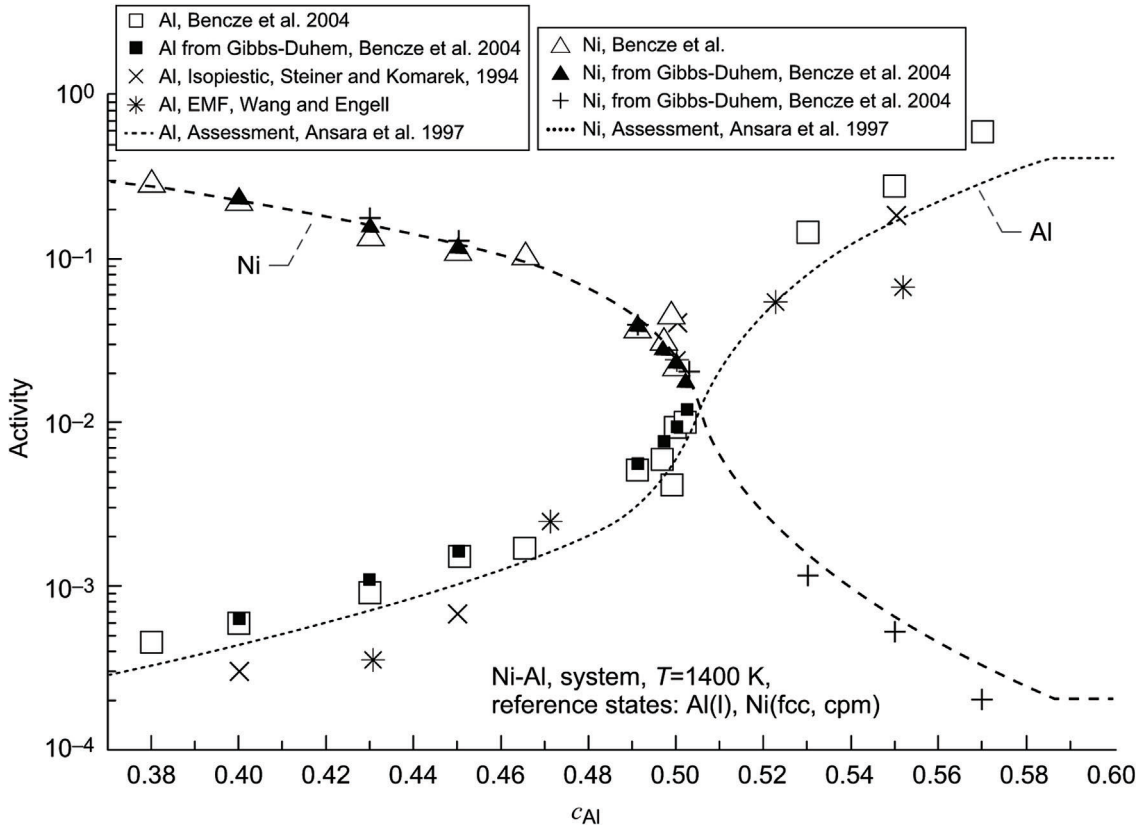

FIGURE 17 Activity as a function of composition for β-NiAl. *Source*: Reprinted from Bencze et al.[177] with permission from Springer Nature.

decade.[185–190] We can delineate them into three main groups: glass-forming oxide systems,[191–196] ultrahigh-refractory oxide systems mainly based on HfO_2,[197–199] modeling approaches developed using the Knudsen effusion mass spectrometric thermodynamic data on oxide systems for the prediction of their high-temperature behavior,[189,193–196,200,201] and comparison to thermodynamic data that may be obtained at high temperatures using KEMS and differential thermal analysis.[202] During the period indicated from 1994, systematic studies on the thermodynamic properties of the gaseous oxide salts or associates were successfully continued as the development of a scientific school founded by G. A. Semenov. Reviews by Lopatin and Shugurov[203–209] illustrate the recent achievements in studies on thermodynamic properties and the identification of the variety of the gaseous associates in high-temperature vapor using KEMS.[203–209]

It should be mentioned that, although not included in the reviews discussed earlier, recent experimental data obtained using KEMS at high temperatures on oxide systems and materials for nuclear applications such as the UO_2-ZrO_2,[67,210] Cs_2O-B_2O_3,[211] Cs_2O-MoO_3,[212] and SrO-Al_2O_3[213,214] systems are available. Recent KEMS data on ceramics and glass ceramics with the special unique physicochemical properties such as the ZnO-Nb_2O_5,[215] TiO_2-Al_2O_3-SiO_2,[216,217] and Al_2O_3-SiO_2-ZrO_2 systems[218] as well as ultrahigh refractory ceramics based on the binary and multicomponent systems containing rare-earth and hafnium oxides[219–221] have also been reported. It is necessary to emphasize that the thermodynamic properties obtained in all these systems were discussed within the framework of semiempirical and statistical thermodynamic approaches for modeling and prediction of thermodynamic properties of multicomponent systems based on the corresponding data on binary systems. Additionally, phase diagrams for the ZnO-Nb_2O_5[215] and the Al_2O_3-SiO_2-ZrO_2 systems[218,222] were optimized and calculated. Examples of component isoactivity curves and Gibbs energy of formation in the Al_2O_3-SiO_2-ZrO_2 system are shown in Figure 19A–D based on experimental data and modeling provided in Stolyarova et al.[218]

We next focus on the latest experimental data on the vaporization and thermodynamic properties of binary and multicomponent systems containing rare-earth and hafnium oxides.[197–199,219–225] In recent years, the composition of vapor, the temperature dependences of partial pressures of the vapor species, and the thermodynamic properties of vaporization of the following individual pure rare-earth oxides have been studied: Y_2O_3, La_2O_3, CeO_2, Nd_2O_3, Sm_2O_3, Gd_2O_3, Yb_2O_3, and Lu_2O_3. The study of the high-temperature behavior of Sm_2O_3 deserves special mention, as data on the composition and partial pressures of vapor species over Sm_2O_3 in a wide temperature range have not been previously published in the literature. When comparing the excess Gibbs energies at 2373 K in the La_2O_3-HfO_2, Nd_2O_3-HfO_2, Sm_2O_3-HfO_2, and Gd_2O_3-HfO_2 systems as well as in the La_2O_3-Y_2O_3, ZrO_2-Y_2O_3,

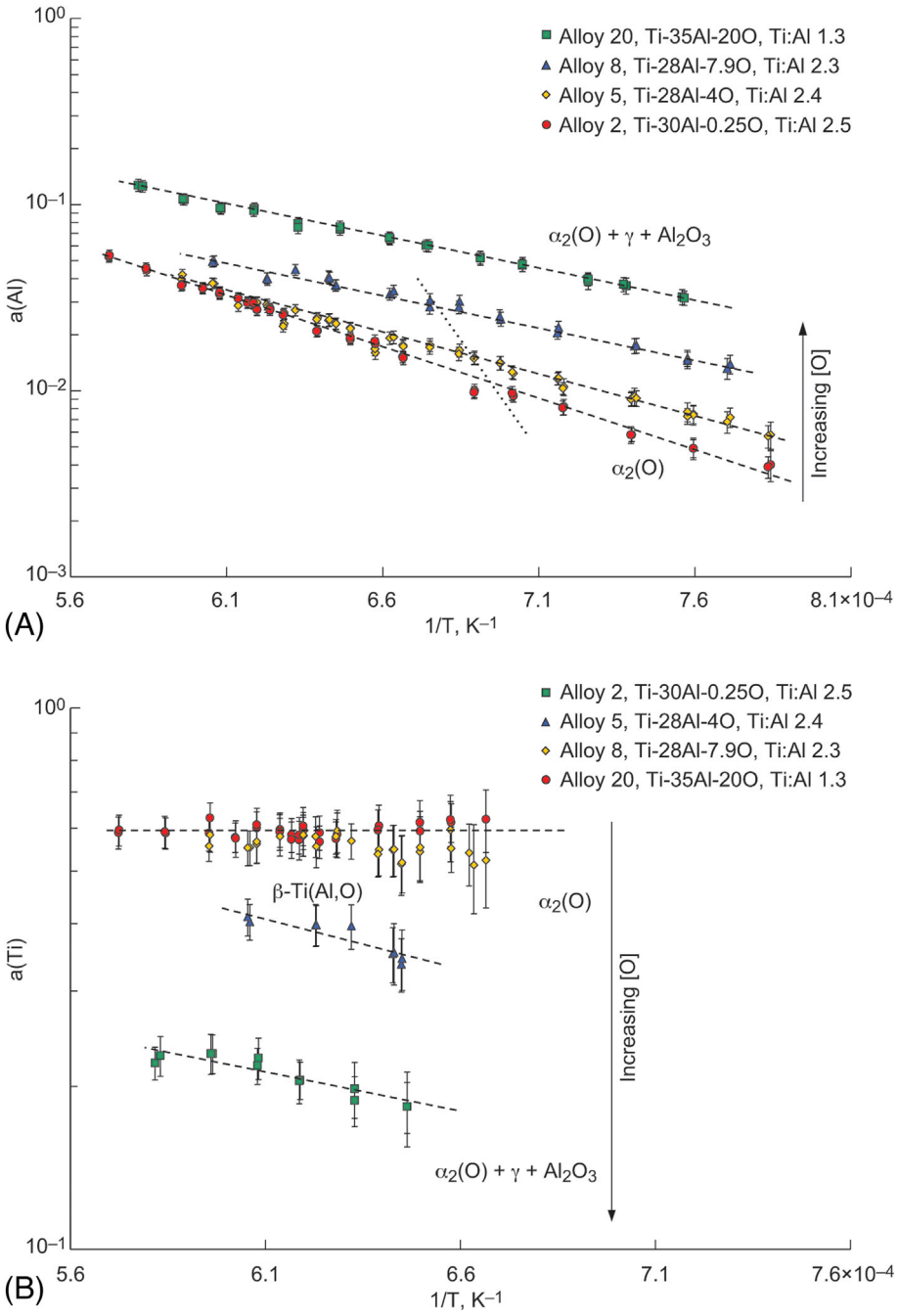

FIGURE 18 Activity as a function of composition for different [O] with constant Ti–Al ratio. (A) Activity of aluminum (B) Activity of titanium. *Source:* Reprinted from Copland et al.[183] with permission from Elsevier. [Color figure can be viewed at wileyonlinelibrary.com]

Sm_2O_3-Y_2O_3, and Gd_2O_3-Y_2O_3 systems, it was found that there is a correlation between the electronic structure of lanthanide oxide and the degree of negative deviation from ideal behavior.

Special attention should be paid to the study of evaporation processes and thermodynamic properties in ternary systems based on hafnium and rare-earth oxides (e.g., La_2O_3-Y_2O_3-HfO_2, Gd_2O_3-Y_2O_3-HfO_2, and Y_2O_3-ZrO_2-HfO_2) using KEMS at high temperatures. In these systems, the partial pressures of the vapor species, the evaporation rates of the samples, the activities of the components, and the excess Gibbs energies were obtained for the first time. In the La_2O_3-Y_2O_3-HfO_2 and Y_2O_3-ZrO_2-HfO_2 systems, the concentration changes in the samples due to the selective evaporation of the components at temperatures of 2337 and 2660 K, respectively, were also evaluated. Similarly, the evaporation rates and changes in the contents of components in the samples during isothermal holding in the Sm_2O_3-Y_2O_3-HfO_2, Sm_2O_3-ZrO_2-HfO_2 and Gd_2O_3-ZrO_2-HfO_2, and Gd_2O_3-ZrO_2-HfO_2 systems were compared. It is shown that at a temperature of 2373 K, the evaporation rates of samples in the Sm_2O_3-Y_2O_3-HfO_2 and Sm_2O_3-ZrO_2-HfO_2 systems are similar, and the least volatile system is Gd_2O_3-ZrO_2-HfO_2, which is consistent with the lower volatility of Gd_2O_3 compared to Sm_2O_3.

Among the modeling approaches used to calculate the thermodynamic properties of multicomponent systems, the appropriate semiempirical methods and statistical–thermodynamic

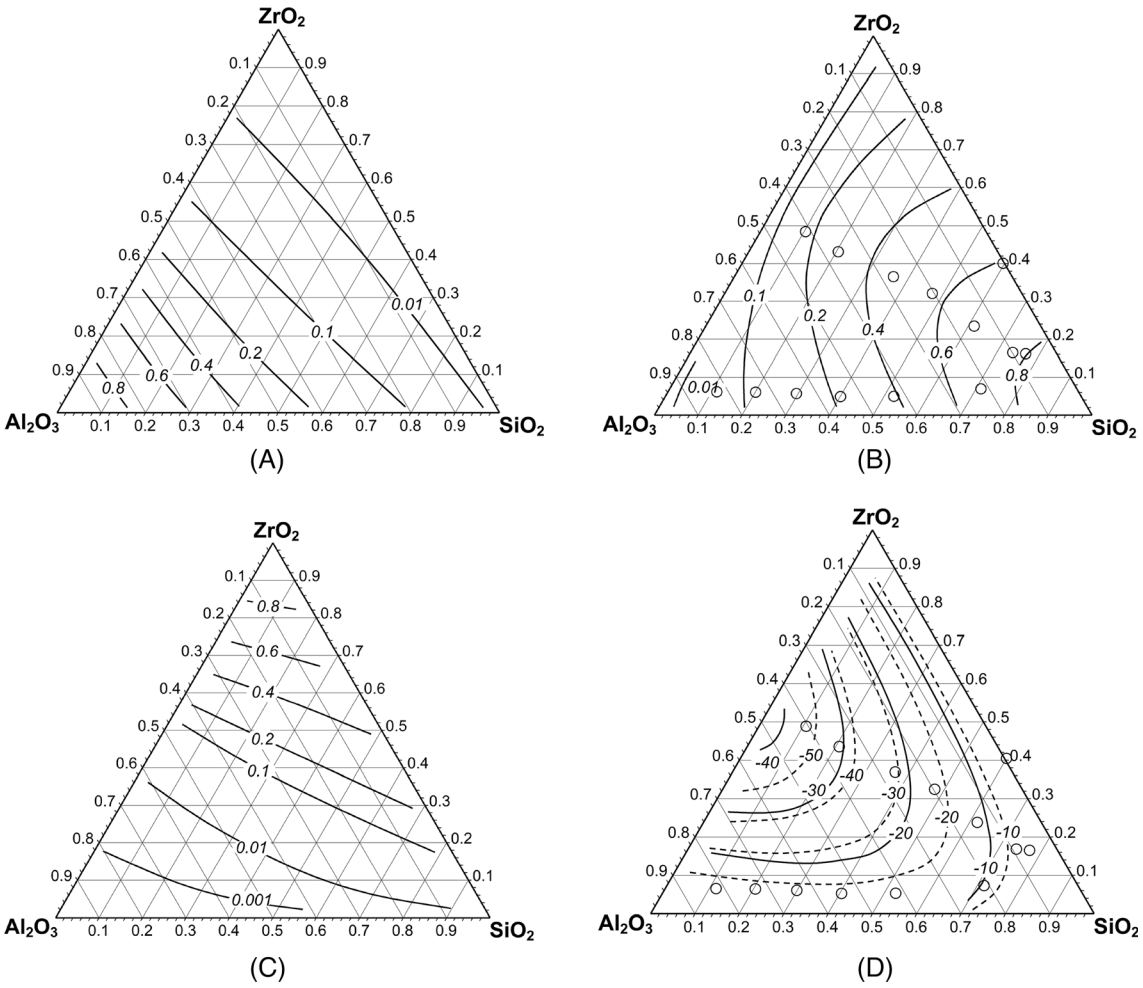

FIGURE 19 (A) The Al_2O_3 isoactivity curves in the Al_2O_3-SiO_2-ZrO_2 system calculated using Generalized Lattice Theory of Associated Solutions (GLTAS) at 2500 K.[218] (B) The SiO_2 isoactivity curves in the Al_2O_3-SiO_2-ZrO_2 system calculated using GLTAS at 2500 K. The circles indicate the sample compositions for which the experimental values were obtained.[218] (C) The ZrO_2 isoactivity curves in the Al_2O_3-SiO_2-ZrO_2 system calculated using GLTAS at 2500 K.[218] (D) The curves of constant ΔG^E (kJ/mol) calculated within the GLTAS approach at 2500 K using the SiO_2 activity experimental data in the Al_2O_3-SiO_2-ZrO_2 system (solid lines) and the SiO_2 and Al_2O_3 activity data for the binary SiO_2-ZrO_2 and Al_2O_3-ZrO_2 systems (dashed lines).[218]

models must be selected. A significant limitation of semiempirical methods is the inability to obtain information on the structure of the solutions for which the calculations of thermodynamic properties are carried out; additionally, it is impossible to consider the temperature dependence of thermodynamic properties if they are not available for the corresponding binary systems. Statistical–thermodynamic approaches, on the contrary, allow both modeling thermodynamic properties and relating physicochemical characteristics to structure. Among the variety of statistical and thermodynamic model approaches available, the Barker theory (generalized lattice theory of associated solutions)[226] has been used to calculate the thermodynamic properties of ternary systems containing rare-earth oxides, which has been extensively studied. It should be noted that, within the framework of the Barker theory,[226] it is possible to both optimize the thermodynamic description based on the available experimental data and calculate the thermodynamic quantities in solid solutions of multicomponent systems using the data on the corresponding binary systems.

Thus, the potential of KEMS as a unique method for studying the physicochemical properties of oxides at high temperatures is shown. Obviously, a wide range of model approaches are needed to process and further use the significant array of experimental data that can be obtained using this method. These models make it possible to calculate thermodynamic properties in multicomponent systems using data from corresponding binary systems and obtain sets of mutually consistent thermodynamic quantities for the systems under study.

An analysis of the current state of scientific knowledge indicates a need for further research into the high-temperature behavior of oxide systems containing rare-earth elements. Research by both experimental methods of high-temperature chemistry and within the framework of model approaches produces modern databases of thermodynamic data and model parameters, such as TAF-ID.[227] This

includes databases for the commonly used computational thermochemistry codes, such as FactSage or ThermoCalc, for predicting physicochemical properties and phase equilibria in oxide systems and materials.[197–200,222–225]

3.2.6 | Solution models and model parameters from KEMS

Solution behavior in metallic alloys and oxide systems is generally described using models. Although much progress has been made with first principles descriptions, models continue to be widely used for complex metallic alloys and oxide systems. These models are the primary feature of the CALPHAD method.[228] These models have been discussed in numerous books and review articles,[226,228,229] and an extensive discussion on them is outside the scope of this paper. We will summarize the key models and fitting of adjustable parameters for excess Gibbs energy of mixing with data obtained using the KEMS method. Generally, the Gibbs energy is described in terms of the constituent species, ideal Gibbs energy of mixing, and excess Gibbs energy of mixing.[228] For example, G^{φ}, the Gibbs energy of phase φ, is given as[230,231]

$$\begin{aligned} G^{\varphi} &= G_{\text{ref}} + G^{\text{ideal}}_{\text{mix}} + G^{xs}_{\text{mix}} \\ &= \sum_i x_i G_i^o + RT\sum_i x_i \ln x_i + \sum_{i=1}^{n}\sum_{j=i+1}^{n+1}\sum_{\upsilon=0}^{N} x_i x_j \left[L_{ij}^{\upsilon}\left(x_i - x_j\right)^{\upsilon}\right] \\ &+ \sum_{i=1}^{n-2}\sum_{j=i+1}^{n-1}\sum_{k=j+1}^{n} x_i x_j x_k \left(\nu_i L_i + \nu_j L_j + \nu_k L_k\right) \end{aligned} \tag{60}$$

Here x_i is the mole fraction of the constituent i, x_j is the mole fraction of the constituent j, and L_{ij}^{υ} is the interaction parameter where the superscript indicates the order and the subscripts indicate the two components of interest, namely $\nu_i = x_i/(x_i + x_j + x_k)$ and L_i is the ternary interaction parameter. The excess Gibbs energy is described using the Redlich–Kister polynomial,[232] which is often used in CALPHAD calculations due to its easy manipulation to obtain thermodynamic functions.[233] Without the excess term we, of course, have an ideal solution. Examining only the binary interaction terms, note the first term is simply the regular solution model and the second term is the subregular solution model. The ternary interaction term may be derived from several geometric arguments—here the Muggianu approach is shown.[230,231] Generally, each parameter is given a linear dependence on temperature[234–236]:

$$L_{ij}^{\upsilon} = A_{ij}^{\upsilon} + B_{ij}^{\upsilon} T \tag{61}$$

A_{ij}^{υ} and B_{ij}^{υ} are the adjustable parameters taken from experimental data, such as phase boundaries, enthalpy of mixing, and thermodynamic activity of each component. There are computer codes (e.g., PARROT for ThermoCalc[116] or OptiSage for FactSage[115]) for fitting these interaction parameters to experimental data. Accurate thermodynamic data are considered particularly desirable for setting the interaction parameters.

A wide variety of solution models have been applied to alloys, oxide systems, and other solutions. Perhaps the most common is the sublattice model, which would include two or more sublattices and equations like Equation (60) for each sublattice. Many models are based on the quasi-chemical or associates model, where the constituents in Equation (60) are not elements but rather hypothetical chemical compounds or associates. These may or may not be observable in the solution, but they allow for better modeling. There are many variations in the quasi-chemical model.[226,237,238] In summary, an appropriate model is selected to best describe the properties of a solution. These properties include structures, phase transformations, ordering, integral enthalpy of mixing, and thermodynamic activities of components. The parameters for a particular model are then fitted to the experimental data. KEMS can provide thermodynamic activities of components, melting enthalpies, and phase transformation temperatures, which are particularly valuable in the fitting. There are numerous examples of this in the literature. Bencze and colleagues[234–236] have determined binary and ternary interaction parameters from KEMS data for a number of alloys. Stolyarova and colleagues[5,189,193–196,200,201] have determined interaction parameters for a number of oxide systems using KEMS data.

4 | NOVEL APPLICATIONS OF KEMS

As discussed, the major application of KEMS has been thermodynamic measurements of both pure compounds and solutions. In this section, we discuss several novel applications of KEMS. We select a few applications that are particularly intriguing and offer promise for future studies. This list is by no means exhaustive, and there are many more novel applications of KEMS.

4.1 | Phase transformations

KEMS can be a valuable technique for determining phase changes, assuming, of course, an accurate temperature calibration. Gokcen et al.[239] have shown that the ratio of partial pressures of vapor species or ion intensities in the mass spectra of a vapor shows a discontinuity at the liquidus temperature. Consider a binary alloy with components A and B in the vapor mass spectra. The natural logarithm of the ratio of the ion intensities in the mass spectra of the vapor is given by

$$\ln(I_A/I_B) = \frac{\Delta_{\text{vap}}\bar{G}_B^i - \Delta_{\text{vap}}\bar{G}_A^i}{RT} + \tilde{C} \tag{62}$$

Here $\Delta_{\text{vap}}\bar{G}_A^i$ and $\Delta_{\text{vap}}\bar{G}_B^i$ are the partial molar Gibbs energies of vaporization of A and B from a solution i, respectively, and $\tilde{C}$ is a constant. A plot of $\ln(P_A/P_B)$ versus $1/T$—similar to the component activity ratio—is linear for a homogeneous solution (i.e., monophasic domain). For a liquid, when the temperature is decreased to that of liquidus, crystals of the solid will precipitate. The partial molar

quantities would change with composition of the system under study, and therefore, the plot is no longer linear. Such plots can yield quite accurate liquidus lines for a range of compositions. Nunoue and Kato[240] have used this technique with the Fe–Ge system, and Copland has used this technique with the Ni–Al–O[175] system, as shown in Figure 20.

Another interesting phase change study phenomena first reported using KEMS is that of Roberts and Searcy.[241] On cooling Ga_2S_3(s) between 1228 and 1203 K, they observed an *increase* in the partial pressure of Ga_2S. The vaporization of Ga_2S_3 is given by

$$Ga_{(2+2\varepsilon)}S_{(3-\varepsilon)}(s) = (1+\varepsilon)Ga_2S(g) + (1-\varepsilon)S_2(g) \quad (63)$$

The increase is explained by the appearance of a second phase of Ga_2S_3. As this second phase nucleates, the composition of the original Ga_2S_3 phase shifts to a higher Ga content and higher P(Ga_2S). The appearance of a second phase has been confirmed by Jones and Edwards.[242] This study shows the sensitivity of the Knudsen mass spectrometric technique to small phase changes.

Chatillon and Nuta[42] have pointed out that this phenomenon is related to the movement toward congruent vaporization in relation to continuous effusion that can modify the condensed phase composition throughout an experiment. As the specimen is cooled, it necessarily loses material to move toward a new point of congruency. This is analogous to the approach of an azeotrope in organic chemistry. Going through a two-phase region toward congruency, one of the phases loses material faster than the other. But the final P(Ga_2S)/P(S_2) is lower than the starting ratio. This indicates the importance of slow measurements and accounting for compositional differences during KEMS experiments.

4.2 | Ultrahigh-temperature materials

Since its inception, KEMS has been used for vapor phase analysis and determination of pressures where vaporization occurs with dissociation at very high temperatures. This is particularly useful now for materials that can withstand extreme temperatures encountered as reentry surfaces, heat engine components, and nuclear reactor components. These are termed "ultrahigh-temperature ceramics or composites" (UHTCs). Candidate UHTCs include oxides, borides, carbides, nitrides, and silicides.[243] The use of an electron beam or laser heating allows attainment of temperatures in excess of 2000 K. Stolyarova and colleagues[210,244] have investigated numerous binary and ternary systems of the form RE_2O_3-ZrO_2 (RE, rare earth), RE_2O_3-HfO_2-ZrO_2, or RE_2O_3-RE'_2O_3-ZrO_2 to temperatures near 3000 K.

Other ultrahigh-temperature materials, including borides, carbides, and nitrides, have been studied using KEMS. According to Fleischer,[243] there are more borides with melting points above 2273 K than any other group of inorganic compounds (i.e., carbides, nitrides, and oxides). Brewer and Haraldsen[245] point out that thermodynamic measurements of these compounds with conventional calorimetry are challenging due to insolubility in many solvents. However, KEMS offers the possibility of obtaining accurate thermodynamic data by measuring the partial pressures of the vapor species. Storms and Mueller[246] have studied the Mo–B system by measuring the boron partial pressures of species in compounds

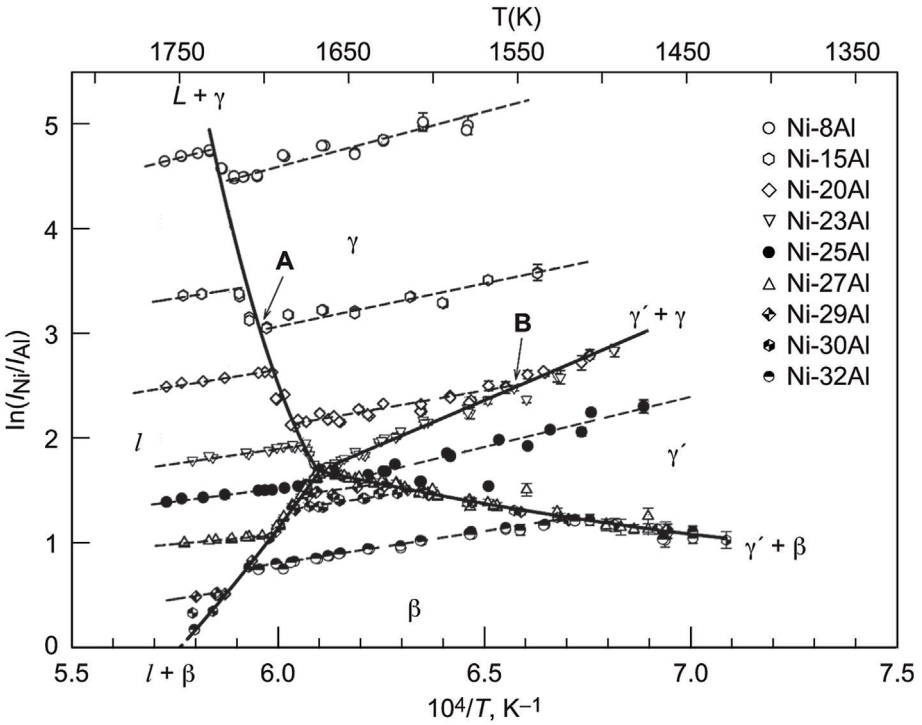

FIGURE 20 Phase changes in the Ni–Al–O system from ion current ratios. *Source*: Reprinted from Copland,[175] with permission from Elsevier.

spanning the range from the boron-rich to the molybdenum-rich sides of the corresponding phase diagram. A tungsten effusion cell saturated with B vapor was used, so the cell walls were tungsten boride. Figure 21 is a plot of measured activity of boron versus Mo–B ratio in the Mo–B system. Such an activity plot in conjunction with XRD data provides phase diagram information in this system. Other metal borides have also been studied using KEMS.[247,248]

Refractory carbides have some of the highest melting points measured, with HfC, TaC, NbC, and ZrC melting at temperatures >3773 K.[243] KEMS has been successfully applied to many refractory carbides, yielding information on the vapor species as well as partial molar quantities (e.g., component activities) of metal–carbon solid solutions. Considering pure carbon, an early KEMS study by Drowart et al.[249] illustrated the complex behavior of this basic material. There is a large body of KEMS work on metallic carbides, primarily in the 1960s and 1970s. Much of this work has been summarized in reviews.[250,251] The most common high-temperature carbide is SiC, which has been studied in a number of KEMS laboratories.[252–254] Rocabois et al.[253] observed the major species: Si(g), Si_2(g), Si_3(g), Si_2C(g), SiC_2(g), Si_2C_2(g), and Si_3C_2(g). They reported enthalpies of formation at 298.15 K for each of these vapor species. Behrens and Rinehart[254] and Davis et al.[255] have used vapor pressure measurements of the Si vapor species to determine the enthalpy of formation of SiC(s) at 298.15 K.

The transition metals and lanthanide metals also form useful refractory carbides. Kohl and Stearns[256] have examined TiC, ZrC, HfC, and ThC. They observed vapor species of the form MC(g), MC_2(g), and MC_4(g) at temperatures up to 3003 K. Using both the second and third law methods of thermodynamics, they reported standard enthalpies for the following reactions:

$$M(g) + 2C(s) = MC_2(g) \quad (64a)$$

$$M(g) + 4C(s) = MC_4(g) \quad (64b)$$

For the third thermodynamic law calculations, *gefs* are estimated from limited structural information and analogy to monoxide species, assuming the C_2^{-2} group bonding is similar to the O^{-2} group bonding. As noted earlier, improvements in *gef* estimates can now be made using modern computational methods. The study of Kohl and Stearns also shows that a component activity versus composition diagram in the system under study can be constructed from the two equilibria mentioned earlier. For the first reaction without excess carbon,

$$a_c^2 = \frac{1}{K_p}\frac{P_{MC_2}}{P_M} \approx \frac{1}{K_p}\frac{I_{MC_2^+}}{I_{M^+}} \quad (65)$$

This assumes the cross sections of the M and MC_2 vapor species are close. Then for the second reaction, without excess carbon,

$$a_c^2 = \frac{1}{K_p}\frac{P_{MC_4}}{P_{MC_2}} \approx \frac{1}{K_p}\frac{I_{MC_4^+}}{I_{MC_2^+}} \quad (66)$$

Gupta and Gingerich[257] have reported bond dissociation energies for vanadium, niobium, and molybdenum carbides. They used a single cell containing a small amount of Au for calibration. At lower temperatures, the Au^+/Au_2^+ ion current ratio was used to obtain a calibration constant, and then the measurements were taken in the 2600–3000 K temperature range. They used the second and third law methods of thermodynamics to report bond dissociation energies and atomization enthalpies. Gupta and Gingerich have also studied the vaporization of UC(s) and observed UC_n(g) ($n = 1$–6) vapor species, reporting enthalpies of formation at 298 K for all these species.[258] Yamawaki et al.[259] have reported on the thermodynamics of $ThC_{(1 \pm x)}$, and Koyama and Yamawaki[260] have presented thermodynamic data on the mixed carbide $(Th_{(1-y)}U_x)C$. In both studies dissolved oxygen plays an important role, and volatile metal oxides are observed. Nonetheless, activities of all components are reported in these systems. As shown, there is extensive research on refractory carbides using KEMS. Thus, KEMS is particularly well suited to carbides, as the generated vapor species can be analyzed, and the component activities can be measured.

Another important class of high-temperature materials is metal nitrides. These are typically less refractory than metal carbides, as they decompose into nitrogen and the metal and have somewhat lower melting points than carbides. Nonetheless, Si_3N_4, HfN, TaN, BN, ZrN, and TiN are all considered refractory materials. Again, KEMS is a valuable technique to study these materials, as it provides vapor composition and partial molar thermodynamic quantities. Rocabois et al.[261] have observed N_2(g), Si(g), Si_2(g), SiN(g), and Si_2N(g) above Si_3N_4(s). They used Knudsen cells with different orifice diameters to

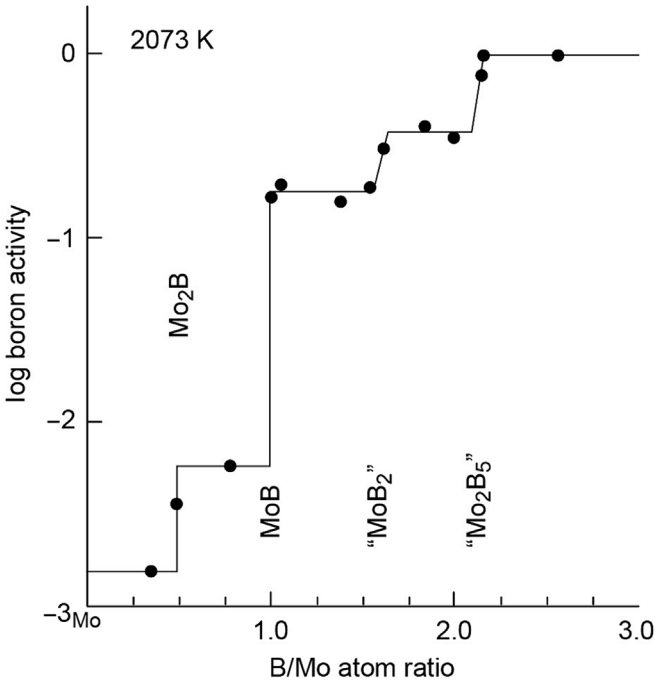

FIGURE 21 Activity as a function of composition for the Mo–B system. *Source*: Adapted from Storms and Mueller,[246] with permission from the American Chemical Society.

extract a very low vaporization coefficient of the vapor, which indicated a significant kinetic barrier to decomposition. Further, Rocabois et al. showed that compounds with very low vaporization coefficients,[261] such as Si_3N_4, do not yield adequate equilibrium data to determine enthalpies of formation. They recommend using calorimetric data instead.

Kohl and Stearns[262] have reported that HfN decomposes primarily into Hf(g) and N_2(g) and also HfN(g). Similar results have been reported for TiN,[263] ZrN,[264] UN,[265] and ThN.[266] Nitrides such as BN and AlN have kinetic barriers to vaporization.[42] Vaporization of Al or B limits the vaporization of N_2(g). In the case of TiN, N_2 loss changes the composition of the solid.[267]

Silicides have long been material candidates for very high-temperature use. $MoSi_2$ is commonly used as a high-temperature heating element in air, which suggests it may be useful as a structural material. Myers and coworkers have examined a number of transition metal silicides using KEMS.[268–270] They measured the activities of the metal and silicon, from the ion intensities of the metal, I_{M^+}, and ion current intensities of silicon, I_{Si^+}, in the mass spectra of the vapor, respectively. In some cases, where the Si vapor pressure and/or silicon activity is too low to measure, they add SiO_2 to the alloy and that generates a strong SiO^+ signal, which can be related to the activity of silicon.

4.3 | Measurement and fixing low oxygen potentials

In a KEMS experiment, the only source of oxygen is the residual oxygen in the vacuum system from outgassing of the construction materials. Further, oxygen-active refractory metals (W, Ta, Mo) tend to getter the oxygen. Therefore, one would expect a low oxygen potential inside the cell. Note that at high temperature and low oxygen potential, the O(g) pressure becomes higher than the O_2(g) pressure. Note that O(g) must be measured at ≤17 eV to avoid O^+ fragments in the mass spectra of the vapor from any O_2 in the ionizer. The direct measurement of oxygen is thus difficult, given the background that makes a shutterable oxygen signal less likely to be observed. However, many systems provide other species that allow indirectly an accurate determination of oxygen potential. These include the following:

$$WO_2(g) + ½O_2(g) = WO_3(g) \qquad P(O_2) = \left[\frac{P(WO_3)}{P(WO_2)K_p}\right]^2 \quad (67a)$$

$$MoO_2(g) + ½O_2(g) = MoO_3(g) \qquad P(O_2) = \left[\frac{P(MoO_3)}{P(MoO_2)K_p}\right]^2 \quad (67b)$$

$$Al_2O(g) = 2Al(g) + ½O_2(g) \qquad P(O_2) = \left[\frac{P(Al_2O)K_p}{[P(Al)]^2}\right]^2 \quad (67c)$$

Recently reaction (67c) has been used to determine the oxygen potential above Ti–Al–O alloys.[183] Such measurements are extremely important given the high solubility of oxygen in Ti and Ti–Al alloys. Stolyarova and Semenov[5] have shown that coupled oxide equilibria can be used to calculate the oxygen potential in an oxide system.

Related to the measurement of oxygen potential is the use of a zirconia cell to impose an oxygen potential in the cell. Detry et al. first demonstrated the use of an "electrochemical Knudsen cell" to set a sulfur potential.[20] More commonly, a zirconia Knudsen cell is converted into a zirconia oxygen pump, as shown in Figure 2E:

$$Pt, O_2(r) \,|\, ZrO_2 \,|\, Pt, O_2(cell) \qquad \ln\left(\frac{P(O_2)_r}{P(O_2)_{cell}}\right) = -\frac{4FE}{RT} \quad (68)$$

Here $P(O_2)_r$ is the oxygen reference pressure, $P(O_2)_{cell}$ is the desired oxygen pressure in the cell, F is the Faraday constant, and E is the applied voltage. There are many processes that occur at low oxygen potential, for example, processes at the oxide–metal interface during the high-temperature oxidation of metals. A Knudsen cell with a controlled/known oxygen potential offers an intriguing method to probe these processes.

4.4 | Geological applications

There are many questions in geochemistry and cosmochemistry that can be answered using KEMS. Minerals and rocks are often complex, multicomponent solutions, which lend themselves to KEMS studies. There are some KEMS studies on complex, multicomponent rocks and minerals in the literature.[118,271] For example, Rammensee and Fraser have used the ion current ratio method to examine the pseudo-binaries $NaAlSi_3O_8$-$KAlSi_3O_8$,[272] (Na–K)$AlSi_4O_{10}$, and (Na–K) $AlSi_5O_{12}$.[273]

The study on magmas has always been an important topic in geology. There are several studies on magmas such as those that may have existed on earth after the giant impact that formed the moon.[274–276] Understanding the solution behavior of lava is essential to these studies. Such behavior has been predicted from solution models.[275–277] In the study of Fegley et al.,[276] a magma consisting of 69 oxides was considered, and solution properties are extrapolated from a number of models. As discussed in the section on solution models, complex, multicomponent solutions can be modeled from binaries and ternary systems. KEMS can be useful in developing lower-order models for the study of geologically relevant higher-order systems and also providing a direct check for the solution properties of the actual higher-order systems.[278,279]

As noted, the high-resolution magnetic sector KEMS instruments can also be useful as isotope mass spectrometers. KEMS has proven useful in measuring the potassium component in K–Ar dating. In a study by Farley et al.[280] a tracer spike enriched in ^{39}Ar and ^{41}K was added to a lithium borate flux together with the mineral of known mass to be dated. A noble gas mass spectrometer was used to measure $^{40}Ar^*/^{39}Ar$, and a KEMS system was used to measure $^{39}K/^{41}K$. These two quantities are combined to calculate the age of

the sample. This method [280] was demonstrated on a basalt sample, whose age was known from other methods.

Another intriguing application of KEMS is the study of simulated exoplanet atmospheres.[281] Hot, rocky extrasolar planets such as CoRoT-7b, Kepler-10b, and 55 CNC e are close enough to their host suns that they may have surface temperatures from 2400 to 3000 K. Further, they are tidally locked, meaning one side always faces the host star.[282] This leads to a planet surface of magma oceans and an atmosphere of the corresponding high-temperature vapors above those oceans. Thus, the Knudsen cell may act as a small simulation of the surface conditions of a hot, rocky exoplanet. In the study by Costa et al.,[281] olivine and its vapor were examined using KEMS. Olivine was selected as a test material, because it is the principal constituent of the earth's mantle and may be a reasonable approximation to an exoplanet surface composition. The study of exoplanets is one of the most exciting areas in modern astrophysics, and KEMS can play an important role in this.

4.5 | Nuclear applications

Another growth area for KEMS is its application to the nuclear field. As noted in the ultrahigh-temperature materials section, KEMS has provided excellent data on nuclear materials such as UO_2, MOX (mixed oxide, plutonium-blended uranium fuel), UC, and UN. Earlier reviews[190,283] have presented this work in detail. A recent reference work[284] on fuel chemistry reports further information on KEMS studies in this field.

Recent KEMS studies in the nuclear field are heavily influenced by events such as climate change,[285] energy supply issues,[286] and decommissioned irradiation facilities for medical isotope production.[287] Advanced reactors such as small modular reactors, reactors developed in GEN IV, and alternative research reactors are drawing attention in this context. There are many ongoing advanced reactor development efforts, funded by both the public and private sectors.[288] Some of these new reactor concepts need investigations on new fuels. KEMS is the key technique for such studies. Nuclear fuel, in its environment, under normal or accidental conditions, is a very complex system for which the thermodynamic properties need to be assessed before implementation in a commercial or research reactor. KEMS has long been a key technique used to investigate nuclear fuel behavior. KEMS investigations in this field provide unique key data on partial vapor pressures, component activities, and nonideal solution behavior (e.g., the behavior of fission products in oxide fuels). These data are all essential for the safety and licensing of a nuclear fuel. Nuclear waste is also an important domain in which KEMS studies play a key role.

4.5.1 | Molten salt fuels

Molten salt reactors (MSR) are the only reactors using liquid as fuel. Fissile material and fission product are dissolved in the liquid, which is also used as a coolant. A fuel treatment unit can be included in the liquid loop to reprocess the fuel during irradiation. One reactor of this type is the well-known Oak Ridge molten fluoride reactor built in the 1960s. Two kinds of fuels are considered for MSRs: chlorides and fluorides. Both have different chemical and neutronic characteristics. Depending on the function of the fuel and its composition, different kinds of reactors can be built. With a thermal neutron spectrum, reactors can burn ^{235}U, which represents only a fraction of the uranium extracted, or breed ^{233}U from natural thorium, ^{232}Th, which is more abundant in the earth's crust but requires significantly more expensive extraction methods. Reactors with a fast neutron spectrum can burn plutonium and other transuranium actinides, which thus reduce nuclear waste and breed ^{238}U and ^{232}Th to form ^{239}Pu and ^{233}U, respectively. These can then be used as fuel. The salts are also used for pyrometallurgical processes in nuclear industry.

Many studies on these salts have been conducted using KEMS. Some examples follow. Tosolin et al.[289,290] have reported thermodynamic data from KEMS on the LiF-ThF_4-UF_4 and LiF-ThF_4-UF_4-PuF_3 systems. Vozárová et al.[291] published KEMS-derived thermodynamic data for the CsF-ThF_4 system. Capelli et al.[292] reported data on $Li_xTh_{(1-x)}F_{(4-3x)}$, and Mishra[293] and McMurray et al.[294] presented data on FLiNaK. On the chloride side, Trinadh et al.[108] performed measurements on LiCl-KCl-UCl_3. Beneš[295] have measured the vaporization behavior of Cs and I from fluoride melts. Taira[296] have studied the behavior of simulated fission products in solution for different fuel compositions. Hania[297] has studied irradiated molten salt fuels targeted for KEMS measurements. There is limited published information on molten chloride fuels. KEMS investigations related the development of molten chloride fast reactors as ongoing.

4.5.2 | Liquid metal coolants and metallic fuels

Liquid lead–bismuth eutectic is another important material for an advanced nuclear reactor. It is used as a primary coolant in lead-cooled fast reactors and as a fuel and coolant in accelerator-driven systems. Luongo et al.[298] have studied lead iodide decomposition, which is relevant for this fuel.

Metallic fuels, such as dispersion fuels, are used in research reactors. Trinadh et al. have published KEMS studies of the U–Al system.[299,300] The U–Pu–Zr system is a potential driver fuel for fast breeder reactors. Two compositions in this ternary have also been investigated by Trinadh et al.[301] Recent KEMS studies on the Gd–Al system focus on the potential of separating actinides from the lanthanides.[302]

4.5.3 | Oxide fuels

Oxides fuels are the most used in current and advanced reactors. A large amount of literature is available and can be found in earlier reviews, including data on highly radiotoxic oxides.[77,80,303] Most

recently, in the field of fast reactors for transmutation, Smith et al. have published a thermodynamic study of the Np–O system, which included KEMS measurements and thermodynamic modeling.[304] Refractory ceramic oxides are also important for other nuclear issues such as nuclear waste immobilization, fuel cladding, and severe accident containment. KEMS studies on the following relevant systems have recently been reported: Sm_2O_3-ZrO_2,[67,305] UO_2-ZrO_2,[306] and Sm_2O_3-ZrO_2-HfO_2.[244,307]

4.5.4 | Interacting materials, coupled diffusion/desorption, and vaporization measurements

Understanding the interaction of materials in a reactor is another area in which KEMS can play a crucial role. Regarding the interaction of fission products with their environment during severe accidents, Stolyarova and colleagues have published thermodynamic studies on the Cs_2O-B_2O_3[211] and Cs_2O-MoO_3[212] systems. Nakajima published a KEMS study on $CsBO_2$.[308] As noted earlier, the study on the thermal decomposition of lead iodide[298] is important in the interaction of fission products and lead-cooled reactors.

Structural materials used in the complete fuel cycle present high mechanical, thermal, and chemical constraints. A recent KEMS study reports thermodynamic measurements in structural nickel-base alloys and steel used by the fuel enrichment process.[181]

After the Fukushima accident in Japan, accident-tolerant fuels drew attention. Braun et al. have recently reported KEMS studies on the chemical compatibility of UO_2 fuel and an SiC coating.[309]

The behavior of fission products in a reactor has been discussed briefly for MSRs. For other systems, Trinadh et al. and Manikandan et al. have published studies on the Sn–Te–O and U–Sn systems, which are important for fuel safety, accident conditions, and pyro reprocessing.[310,311] Stolyarova et al.[312] have recently reported thermodynamic data and vaporization behavior of Cs, Sr, and Ba compounds relevant to nuclear safety.

Fission products or helium release behavior studies using KEMS are important to mention here. These studies address safety-relevant aspects such as radioisotope release during accidents but also fuel properties during normal operation. They combine the measurement of vaporization at equilibrium with the measurement of the release of volatile elements (or compounds) present in the material studied. This reveals interesting information on the temperature-driven diffusion processes of those volatile elements and their consequences in the material like precipitation, bubble formation, release from the matrix, the role of grain boundaries, diffusion enthalpies, and solubility. Such data are needed to understand the fuel behavior in normal and accidental operations as well as in storage conditions. Fission product release behavior from nuclear fuel has been extensively studied using KEMS. A recent example reports the comparative fission product release behavior of a homogeneous and a heterogeneous high-burn-up MOX nuclear fuel.[313] Other examples demonstrate the measurement using KEMS of helium solubility in stoichiometric and hyper-stoichiometric UO_2[314] or in La-doped UO_2 as a surrogate of hypo-stoichiometric UO_2.[315] In the later study, the spent fuel storage/disposal aspect is addressed. Diffusion and release properties of radiogenic helium need to be assessed for the prediction of material long-term behavior (spent fuel, radioisotopic thermal generator, actinide-bearing fuels). A most recent KEMS study of Luzzi et al.[316] reports measured helium release in the investigation of the solubility and release behavior of helium in a nuclear fuel.

4.5.5 | Sorption/desorption of fission products from graphite

Understanding the sorption/desorption of fission products from fuel element matrix graphite is very important in the event of an accident. Several recent publications on desorption isotherms have been obtained using a KEMS system. Hilpert et al. have studied the sorption of Sr and Cs on graphitic materials[317,318] using KEMS. Seelig et al.[129] and Walton et al.[319] have used KEMS to study sorption of Ag on graphitic materials. Other methods can, of course, be used to study sorption, but KEMS has proven to be very versatile for these applications given its high sensitivity. The method described in the KEMS studies[129,317–319] involves doping nuclear graphite with a nonradioactive isotope of the particular fission product of interest. A series of fission product loadings are examined using KEMS to derive partial pressures of vapor species as a function of temperature. The loading-dependent Sr enthalpy of vaporization,[317] as shown in Figure 22, indicates Sr is strongly chemisorbed on graphite. The loading dependence of partial pressures of the vapor species can be used to derive a sorption isotherm. Walton et al.[319] have examined Langmuir, IAEA-Freundlich, and IAEA-isotherm models for Ag desorption from NBG-17 graphite powders. For this particular case, Langmuir and IAEA-isotherm models gave the best fit.

4.6 | Low-volatility organics and organometallics

The lack of vapor pressure data for multifunctional condensable organic compounds formed from gas phase volatile organic carbon oxidation has led to the development of a novel KEMS device capable of performing such measurements. The design was adapted from high-temperature alloy measurements to study low-volatile organics. The challenge of such measurements is to fulfill the Knudsen conditions and to ensure equilibrium conditions in the temperature range of ~300 K. Most of the measurements comprise only a temperature range from 30 K. For this type of study, a special Knudsen cell was fabricated with a knife-edged orifice of 200-μm diameter. The cell was heated by a coaxially mounted flexible polyimide heating element. The molecular beam effusing out of the Knudsen cell was ionized by a cross-beam electron gun. The ions are separated in a quadrupole mass filter and detected by a classical secondary electron multiplier or a Faraday cup. The system consists of two vacuum chambers, one for housing the sample and Knudsen cell

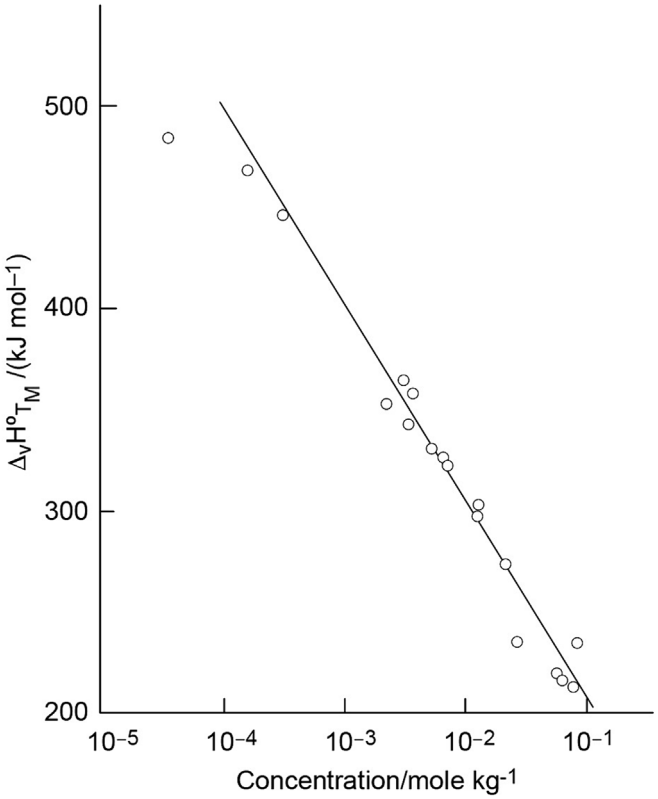

FIGURE 22 Enthalpy of vaporization for Sr from nuclear-grade graphite. *Source*: Reprinted from Hilpert et al.,[318] with permission from Wiley-VCH, GmbH.

and the other for the measurement systems. They are separated from each other by a vacuum-tight gate valve.

A further challenge for the determination of vapor pressures for organic systems is to find a suitable calibration specimen of which pressure data are well established in the literature. The following compounds have been selected: benzophenone, ferrocene, or diphenylmethane. The proof of the development of a simple KEMS system was given in 2009 by measuring the vapor pressures of dicarboxylic acid.[320] The device has been built at the University of Manchester (UK) and has since been used to determine vapor pressure data for a number of organic systems. Kudin et al. have studied the thermochemistry of 5,10,15,20-tetraphenylporphyrin.[321] The extension of KEMS to low temperatures opens up the possibility of novel ionization methods to limit fragmentation. Booth and colleagues[322] described the use of a lithium ion attachment technique to form ions without fragmentation in mass spectra of a vapor over the compounds studied.

KEMS studies on organometallic compounds have been published at SIMaP.[21,323,324] As these compounds show ignition under atmospheric pressure, the cell is fitted with a valve controlled from outside. The sample is loaded and held in a glove box before transfer to the mass spectrometer. The cell (see Figure 2F) is then opened under vacuum when starting an experiment. Thermodynamic measurements of organometallic vapor pressures require a coupling of a restricted collimation device, a liquid-nitrogen-cooled ionization box, and a "free" shutter blade to distinguish the signal from secondary reflections in the vacuum chamber. These were described in previous sections of this review. The Knudsen cell furnace has been designed as a double envelope with a circulating liquid and temperature range of 233–473 K. Saturated pressure of the PDMAT (pentakis (dimethylamino) tantalum)—usually believed to be the same molecule as the solid or liquid compound as for organic compounds—has been determined to correspond to at least two main molecules from Ta^{4+} to Ta^{5+}. Then the Knudsen is fitted with an upper cell to study high-temperature cracking of these molecules useful for the understanding of chemical vapor deposition or atomic layer deposition processes.

4.7 | Lithium ion battery applications

KEMS has recently been used more for the determination of low temperature and room temperature thermodynamic data. Such an approach is used in the determination of data for various lithiation states of lithium ion battery electrode materials. One example for that is the development of lighter and anode materials that also show less volume change on lithiation. Henriques and coworkers have determined thermodynamic data in the ternary alloy system Cu–Li–Sn using KEMS for the solid, solid–liquid, and liquid regions. Thermodynamic activities of components, enthalpies, and entropies of mixing were measured.[325,326] This work was directly supported using CALPHAD-type modeling.[236]

5 | SUMMARY AND CONCLUSIONS

KEMS has long been a central tool in physical chemistry, and it has many applications in related fields. There are many excellent reviews on the basic concepts of this technique.[1-11,18,87] In this review, we focus on the current and future status of the field. The first part of the review covers instrumentation and progress in methodology. Modern simulation methods of both the neutral beam and the ionization processes can lead to many design improvements for better sensitivity, resolution, and background/noise rejection. Newer heating systems and temperature measurement devices offer better control and measurement of temperature to higher (and lower) limits. Data acquisition systems allow computer control of nearly all aspects of an experiment. Given the nonroutine nature of a KEMS experiment, it may not be possible to fully automate an experiment; nonetheless, data acquisition systems make measurements easier and more precise.

The second part of this review focuses on actual measurements and applications. We focus on current topics that show promise for the future, although the areas covered are by no means exhaustive. KEMS has always been a prime tool for analysis of vapor composition and then measurement of vapor pressures as a function of temperature and thus obtaining thermodynamic data of pure compounds and gaseous species. A key area is now coupling these

measurements to precision quantum chemistry calculations. These calculations can be used to generate high-fidelity *gefs*. It has been shown that in many cases, DFT/B3LYP is sufficient to generate these *gefs*. KEMS measurements of enthalpies of formation and dissociation can also be compared directly to ab intio calculations, giving them added reliability. KEMS is also well suited to the study of solutions. Although first principles can describe some solutions, model-based approaches work well for complex, multicomponent solutions. We discuss the solution thermodynamic parameters that can be fitted to model parameters. The parameters from relatively simple binary and ternary solutions can be combined to develop solution models for complex multicomponent solutions.

Finally, we select a few important applications of KEMS and likely growth areas for KEMS. These include measurement of phase transformations, measurements/control of systems with low oxygen potentials, studies on ultrahigh-temperature materials, applications to geological systems, applications to nuclear systems, and applications to organic and organometallic chemistry. As noted, this list is not exhaustive, and the number of applications of this valuable method can and should continue to grow.

AUTHOR CONTRIBUTIONS

Nathan S. Jacobson: conceptualization; project administration; writing—introduction, portions of the instrumentation section, measurement section, and sections on phase transformations, ultrahigh-temperature materials, measurement and fixing of low oxygen potentials, and geological applications; figures; and overall editing and checking. **Jean-Yves Colle:** writing—section on KEMS in gloveboxes, portions of the data acquisition section, nuclear applications section; figures; and overall editing and checking. **Valentina Stolyarova**: writing—section on measurements of oxide thermodynamics; figures; and overall editing and checking. **Torsten Markus**: writing—portions of the data acquisition section, section on lithium ion battery applications; figures; and overall editing and checking. **Ioana Nuta:** writing—portions of the instrumentation section and section on low-volatility organics and organometallics; figures; and extensive editing and checking.

ACKNOWLEDGMENTS

The authors thank the many individuals who have contributed to this review. Nathan S. Jacobson thanks his colleagues at NASA for helpful discussion—Drs. Benjamin Kowalski, Rebekah Webster, and particularly Evan Copland (now at the University of Newcastle, Australia). The authors are grateful to Prof. John H. Beynon, founder and first editor of *RCM*, who promoted KEMS as an important subdiscipline of general mass spectrometry. They thank Dr. Christian Chatillon for his many suggestions for this review. The authors have been fortunate to learn from the pioneers and leaders in KEMS, which include Prof. Dr. Klaus Hilpert, Prof. Alan Searcy, Dr. Donald Hildenbrand, Prof. Paul Gilles, Dr. John Hastie, Dr. Christian Chatillon, Prof. Jean Drowart, Prof. Lev Gorokhov, and Prof. G. A. Semenov. The authors dedicate this review to them.

DATA AVAILABILITY STATEMENT

Data sharing not applicable to this article as no datasets were generated or analysed during the current study.

ORCID

Nathan S. Jacobson https://orcid.org/0000-0002-9177-4129

REFERENCES

1. Inghram M, Drowart J. Mass spectrometry applied to high temperature chemistry. *High Temp Technol*. 1960;219-240.
2. Drowart J, Goldfinger P. Investigation of inorganic systems at high temperature by mass spectrometry. *Angew Chem Int Ed*. 1967;6(7):581-648. doi:10.1002/anie.196705811
3. Cater ED. The effusion method at age 69: current state of the art. In: Hastie JW, ed. *Characterization of High Temperature Vapors and Gases*. U. S. Government Printing Office; 1979:3-38.
4. Grimley RT. Mass spectrometry. In: Margrave JL, ed. *The Characterization of High Temperature Vapors*. Wiley; 1967:195-243.
5. Stolyarova VL, Semenov GA. In: Beynon JH, ed. *Mass Spectrometric Study of the Vaporization of Oxide Systems*. Wiley; 1994.
6. Kato E. Thermodynamic studies of metallurgical systems by mass spectrometry. *J Mass Spectrom Soc Japan*. 1993;41(6):297-316. doi:10.5702/massspec.41.297
7. Hilpert K. High-temperature mass-spectrometry in materials research. *Rapid Commun Mass Spectrom*. 1991;5(4):175-187. doi:10.1002/rcm.1290050408
8. Gorokov L, Semenov G. Mass spectrometric studies in high-temperature chemistry. *Adv Mass Spectrometry*. 1971;5:349.
9. Gorokhov L. High-temperature mass spectrometry. *Adv Mass Spectrom*. 1989;11B:1064-1077.
10. Rose ME, Plante E, Haltle J. High-temperature mass spectrometric studies of inorganic systems. In: *Mass Spectrometry*. Royal Society of Chemistry; 1989:357-378. doi:10.1039/9781847556677-00357
11. Johnston G. High-temperature vaporization studies using Knudsen cell mass spectrometry—a review. *J Aust Inst Metals*. 1974;19(2):106-115.
12. Knudsen M. Experimental determination of the vapor pressure of mercury at 0° and at higher temperatures. *Ann Phys*. 1909;29(6):179-193. doi:10.1002/andp.19093340614
13. Santeler DJ. New concepts in molecular gas flow. *J Vac sic Technol A*. 1986;4(3):338-343. doi:10.1116/1.573923
14. Jacobson NS. Silica activity measurements in the Y_2O_3–SiO_2 system and applications to modeling of coating volatility. *J am Ceram Soc*. 2014;97(6):1959-1965. doi:10.1111/jace.12974
15. Bauschlicher CW Jr, Kowalski BA, Jacobson NS. Quantum chemical and experimental thermodynamic studies of HfO(g). *J Chem Phys*. 2022;157(15):154302. doi:10.1063/5.0120504
16. Rocabois P, Chatillon C, Bernard C. Thermodynamics of the Si-C system I. mass spectrometry studies of the condensed phases at high temperature. *High Temp-High Press*. 1995;27(1):3-23. doi:10.1068/htrt35
17. Meschi DJ, Chupka WA, Berkowitz J. Heterogeneous reactions studied by mass spectrometry. I. Reaction of B_2O_3(s) with H_2O(g). *J Chem Phys*. 1960;33(2):530-533. doi:10.1063/1.1731179
18. Copland EH, Jacobson NS. *Measuring Thermodynamic Properties of Metals and Alloys with Knudsen Effusion Mass Spectrometry*. NASA/TP--2010–216795
19. Chatillon C, Malheiros L-F, Rocabois P, Jeymond M. High-temperature mass spectrometry with the Knudsen cell: II. Technical constraints in the multiple-cell method for activity determinations. *High Temp-High Press*. 2002;34(2):213-233. doi:10.1068/htjr021

20. Detry D, Drowart J, Goldfing P, Keller H, Rickert H. Zur Thermodynamik Von Schwefeldampf—Massenspektrometrische Untersuchungen Mit Der Elektrochemischen Knudsen-Zelle. *Z Phys Chem Neue Fol*. 1967;55(5–6):314-319. doi:10.1524/zpch.1967.55.5_6.314
21. Violet P, Nuta I, Artaud L, Collas H, Blanquet E, Chatillon C. A special reactor coupled with a high-temperature mass spectrometer for the investigation of the vaporization and cracking of organometallic compounds. *Rapid Commun Mass Spectrom*. 2009;23(6):793-800. doi:10.1002/rcm.3942
22. Colle J-Y, Capone F. Very high temperature laser heated furnace for Knudsen cell mass spectrometry. *Rev Sci Instrum*. 2008;79(5):055105. doi:10.1063/1.2918135
23. Shilov A. Vaporizers for KEMS: measurement errors depending on their design. *ECS Transactions*. 2013;46(1):187-190. doi:10.1149/04601.0187ecst
24. Cater ED. Vapor pressure measurements A. measurement of the gross equilibrium vaporization rate (Knudsen Methods). In: Rapp RA, ed. *Physicochemical Methods in Metals Research. Techniques of Metals Research. IV*. John Wiley & Sons, Inc.; 1970:21-94.
25. Solorio-Leyva JC, Suárez-Romero JG, Cortés-Reynoso JG, Hurtado-Ramos JB, Tepichín-Rodríguez E. Corrections of size-of-source effect and distance effect in radiometric measurements of radiance. *Appl Optics*. 2005;44(13):2511-2518. doi:10.1364/AO.44.002511
26. Ackermann RJ, Garg SP, Rauh EJ. High-temperature phase diagram for the system Zr-O. *J am Ceram Soc*. 1977;60(7–8):341-345. doi:10.1111/j.1151-2916.1977.tb15557.x
27. Bhatt Y, Venkataramani R, Garg S. Measurements of eutectic temperatures in the metal-rich regions of several MC systems. *J Less-Common Met*. 1987;132(2):21-24. doi:10.1016/0022-5088(87)90590-X
28. Balakrishnan S, Ananthasivan K, Kumar KH. Measurement of the solidus and liquidus in the U-Zr system by the spot-technique. *J Alloys Compd*. 2016;689:751-758. doi:10.1016/j.jallcom.2016.07.252
29. Preston-Thomas H. International temperature scale of 1990 (ITS-90). *Metrologia*. 1990;27(1):3-10. doi:10.1088/0026-1394/27/1/002
30. Yamada Y, Sakate H, Sakuma F, Ono A. High-temperature fixed points in the range 1150 C to 2500 C using metal-carbon eutectics. *Metrologia*. 2001;38(3):213-219. doi:10.1088/0026-1394/38/3/3
31. Hildenbrand D. Attainment of chemical equilibrium in effusive beam sources of the heterogeneous reaction type. In: Hastie J, ed. *Characterization of High Temperature Vapors and Gases*. U. S. Government Printing Office; 1979:171-180.
32. Whitman CI. On the measurement of vapor pressures by effusion. *J Chem Phys*. 1952;20(1):161-164. doi:10.1063/1.1700161
33. Motzfeldt K. The thermal decomposition of sodium carbonate by the effusion method. *J Phys Chem*. 1955;59(2):139-147. doi:10.1021/j150524a011
34. Paule RC, Margrave JL. Free-evaporation and effusion techniques. In: Margrave JL, ed. *The Characterization of High-Temperature Vapors*. John Wiley & Sons; 1967.
35. Kulkarni A, Worrell W. High-temperature thermodynamic properties of the chromium carbides determined using the torsion-effusion technique. *Metall Trans A*. 1972;3(9):2363-2370. doi:10.1007/BF02647039
36. Rocabois P, Chatillon C, Bernard C. Vapor-pressure and evaporation coefficient of SiO (amorphous) and SiO_2(s)+Si(s) mixtures by the multiple Knudsen cell mass-spectrometric method. *Rev Int Hautes Temp*. 1992;28(2):37-48.
37. WC DM. *The Problem of Knudsen Flow. Part I. General Theory*. Oak Ridge Gaseous Diffusion Plant (K-25); 1956.
38. DeMarcus WC, Hopper E. Knudsen flow through a circular capillary. *J Chem Phys*. 1955;23(7):1344. doi:10.1063/1.1742272
39. Davis DH. Monte Carlo calculation of molecular flow rates through a cylindrical elbow and pipes of other shapes. *J Appl Phys*. 1960;31(7):1169-1176. doi:10.1063/1.1735797
40. Rosenblatt GM. Evaporation from Solids. In: Hannay NB, ed. *Treatise on Solid State Chemistry*. Springer; US, 1976:165-240. doi:10.1007/978-1-4613-4313-4_3
41. Rosenblatt GM. Effect of restrictions to molecular flow upon measurements of vaporization rate and vapor pressure. *J Phys Chem*. 1967;71(5):1327-1333. doi:10.1021/j100864a022
42. Chatillon C, Nuta I. Mass spectrometric studies of non-equilibrium vaporizations in Knudsen cells: a way to the determination of the nature of kinetic processes. *ECS Transactions*. 2013;46(1):1-22. doi:10.1149/04601.0001ecst
43. Jacobson N, Lee K, Fox D. Reactions of silicon carbide and silicon (IV) oxide at elevated temperatures. *J am Ceram Soc*. 1992;75(6):1603-1611. doi:10.1111/j.1151-2916.1992.tb04232.x
44. Heyrman M, Chatillon C. Evaporation/condensation coefficients as determined by the multiple Knudsen effusion cell method. *J Phys Chem Solid*. 2005;66(2–4):494-497. doi:10.1016/j.jpcs.2004.06.025
45. Rosenblatt GM. Interpretation of Knudsen vapor-pressure measurements on porous solids. *J Electrochem Soc*. 1963;110(6):563. doi:10.1149/1.2425815
46. Golden DM, Spokes GN, Benson SW. Very low-pressure pyrolysis (VLPP); a versatile kinetic tool. *Angew Chem Int Ed*. 1973;12(7):534-546. doi:10.1002/anie.197305341
47. Abbasi M, Evans J, Abramson I. Diffusion of gases in porous solids: Monte Carlo simulations in the Knudsen and ordinary diffusion regimes. *AIChE J*. 1983;29(4):617-624. doi:10.1002/aic.690290415
48. Gorokhov L, Milushin M, Emelyanov A. Knudsen effusion mass spectrometric determination of metal hydroxide stabilities. In: Hastie JW, ed. *Materials Chemistry at High Temperatures*. Vol.1. Humana Press; 1990:395-403. doi:10.1007/978-1-4612-0481-7_29
49. Heyrman M, Chatillon C, Collas H, Chemin JL. Improvements and new capabilities for the multiple Knudsen cell device used in high-temperature mass spectrometry. *Rapid Commun Mass Spectrom*. 2004;18(2):163-174. doi:10.1002/rcm.1298
50. Chatillon C, Senillou C, Allibert M, Pattoret A. High-temperature thermodynamical studies by a mass spectrometry device for measurements using multiple effusion cells. *Rev Sci Instrum*. 1976;47(3):334-340. doi:10.1063/1.1134618
51. Heyrman M, Chatillon C. Methodological improvements in the multiple Knudsen cell mass spectrometry. *J Phys Chem Solid*. 2005;66(2–4):376-378. doi:10.1016/j.jpcs.2004.06.076
52. Johnston G, Burley N. Quad-cell mass spectrometry: vaporization studies up to 2300 K using a rotatable, multiple Knudsen Cell ('QUAD-CELL'). In: Czairliyan A, ed. *Proceedings of the Seventh Symposium on Thermophysical Properties*. American Society of Mechanical Engineers, New York; 1977:222-230.
53. Hilpert K, Ruthardt K. Determination of the dissociation-energy of the Cr_2 molecule. *Ber Bunsen Phys Chem*. 1987;91(7):724-731. doi:10.1002/bbpc.19870910707
54. Wahlbeck P. Effusion. VII. The failure of isotropy of a gas in an effusion cell and the transition region. *J Chem Phys*. 1971;55(4):1709-1715. doi:10.1063/1.1676300
55. Demarcus WC. *The Problem of Knudsen Flow. Part II. Solution of Integral Equation with Probability Kernels*. Oak Ridge Gaseous Diffusion Plant (K-25); 1956.
56. Grimley RT, Wagner LC, Castle PM. Angular-distributions of molecular species effusing from near-ideal orifices. *J Phys Chem*. 1975;79(4):302-308. doi:10.1021/j100571a003
57. Ward JW, Fraser MV. Some of the parameters affecting Knudsen effusion. IV Monte Carlo calculations of effusion probabilities and flux gradients for Knudsen cells. *J Chem Phys*. 1968;49(9):3743-3750. doi:10.1063/1.1670674

58. Ward JW, Fraser MV. Study of some of the parameters affecting Knudsen effusion. VI. Monte Carlo analyses of channel orifices. *J Chem Phys*. 1969;50(4):1877-1882. doi:10.1063/1.1671283
59. Ward JW, Bivins RL, Fraser MV. Monte-Carlo simulation of specular and surface diffusional perturbations to flow from Knudsen cells. *J Vac Sci Technol A*. 1970;7(1):206-210. doi:10.1116/1.1315797
60. Ward JW, Bivins RL, Fraser MV. Monte-Carlo analysis of behavior of divergent conical effusion orifices. *J Vac Sci Technol A*. 1972;9(3):1056-1061. doi:10.1116/1.1316990
61. Radke MJ, Jacobson NS, Copland EH. Monte Carlo simulation of a Knudsen effusion mass spectrometer sampling system. *Rapid Commun Mass Spectrom*. 2017;31(12):1041-1046. doi:10.1002/rcm.7873
62. Margrave JL. *The Characterization of High-Temperature Vapors*. Wiley; 1967.
63. Froment A, Chatillon C, Colin M. Determination of B and C activities in the non-stoichiometric $B_{4-x}C$ compound by the multiple Knudsen-cell mass spectrometric method. *Rev Int Hautes Temp*. 1991;27(4):141-158.
64. Morland P, Chatillon C, Rocabois P. High-temperature mass spectrometry using the Knudsen effusion cell I—optimization of sampling constraints on the molecular beam. *High Temp Mat Sci*. 1997;37(3):167-187.
65. Nuta I, Chatillon C. Knudsen cell mass spectrometry using restricted molecular beam collimation. I. Optimization of the beam from the vaporizing surface. *Rapid Commun Mass Spectrom*. 2015;29(1):10-18. doi:10.1002/rcm.7071
66. Benigni P, Berche A, Mikaelian G, Rogez J. Transformation of a double focusing BE mass spectrometer for multiple-cell Knudsen effusion–part I: scientific concepts. *ECS Transactions*. 2013;46(1):127-141. doi:10.1149/04601.0127ecst
67. Baïchi M, Chatillon C, Guéneau C, Chatain S. Mass spectrometric study of UO_2–ZrO_2 pseudo-binary system. *J Nucl Mater*. 2001;294(1–2):84-87. doi:10.1016/S0022-3115(01)00477-9
68. Walsh JW. Radiation from a perfectly diffusing circular disc (Part I). *P Phys Soc Lond*. 1919;32(1):59-71. doi:10.1088/1478-7814/32/1/308
69. Walsh JW. *Photometry*. Constable & Co. Ltd; 1958.
70. Nuta I, Chatillon C. Erratum to: Knudsen cell mass spectrometry using restricted molecular beam collimation. I. Optimization of the beam from the vaporizing surface. *Rapid Commun Mass Spectrom*. 2017;31(12):1077-1078. doi:10.1002/rcm.7870
71. Chatillon C, Nuta I. Spurious molecular beams in Knudsen effusion mass spectrometry. *CAL*. 2019;65:8-15. doi:10.1016/j.calphad.2019.01.009
72. Trinadh V, Manikandan P, Bera S, et al. Vaporisation studies over Sn-Te-O system. In: *Proceedings of the Thirty First ISMAS Symposium on Mass Spectrometry*; 2017.
73. Murad E. Mass spectrometric techniques. In: *Spectrometric Techniques*. Academic Press; 1985:181-251. doi:10.1016/B978-0-12-710404-1.50009-7
74. Dunaev A, Kudin L, Motalov V, Ivanov D, Butman M, Krämer K. Mass spectrometric study of molecular and ionic sublimation of lanthanum triiodide. *Thermochim Acta*. 2015;622:82-87. doi:10.1016/j.tca.2015.09.008
75. Motalov V, Dunaev A, Kudin L, Butman M, Krämer K. Molecular and ionic sublimation of neodymium, dysprosium, holmium, and erbium triiodides and thermochemistry of molecules and ions. *Int J Mass Spectrom*. 2020;457:116431. doi:10.1016/j.ijms.2020.116431
76. Klemperer O, Barnett ME. *Electron Optics*. Cambridge University Press; 1971.
77. Gotcu-Freis P, Colle J-Y, Hiernaut J-P, Konings RJM. The vaporisation behaviour of americium dioxide by use of mass spectrometry. *J Nucl Mater*. 2011;409(3):194-198. doi:10.1016/j.jnucmat.2010.12.024
78. Ivanov D, Bourdon B. Numerical simulations of magnetic electron-impact ion source. *Int J Mass Spectrom*. 2019;442:35-43. doi:10.1016/j.ijms.2019.05.005
79. Dahl DA. SIMION for the personal computer in reflection. *InterJ Mass Spectrom*. 2000;200(1–3):3-25. doi:10.1016/S1387-3806(00)00305-5
80. Capone F, Colle Y, Hiernaut JP, Ronchi C. Mass spectrometric measurement of the ionization energies and cross sections of uranium and plutonium oxide vapors. *J Phys Chem A*. 1999;103(50):10899-10906. doi:10.1021/jp992405f
81. Levin RD, Lias SG, Ionization Potential and Appearance Potential Measurements, 1971–1981. : U.S. Dept. of Commerce, National Bureau of Standards; 1982 Available from: http://purl.access.gpo.gov/GPO/LPS113176. Accessed January 12, 2024.
82. Rosenstock HM, Draxl K, Steiner B, Herron J-T. *Energetics of Gaseous Ions*. National Standard Reference Data System; 1977.
83. Banon S, Chatillon C, Allibert M. High temperature mass spectrometric study of ionization and fragmentation of TiO and TiO_2 gas under electron impact. *High Temp Sci*. 1982;15(1):17-40.
84. Speight JG. *Lange's Handbook of Chemistry*. McGraw-Hill Education; 2017.
85. Knutsen GF, Searcy AW. Characterization of the gaseous and solid products of aluminum sulfate decomposition. *J Electrochem Soc*. 1978;125(2):327-330. doi:10.1149/1.2131439
86. Brittain RD, Hildenbrand DL. Catalytic effects in the decomposition behavior of metal sulfates. *J Electrochem Soc*. 1983;130(3):C104-C.
87. Drowart J, Chatillon C, Hastie J, Bonnell D. High-temperature mass spectrometry: instrumental techniques, ionization cross-sections, pressure measurements, and thermodynamic data—(IUPAC technical report). *Pure Appl Chem*. 2005;77(4):683-737. doi:10.1351/pac200577040683
88. Chatillon C, Allibert M, Pattoret A. Thermodynamic and physicochemical behavior of the interactions between Knudsen-effusion cells and the systems under investigation: analysis by high temperature mass spectrometry. In: *Characterization of High Temperature Vapors and Gases*. Vol.1. U. S. Government Printing Office; 1979:181-210.
89. Otvos JW, Stevenson DP. Cross-sections of molecules for ionization by electrons. *J Am Chem Soc*. 1956;78(3):546-551. doi:10.1021/ja01584a009
90. Mann JB. Ionization cross sections of elements calculated from mean-square radii of atomic orbitals. *J Chem Phys*. 1967;46(5):1646-1651. doi:10.1063/1.1840917
91. Mann JB. Ionization cross sections of elements. Recent development in mass-spectroscopy. In: *Proceedings of International Conference on Mass Spectroscopy*; 1969.
92. McFarland RH. Gryziński electron-impact ionization cross-section computations for the alkali metals. *Phys Ther Rev*. 1965;139(1A):A40-A42. doi:10.1103/PhysRev.139.A40
93. Bethe H. Zur theorie des durchgangs schneller korpuskularstrahlen durch materie. *Ann Phys*. 1930;397(3):325-400. doi:10.1002/andp.19303970303
94. Bell K, Gilbody H, Hughes J, Kingston A, Smith F. Recommended data on the electron impact ionization of light atoms and ions. *J Phys Chem Ref Data Monogr*. 1983;12(4):891-916. doi:10.1063/1.555700
95. Colle J-Y. *Knudsen Effusion Mass Spectrometry (KEMS-Online)* https://sites.google.com/site/kemsonline/home?authuser=0. Accessed January 12, 2024.
96. Freund RS, Wetzel RC, Shul RJ, Hayes TR. Cross-section measurements for electron-impact ionization of atoms. *Phys Rev A*. 1990;41(7):3575-3595. doi:10.1103/PhysRevA.41.3575
97. Younés C, Nguyen L, Pattoret A. Studies of the thermodynamic systems UO, Ce-O, U-Ce-O, U-La-O, Ce-La-O, and Ce-La-YO by mass spectrometry: improved assessment of uncertainties in derived thermodynamic data. *High Temp-High Press*. 1981;13(1).

98. Gotcu-Freis P, Colle J-Y, Guéneau C, Dupin N, Sundman B, Konings RJM. A thermodynamic study of the Pu–Am–O system. *J Nucl Mater*. 2011;414(3):408-421. doi:10.1016/j.jnucmat.2011.05.014
99. Kim Y-K, Rudd ME. Binary-encounter-dipole model for electron-impact ionization. *Phys Rev A*. 1994;50(5):3954-3967. doi:10.1103/PhysRevA.50.3954
100. Deutsch H, Schmidt M. On the quantitative-determination of cross-sections of ionization of molecules by electronic collisions. *Beit Plasmaphys-Cont*. 1984;24(5):475-486. doi:10.1002/ctpp.19840240504
101. Margreiter D, Walder G, Deutsch H, et al. Electron-impact ionization cross-sections of molecules 1. Experimental-determination of partial ionization cross-sections of SF_6—a case-study. *Int J Mass Spectrom*. 1990;100:143-156. doi:10.1016/0168-1176(90)85073-B
102. Margreiter D, Deutsch H, Mark TD. A semiclassical approach to the calculation of electron-impact ionization cross-sections of atoms—from hydrogen to uranium. *Int J Mass Spectrom*. 1994;139:127-139. doi:10.1016/0168-1176(94)90024-8
103. Mulliken RS. Electronic population analysis on LCAO [single bond] MO molecular wave functions. II. Overlap populations, bond orders, and covalent bond energies. *J Chem Phys*. 1955;23(10):1841-1846. doi:10.1063/1.1740589
104. El-Aneed A, Cohen A, Banoub J. Mass spectrometry, review of the basics: electrospray, MALDI, and commonly used mass analyzers. *Appl Spectrosc Rev*. 2009;44(3):210-230. doi:10.1080/05704920902717872
105. Hastie J. New techniques and opportunities in high temperature mass spectrometry. *Pure Appl Chem*. 1984;56(11):1583-1600. doi:10.1351/pac198456111583
106. Bonnell D, Plante E, Hastie J. Vaporization of simulated nuclear waste glass. *J Non Cryst Solids*. 1986;84(1–3):268-275. doi:10.1016/0022-3093(86)90785-4
107. Gotcu-Freis P, Colle JY, Hiernaut JP, Naisse F, Guéneau C, Konings RJM. Mass spectrometric studies of the vapour phase in the (Pu+O) system. *J Chem Thermodyn*. 2011;43(8):1164-1173. doi:10.1016/j.jct.2011.02.024
108. Trinadh VV, Manikandan P, Bera S, Brahmananda Rao CV, Lakshmi Narasimhan TS. Thermochemical properties over LiCl-KCl-UCl_3 ternary salt system: Knudsen effusion mass spectrometric study. *J Ph Equil Diff*. 2023;44(3):496-508. doi:10.1007/s11669-023-01053-z
109. Roboz J. *Introduction to Mass spectrometry; Instrumentation and Techniques*. Interscience; 1968.
110. Davis DW. A simple method for rapid calibration of faraday and ion counting detectors on movable multi-collector mass spectrometers. *J Mass Spectrom*. 2020;55(6):e4511. doi:10.1002/jms.4511
111. Marchand P, Paquet C, Marmet P. Near 100% efficiency ion detector for use with quadrupole mass filter. *Rev Sci Instrum*. 1966;37(12):1702-1704. doi:10.1063/1.1720090
112. Pottie R, Cocke D, Gingerich K. Discrimination in electron multipliers for atomic ions II. Comparison of yields for 61 atoms. *Int J Mass Spectrom*. 1973;11(1):41-48.
113. Leo WR. *Techniques for Nuclear and Particle Physics Experiments: A How-to Approach*. Springer Sci Bus Media; 2012.
114. Dietz LA. Basic properties of electron multiplier ion detection and pulse counting methods in mass spectrometry. *Rev Sci Instrum*. 1965;36(12):1763-1770. doi:10.1063/1.1719460
115. Bale CW, Chartrand P, Degterov SA, et al. FactSage thermochemical software and databases. *CAL*. 2002;26(2):189-228. doi:10.1016/S0364-5916(02)00035-4
116. Andersson JO, Helander T, Hoglund LH, Shi PF, Sundman B. THERMO-CALC & DICTRA, computational tools for materials science. *CAL*. 2002;26(2):273-312. doi:10.1016/S0364-5916(02)00037-8
117. Snyder GA, Neal CR, Taylor LA, Halliday AN. Anatexis of lunar cumulate mantle in time and space: clues from trace-element, strontium, and neodymium isotopic chemistry of parental Apollo 12 basalts. *Geochim Cosmochim ac*. 1997;61(13):2731-2747. doi:10.1016/S0016-7037(97)00082-3
118. De Maria G, Balducci G, Guido M, Piacente V (Eds). Mass spectrometric investigation of the vaporization process of Apollo 12 lunar samples. In: *Lunar and Planetary Science Conference Proceedings*. Vol.2; 1971:1367.
119. Dushman S. *Scientific Foundations of Vacuum Technique*. John Wiley; 1949.
120. https://www.normandale.edu/academics/degrees-certificates/vacuum-and-thin-film-technology/the-danielson-collection.html Accessed January 12, 2024
121. Tmar M, Gabriel A, Chatillon C, Ansara I. Critical analysis and optimization of the thermodynamic properties and phase diagrams in the III-V compounds: the In-P and Ga-P systems. *J Cryst Growth*. 1984;68(2):557-580. doi:10.1016/0022-0248(84)90464-0
122. Anderson T, Colinet C, Chatillon C, Tmar M. Calorimetric and Knudsen effusive studies of the thermochemical properties of $Ga_xIn_{1-x}P$ alloys. *J Cryst Growth*. 1987;83(2):252-260. doi:10.1016/0022-0248(87)90015-7
123. Colle JY, Freis D, Beneš O, Konings RJM. Knudsen effusion mass spectrometry of nuclear materials: applications and developments. *ECS Trans*. 2013;46(1):23-38. doi:10.1149/04601.0023ecst
124. Huang J, Furukawa T, Aoto K. Thermodynamic study of sodium–iron oxides: part I. Mass spectrometric study of Na–Fe oxides. *Thermochim Acta*. 2003;405(1):61-66. doi:10.1016/S0040-6031(03)00136-9
125. Raj DDA, Viswanathan R, Manikandan P. The design, construction, and testing of a Knudsen effusion mass spectrometric system suitable for studies of nuclear fuel materials. *ECS Transactions*. 2013;46(1):77-97. doi:10.1149/04601.0077ecst
126. Souček P, Beneš O, Claux B, et al. Synthesis of UF_4 and ThF_4 by HF gas fluorination and re-determination of the UF_4 melting point. *J Fluorine Chem*. 2017;200:33-40. doi:10.1016/j.jfluchem.2017.05.011
127. Colle J-Y, Rautio J, Freis D. A modular LabVIEW application frame for Knudsen effusion mass spectrometry instrument control. *SoftwareX*. 2021;16:100875. doi:10.1016/j.softx.2021.100875
128. Dunaev A, Kryuchkov A, Kudin L, Butman M. Automated complex for high-temperature researches on base of mass-spectrometer MI1201. *Izvestiya Vysshikh Uchebnykh Zavedenii Seriya Khimiya I Khimicheskaya Tekhnologiya*. 2011;54(8).
129. Seelig J, Ghosh T, Jacobson N, et al. Sorption of Ag and its vaporization from graphite at high temperatures. *J Nucl Mater*. 2017;493:132-146. doi:10.1016/j.jnucmat.2017.06.002
130. Lewis GN, Randall M. Revised by: Pitzer KS, Brewer L, eds. *Thermodynamics*. 2nd ed., McGraw Hill, 1961.
131. Cubicciotti D. A new sigma-plot treatment of equilibrium data and its application to vaporization of bismuth chloride. *J Phys Chem*. 1966;70(7):2410-2413. doi:10.1021/j100879a504
132. Jacobson NS, Myers DL. High-temperature vaporization of B_2O_3 under reducing conditions. *J Phys Chem B*. 2011;115(45):13253-13260. doi:10.1021/jp206480d
133. Hildenbrand DL, Lau KH. Thermochemistry of gaseous manganese oxides and hydroxides. *J Chem Phys*. 1994;100(11):8377-8380. doi:10.1063/1.466783
134. Hildenbrand DL, Lau KH. Thermochemistry of gaseous SiO (OH), SiO $(OH)_2$, and SiO_2. *J Chem Phys*. 1994;101(7):6076-6079. doi:10.1063/1.467322
135. Nguyen QN, Bauschlicher C Jr, Myers DL, Jacobson NS, Opila EJ. Computational and experimental study of thermodynamics of the reaction of titania and water at high temperatures. *J Phys Chem A*. 2017;121(49):9508-9517. doi:10.1021/acs.jpca.7b08614

136. Dunning TH Jr. Gaussian basis sets for use in correlated molecular calculations. I. The atoms boron through neon and hydrogen. *J Chem Phys*. 1989;90(2):1007-1023. doi:10.1063/1.456153
137. Kendall RA, Dunning TH Jr, Harrison RJ. Electron affinities of the first-row atoms revisited. Systematic basis sets and wave functions. *J Chem Phys*. 1992;96(9):6796-6806. doi:10.1063/1.462569
138. Balabanov NB, Peterson KA. Systematically convergent basis sets for transition metals. I. All-electron correlation consistent basis sets for the 3 d elements Sc–Zn. *J Chem Phys*. 2005;123(6):064107. doi:10.1063/1.1998907
139. Bauschlicher CW Jr, Jacobson NS, Myers DL, Opila EJ. Computational chemistry derivation of Cr, Mn, and La hydroxide and oxyhydroxide thermodynamics. *J Phys Chem A*. 2022;126(9):1551-1561. doi:10.1021/acs.jpca.2c00764
140. Chase MW. *NIST-JANAF Thermochemical Tables*. 4thed. American Chemical Society; American Institute of Physics for the National Institute of Standards and Technology; 1998.
141. Barin I. *Thermochemical Data of Pure Substances*. Thirded. VCH; 1995. doi:10.1002/9783527619825
142. Drowart J, Honig R. A mass spectrometric method for the determination of dissociation energies of diatomic molecules. *J Phys Chem*. 1957;61(7):980-985. doi:10.1021/j150553a032
143. Gingerich K. Mass-spectrometric determination of bond energies of high-temperature molecules. *Chimia*. 1972;26(12):619-623.
144. Gingerich KA. Mass spectrometric determination of atomization energies of inorganic molecules and their correlation by empirical models of bonding. In: Hastie JW, ed. *Characterization of High Temperature Vapors and Gases*. Vol.1(561). U. S. Government Printing Office; 1979:289-300.
145. Smoes S, Drowart J, Verhaegen G. Mass-spectrometric study of gaseous oxides and suboxides of scandium, yttrium, and lanthanum. *J Chem Phys*. 1965;43(2):732-736. doi:10.1063/1.1696798
146. Hilpert K, Gingerich KA. Atomization enthalpies of the molecules Cu-3, Ag-3, and Au-3. *Ber Bunsen Phys Chem*. 1980;84(8):739-745. doi:10.1002/bbpc.19800840810
147. Gingerich KA. Experimental and predicted stability of diatomic metals and metallic clusters. In: *Faraday Symposia of the Chemical Society Royal Society of Chemistry*. Vol.14; 1980:109-125. doi:10.1039/fs9801400109
148. Gingerich KA, Shim I, Gupta S, Kingcade J Jr. Bond energies of small metal clusters. *Surf Sci*. 1985;156:495-503. doi:10.1016/0039-6028(85)90611-9
149. Shim I, Gingerich KA. Ab initio HF–CI calculations of the electronic "band structure" in the Fe_2 molecule. *J Chem Phys*. 1982;77(5):2490-2497. doi:10.1063/1.444120
150. Roki F-Z, Ohnet M-N, Fillet S, Chatillon C, Nuta I. Critical assessment of thermodynamic properties of CsI solid, liquid and gas phases. *J Chem Thermodyn*. 2014;70:46-72. doi:10.1016/j.jct.2013.09.038
151. Moore R, Robinson D, Argent B. The use of high resolution mass spectrometry in the measurement of thermodynamic properties of metallic systems. *J Phys E Sci Instrum*. 1975;8(8):641-648. doi:10.1088/0022-3735/8/8/010
152. Chatillon C, Pattoret A, Drowart J. Thermodynamic studies of condensed phases by high temperature mass spectrometry. *High Temper-High Press*. 1975;7(2):119-148.
153. Lupis CH. *Chemical Thermodynamics of Materials*. Elsevier Science Publishing Co, Inc; 1983:581.
154. Eckert M, Bencze L, Kath D, Nickel H, Hilpert K. Thermodynamic activities in the alloys of the Ti-Al system. *Ber Bunsen Phys Chem*. 1996;100(4):418-424.
155. Jacobson NS, Brady MP, Mehrotra GM. Thermodynamics of selected Ti-Al and Ti-Al-Cr alloys. *Oxid Met*. 1999;52(5–6):537-556. doi:10.1023/A:1018820401533
156. Costa GC, Jacobson NS. Mass spectrometric measurements of the silica activity in the Yb_2O_3–SiO_2 system and implications to assess the degradation of silicate-based coatings in combustion environments. *J Eur Ceram Soc*. 2015;35(15):4259-4267. doi:10.1016/j.jeurceramsoc.2015.07.019
157. Lee MY, Adams A. A combination compact Knudsen cell-mass spectrometer apparatus for alloy studies. *High Temp Sci*. 1988;25(2):103-116.
158. Chatillon C, Allibert M, Moracchioli R, Pattoret A. Etudes thermochimiques à haute température par spectrométrie de masse: emploi de dispositifs à caloducs pour le maintien isotherme de cellules d'effusion [Rapport de recherche]. *LTPCM*. 1974;21. hal-01364059
159. Gurvich LV, Veyts IV, Alcock CB. Thermodynamic Properties of Individual Substances. In: *Institut vysokikh temperatur (akademi ia⌒ nauk SSSR), and gosudarstvennyĭ institut prikladnoĭ khimii (Soviet Union)*. 4th ed. Hemisphere Pub. Corp.; 1989.
160. Hultgren R, Desai PD, Hawkins DT, Gleiser M, Kelley KK, Wagman DD. *Selected Values of the Thermodynamic Properties of the Elements*. American Society for Metals; 1973.
161. Schiffman R. Thermodynamics of the ytterbium-lead system by simultaneous weight-loss-mass-spectrometry Knudsen effusion. *J Phys Chem*. 1982;86(19):3855-3861. doi:10.1021/j100216a030
162. Drowart J, Pattoret A, Smoes S. The heat of sublimation of uranium and the consistency of the thermodynamic data for uranium compounds. *J Nucl Mater*. 1964;12(3):319-322. doi:10.1016/0022-3115(64)90086-8
163. Lyubimov A, Zobens VY, Rakhovskii V. A mass spectrometric determination of the thermodynamic characteristics of binary metallic systems. *Zhur Fiz Khim*. 1958;32.
164. Neckel A, Wagner S. Massenspektrometrische Bestimmung thermodynamischer Aktivitäten. I. Das system gold–Kupfer. *Berich Bunsen Gesell*. 1969;73(2):210-217. doi:10.1002/bbpc.19690730221
165. Belton GR, Fruehan RJ. Determination of activities by mass spectrometry. I. The liquid metallic systems iron-nickel and iron-cobalt. *J Phys Chem*. 1967;71(5):1403-1409. doi:10.1021/j100864a034
166. Belton GR, Fruehan RJ. The determination of activities by mass-spectrometry—some additional methods. *Metall Trans A*. 1971;2(1):291-296. doi:10.1007/BF02662673
167. Korobov M, McCreary J, Kematick R, Myers C. The ion-current-ratio method in Knudsen-cell mass spectrometry: binary mixtures with stoichiometric intermediate phases. *J Chem Thermodyn*. 1992;24(12):1275-1279. doi:10.1016/S0021-9614(05)80267-8
168. Neckel A, Wagner S. Massenspektrometrische Bestimmung thermodynamischer Aktivitäten in Dreistoffsystemen. *Monatsh Chem*. 1969;100(2):664-670. doi:10.1007/BF00904114
169. Berkowitz J, Chupka W. Composition of vapors in equilibrium with salts at high temperatures. *Ann N Y Acad Sci*. 1960;79(11):1073-1078. doi:10.1111/j.1749-6632.1960.tb42773.x
170. Pattoret A, Drowart J, Smoes S. Mass spectrometric determination of heat of sublimation of uranium. *T Faraday Soc*. 1969;65:98-112. doi:10.1039/tf9696500098
171. Drowart J, Pattoret A, Smoes S. Concerning the influence of oxygen on the vapor pressure of uranium. *J Chem Phys*. 1965;42(7):2629-2630. doi:10.1063/1.1696358
172. Howard SM. Direct activity measurements in liquid Ag—Cu alloys using a valved Knudsen cell-mass spectrometer system. *Metall Mater Trans B*. 1989;20(6):845-852. doi:10.1007/BF02670189
173. Oktay E. The thermodynamic activities of silver in liquid silver-copper-germanium alloys/Thermodynamische Aktivitäten von Ag in flüssigen Ag-Cu-Ge-Legierungen. *Inter J Mater Res*. 1994;85(12):824-827. doi:10.1515/ijmr-1994-851204

174. Baud S, Thévenot F, Pisch A, Chatillon C. High temperature sintering of SiC with oxide additives: I. Analysis in the SiC–Al_2O_3 and SiC–Al_2O_3–Y_2O_3 systems. *J Eur Ceram Soc*. 2003;23(1):1-8. doi:10.1016/S0955-2219(02)00067-5
175. Copland E. Solidification behavior of gamma'-Ni_3Al-containing alloys in the Ni-Al-O system. *Acta Mater*. 2007;55(14):4853-4865. doi:10.1016/j.actamat.2007.05.011
176. Kattner UR. The thermodynamic modeling of multicomponent phase equilibria. *JOM*. 1997;49(12):14-19. doi:10.1007/s11837-997-0024-5
177. Bencze L, Raj DD, Kath D, Oates WA, Singheiser L, Hilpert K. Thermodynamic properties and diffusion thermodynamic factors in B2-NiAl. *Metall Mater Trans B*. 2004;35(5):867-876. doi:10.1007/s11663-004-0081-x
178. Steiner A, Komarek K. Thermodynamic activities of solid nickel-aluminum alloys. *Trans AIME*. 1964;230:786.
179. Oforka N, Argent B. Thermodynamics of Ni-Cr-Al alloys. *J Less-Common Met*. 1985;114(1):97-109. doi:10.1016/0022-5088(85)90394-7
180. Wang J, Engell HJ. Investigation of the thermodynamic properties of Ni-Al intermetallic compounds by an EMF method. *Steel Res*. 1992;63(8):320-323. doi:10.1002/srin.199200527
181. Chatain S, Alpettaz T, Gossé S, Guéneau C. Thermodynamic activity measurements in nickel-base industrial alloys and steels by Knudsen cell–mass spectrometry. *J Chem Thermodyn*. 2017;114:144-150. doi:10.1016/j.jct.2017.01.015
182. Spathara D, Sergeev D, Kobertz D, Mueller M, Putman D, Warnken N. Thermodynamic study of single crystal, Ni-based superalloys in the γ+ γ' two-phase region using Knudsen effusion mass spectrometry. *DSC SEM J Alloy Compd*. 2021;870:159295. doi:10.1016/j.jallcom.2021.159295
183. Copland EH, Jacobson NS, Hilpert K, Kath D. Thermodynamics of the Ti–Al–O system. *CAL*. 2022;77:102400. doi:10.1016/j.calphad.2022.102400
184. Allibert M, Chatillon C. Mass spectrometry measurements of CaF_2 and CaO activities in CaF_2–CaO–Al_2O_3 slags at 1700K. *Can Metall Quart*. 1979;18(3):349-354. doi:10.1179/cmq.1979.18.3.349
185. Stolyarova V. Mass spectrometric thermodynamic studies of oxide systems and materials. *Russ Chem Rev*. 2016;85(1):60-80. doi:10.1070/RCR4549
186. Stolyarova VL. High temperature mass spectrometric study of oxide systems and materials. *Rapid Commun Mass Spectrom*. 1993;7(11):1022-1032. doi:10.1002/rcm.1290071112
187. Stolyarova V. Vaporization features of oxide systems studied by high-temperature mass spectrometry. *J Nucl Mater*. 1997;247:7-10. doi:10.1016/S0022-3115(97)00025-1
188. Stolyarova V. Vaporization processes and thermodynamic properties of oxide systems studied by high temperature mass spectrometry. *ECS Transactions*. 2013;46(1):55-67. doi:10.1149/04601.0055ecst
189. Stolyarova V. High temperature mass spectrometric study of thermodynamic properties and vaporization processes of oxide systems: experiment and modeling. *Open Thermodyn J*. 2013;7(1):57-70. doi:10.2174/1874396X01307010057
190. Stolyarova V. Review KEMS 2012 till 2017. *CAL*. 2019;64:258-266. doi:10.1016/j.calphad.2018.12.013
191. Stolyarova V. A mass spectrometric study of the thermodynamic properties of oxide melts. *Glass Phys Chem*. 2001;27(1):3-15. doi:10.1023/A:1009599502138
192. Stolyarova VL. Vaporization features of glass forming melts studies by high temperature mass spectrometry. *Glass Phys Chem*. 2002;43C:330-338.
193. Stolyarova V, Plotnikov E. Vaporization processes and thermodynamic properties of oxide systems at high temperatures: experimental study and modeling. *Glass Phys Chem*. 2005;31(1):30-43. doi:10.1007/s10720-005-0022-z
194. Stolyarova V. Thermodynamic properties and structure of ternary silicate glass-forming melts: experimental studies and modeling. *J Non Cryst Solids*. 2008;354(12–13):1373-1377. doi:10.1016/j.jnoncrysol.2006.10.087
195. Stolyarova V, Petersburg S. Vaporization and thermodynamics of glass-forming oxide melts: mass spectrometric study and modeling. *J Mater Sci Chem Eng*. 2015;3(07):81-86. doi:10.4236/msce.2015.37009
196. Stolyarova VL. Vaporization and thermodynamics of glasses and glass-forming melts in ternary oxide systems. *Appl sol St Chem*. 2017;1(1):26-30. doi:10.18572/2619-0141-2017-1-1-26-30
197. Stolyarova VL. *Ceramics based on the hafnium and rare-earth elements oxides: mass specrometric study and modeling*. Trudy Kolyskogo Nauchnogo Tzentra; 2015:5.
198. Stolyarova VL, Vorozhtcov VA. Features of thermodynamic description of the systems based hafnium and rare-earth oxides at high temperatures. *Trudy Kolyskogo Nauchnogo Tzentra*. 2018;9(2):104-107.
199. Stolyarova V, Vorozhtcov V. High temperature behavior of oxide systems containing rare earth elements. *Theor Found Chem Eng*. 2022;56(4):600-608. doi:10.1134/S0040579522040170
200. Stolyarova V, Vorozhtcov V. The potential of the Wilson method in the calculation of the thermodynamic properties of oxide systems at high temperatures. *Russ J Inorg Chem*. 2021;66(9):1396-1404. doi:10.1134/S0036023621090163
201. Vorozhtcov VA, Stolyarova VL. Semiempirical methods for calculating liquidus temperatures in oxide systems. *Tech Phys*. 2021;66(8):958-968. doi:10.1134/S1063784221060219
202. Stolyarova V, Vorozhtcov V. High temperature study of oxide systems: thermal analysis and Knudsen effusion mass spectrometry. *Russ J Phys Chem A*. 2020;94(13):2640-2647. doi:10.1134/S0036024420130257
203. Lopatin SI. Stability of gaseous salts of oxygen-containing acids. *Russ J gen Chem*. 1999;69(9):1364-1367.
204. Lopatin S. Regularities of the vaporization of oxygen-containing acid salts. *Glass Phys Chem*. 2003;29(4):390-396. doi:10.1023/A:1025177027457
205. Lopatin S. Thermodynamic properties of gaseous salts of oxygen-containing acids. *Zh Fiz Khim*. 2003;77(10):1748-1751.
206. Lopatin S, Shugurov S, Semenov G. Gaseous associates over oxide materials. *Inorg Mater*. 2005;41(12):1340-1344. doi:10.1007/s10789-005-0312-9
207. Lopatin S, Stolyarova V. Thermodynamic properties and structure of gaseous metaborates. *Glass Phys Chem*. 2006;32(3):353-369. doi:10.1134/S1087659606030163
208. Lopatin S. Gaseous salts of oxygen-containing acids: thermal stability, structure, and thermodynamic properties. *Russ J gen Chem*. 2007;77(11):1823-1854. doi:10.1134/S1070363207110011
209. Lopatin S, Shugurov S. Inorganic associates in a high-temperature vapor. *Russ J gen Chem*. 2019;89(6):1059-1068. doi:10.1134/S107036321906001X
210. Kablov EN, Stolyarova VL, Vorozhtcov VA, Lopatin SI, Karachevtsev FN. Thermodynamics and vaporization of ceramics based on the Y_2O_3-ZrO_2 system studied by KEMS. *J Alloys Compd*. 2019;794:606-614. doi:10.1016/j.jallcom.2019.04.208
211. Stolyarova VL, Vorozhtcov VA, Lopatin SI, et al. High-temperature mass spectrometric study of vaporization and thermodynamics of the Cs_2O-B_2O_3 system: Review and experimental investigation. *Rapid Commun Mass Spectrom*. 2021;35(11):e9079. doi:10.1002/rcm.9079
212. Stolyarova VL, Vorozhtcov VA, Lopatin SI, et al. Vaporization and thermodynamics of the Cs_2O–MoO_3 system studied using high-

temperature mass spectrometry. *Rapid Commun Mass Spectrom*. 2021;35(12):e9097. doi:10.1002/rcm.9097

213. Stolyarova V, Lopatin S, Selyutin A, Vorozhtcov V, Shugurov S. Vaporization and thermodynamic properties of $SrO–Al_2O_3$ ceramics at high temperatures. *Russ J Inorg Chem*. 2022;67(12):2077-2083. doi:10.1134/S0036023622601428
214. Stolyarova VL, Vorozhtcov VA, Lopatin SI, et al. Mass spectrometric study and modeling of the thermodynamic properties of $SrO–Al_2O_3$ melts at high temperatures. *Rapid Commun Mass Spectrom*. 2023;37(5):e9459. doi:10.1002/rcm.9459
215. Gribchenkova N, Smirnov A, Smorchkov K, Belova E, Alikhanyan A. Thermodynamic characteristics of zinc niobates $Zn_3Nb_2O_8$, $ZnNb_2O_6$, and $Zn_2Nb_{34}O_{87}$. p–x diagram of the $ZnO–Nb_2O_5$ system. *Russ J Inorg Chem*. 2021;66(12):1873-1879. doi:10.1134/S0036023621120044
216. Stolyarova V, Vorozhtcov V, Shemchuk D, Lopatin S, Bogdanov O. High temperature mass spectrometric study of the $TiO_2–Al_2O_3$ system. *Russ J gen Chem*. 2021;91(10):1999-2007. doi:10.1134/S107036322110011X
217. Stolyarova VL, Vorozhtcov VA, Shemchuk DV, et al. High-temperature mass spectrometric study of thermodynamic properties in the $TiO_2–Al_2O_3–SiO_2$ system and modeling. *Rapid Commun Mass Spectrom*. 2022;36(19):e9359. doi:10.1002/rcm.9359
218. Stolyarova VL, Shilov AL, Lopatin SI, et al. High-temperature mass spectrometric study and modeling of ceramics based on the Al_2O_3-SiO_2-ZrO_2 system. *Rapid Commun Mass Spectrom*. 2023;37(3):e9433. doi:10.1002/rcm.9433
219. Kablov EN, Shilov AL, Stolyarova VL, et al. Thermodynamics and vaporization of ceramics based on the Gd_2O_3-ZrO_2 and Gd_2O_3-HfO_2 systems studied by KEMS. *J Alloys Compd*. 2022;908:164575. doi:10.1016/j.jallcom.2022.164575
220. Kablov EN, Stolyarova VL, Vorozhtcov VA, et al. High-temperature mass spectrometric study of the thermodynamic properties in the Sm_2O_3-ZrO_2-HfO_2 system. *Rapid Commun Mass Spectrom*. 2022;36(7):e9238. doi:10.1002/rcm.9238
221. Doronin O, Artemenko N, Stekhov P, Marakhovskii P, Stolyarova V, Vorozhtsov V. Physicochemical properties of $Gd_2O_3–ZrO_2–HfO_2$ ceramics as promising thermal barrier coatings. *Russ J Inorg Chem*. 2022;67(5):732-739. doi:10.1134/S0036023622050060
222. Vorozhtcov V, Yurchenko D, Almjashev V, Stolyarova V. Phase equilibriums in the $Al_2O_3–SiO_2–ZrO_2$ system: calculation and experiment. *Glass Phys Chem*. 2021;47(5):417-426. doi:10.1134/S1087659621050175
223. Kablov EN, Shilov AL, Stolyarova VL, et al. Mass spectrometric study and modeling of the thermodynamic properties in the Gd_2O_3-ZrO_2-HfO_2 system at high temperatures. *Rapid Commun Mass Spectrom*. 2022;36(13):e9306. doi:10.1002/rcm.9306
224. Vorozhtcov VA, Kirillova SA, Shilov AL, Lopatin SI, Stolyarova VL. The hafnia-based ceramics containing lanthana or samaria: mass spectrometric study and calculation of the thermodynamic properties at high temperatures. *Mater Today Commun*. 2021;29:102952. doi:10.1016/j.mtcomm.2021.102952
225. Vorozhtcov V, Stolyarova V, Kirillova S, Lopatin S, Shilov A. Thermodynamic properties of quaternary systems based on hafnia: a high-temperature mass spectrometric study and modeling. *Russ Chem Bull*. 2023;72(1):148-157. doi:10.1007/s11172-023-3719-z
226. Barker JA. Cooperative orientation effects in solutions. *J Chem Phys*. 1952;20(10):1526-1532. doi:10.1063/1.1700209
227. https://www.oecd-nea.org/jcms/pl_24703/thermodynamics-of-advanced-fuels-international-database-taf-id Accessed January 12, 2024.
228. Saunders N, Miodownik AP. *CALPHAD (Calculation of Phase Diagrams): A Comprehensive Guide*. Elsevier; 1998.
229. Gaskell D. Thermodynamic models of liquid silicates. *Can Metall Quart*. 1981;20(1):3-19. doi:10.1179/cmq.1981.20.1.3
230. Eriksson G, Hack K. ChemSage—a computer program for the calculation of complex chemical equilibria. *Metall Trans B*. 1990;21(6):1013-1023. doi:10.1007/BF02670272
231. Eriksson G, Hack K. Calculation of phase equilibria in multicomponent alloy systems using a specially adapted version of the program 'SOLGASMIX'. *CAL*. 1984;8(1):15-24. doi:10.1016/0364-5916(84)90025-7
232. Redlich O, Kister A. Algebraic representation of thermodynamic properties and the classification of solutions. *Ind Eng Chem*. 1948;40(2):345-348. doi:10.1021/ie50458a036
233. Hillert M. Partial gibbs energies from Redlich-Kister polynomials. *Thermochim Acta*. 1988;129(1):71-75. doi:10.1016/0040-6031(88)87198-3
234. Popovic A, Bencze L. Mass spectrometric determination of ternary interaction parameters of liquid cu–in–Sn alloy. *Int J Mass Spectrom*. 2006;257(1–3):41-49.
235. Oates WA, Bencze L, Markus T, Hilpert K. Thermodynamic properties of B2-AlFeNi alloys: modelling of the B2-AlFe and B2-AlNi phases. *Inter J Mater Res*. 2006;97(6):812-820. doi:10.3139/146.101308
236. Bencze L, Henriques D, Motalov V, Markus T. Thermodynamic modelling of Li–Sn liquid alloy based on Knudsen effusion mass spectrometric measurements. *J Alloys Compd*. 2014;607:183-192. doi:10.1016/j.jallcom.2014.03.166
237. Pelton AD, Blander M. Thermodynamic analysis of ordered liquid solutions by a modified quasichemical approach—application to silicate slags. *Metall Trans B*. 1986;17(4):805-815. doi:10.1007/BF02657144
238. Wu P, Eriksson G, Pelton AD, Blander M. Prediction of the thermodynamic properties and phase diagrams of silicate systems—evaluation of the FeO-MgO-SiO2 system. *ISIJ Inter*. 1993;33(1):26-35. doi:10.2355/isijinternational.33.26
239. Gokcen NA, Chang ET, Marx PC. *Novel Uses of Knudsen Cells at High Temperatures. High Temperature Technology*. Butterworth & Co.; 1969:611-627.
240. Nunoue SY, Kato E. Mass-spectrometric study of the partial phase-diagram of the Fe-Ge system above 1050-degrees-C. *Metall Trans A*. 1989;20(5):975-976. doi:10.1007/BF02651663
241. Roberts JA Jr, Searcy AW. Anomalous temperature dependence for a partial vapor pressure. *Science*. 1977;196(4289):525-527. doi:10.1126/science.196.4289.525
242. Jones CY, Edwards JG. Observation of a phase transformation of Ga_2S_3 in a quartz effusion cell above 1230 K by means of neutron scattering. *J Phys Chem B*. 2001;105(14):2718-2724. doi:10.1021/jp003312x
243. Fleischer R. High-temperature, high-strength materials—an overview. *JOM*. 1985;37(12):16-20. doi:10.1007/BF03259961
244. Kablov EN, Stolyarova VL, Vorozhtcov VA, et al. Vaporization and thermodynamics of ceramics in the Sm_2O_3-Y_2O_3-HfO_2 system. *Rapid Commun Mass Spectrom*. 2020;34(8):e8693. doi:10.1002/rcm.8693
245. Brewer L, Haraldsen H. The thermodynamic stability of refractory borides. *J Electrochem Soc*. 1955;102(7):399. doi:10.1149/1.2430108
246. Storms E, Mueller B. Phase relations and thermodynamic properties of transition metal borides. I. The molybdenum-boron system and elemental boron. *J Phys Chem*. 1977;81(4):318-324. doi:10.1021/j100519a008
247. Brutti S, Balducci G, Ciccioli A, Gigli G. Thermodynamic assessment of the Yb–Si system. *CAL*. 2005;29(3):254-261. doi:10.1016/j.calphad.2005.06.004

248. Brutti S, Ciccioli A, Balducci G, Gigli G, Manfrinetti P, Palenzona A. Vaporization thermodynamics of MgB_2 and MgB_4. *Appl Phys Lett*. 2002;80(16):2892-2894. doi:10.1063/1.1471382
249. Drowart J, Burns RP, DeMaria G, Inghram MG. Mass spectrometric study of carbon vapor. *J Chem Phys*. 1959;31(4):1131-1132. doi:10.1063/1.1730519
250. Storms EK. *The Refractory Carbides*. Academic Press; 1967. doi:10.1016/B978-1-4832-3070-2.50004-5
251. Coltters R. Thermodynamics of binary metallic carbides: a review. *Mater Sci Eng A*. 1985;76:1-50. doi:10.1016/0025-5416(85)90078-3
252. Drowart J, De Maria G, Inghram MG. Thermodynamic study of SiC utilizing a mass spectrometer. *J Chem Phys*. 1958;29(5):1015-1021. doi:10.1063/1.1744646
253. Rocabois P, Chatillon C, Bernard C, Genet F. Thermodynamics of the Si-C system II. Mass spectrometric determination of the enthalpies of formation of molecules in the gaseous phase. *High Temp-High Press*. 1995;27(1):25-39. doi:10.1068/htrt34
254. Behrens RG, Rinehart GH. Vaporization thermodynamics and kinetics of hexagonal silicon carbide. In: Haste JW, ed. *Characterisation of High Temperature Vapors and Gases*. Vol.1. U. S. Government Printing Office; 1979:125-142.
255. Davis SG, Anthrop DF, Searcy AW. Vapor pressure of silicon and the dissociation pressure of silicon carbide. *J Chem Phys*. 1961;34(2):659-664. doi:10.1063/1.1701004
256. Kohl FJ, Stearns CA. Vaporization and dissociation energies of the molecular carbides of titanium, zirconium, hafnium, and thorium. *High Temp Sci*. 1974;6(4):284-302.
257. Gupta SK, Gingerich KA. Mass spectrometric study of the stabilities of gaseous carbides of vanadium, niobium, and molybdenum. *J Chem Phys*. 1981;74(6):3584-3590. doi:10.1063/1.441463
258. Gupta SK, Gingerich KA. Observation and atomization energies of the gaseous uranium carbides, UC, UC_2, UC_3, UC_4, UC_5, and UC_6 by high temperature mass spectrometry. *J Chem Phys*. 1979;71(7):3072-3080. doi:10.1063/1.438713
259. Yamawaki M, Koyama T, Takahashi Y. Thermodynamics of the vaporization of non-stoichiometric thorium monocarbide $ThC_{1\pm x}$. *J Nucl Mater*. 1989;167:113-121. doi:10.1016/0022-3115(89)90431-5
260. Koyama T, Yamawaki M. High-temperature vaporization of thorium-uranium mixed monocarbide (Th_{1-y}, U_y) C. *J Nucl Mater*. 1989;167:122-126. doi:10.1016/0022-3115(89)90432-7
261. Rocabois P, Chatillon C, Bernard C. Thermodynamics of the Si-O-N system 1. High-temperature study of the vaporization behavior of silicon nitride by mass spectrometry. *J Am Ceram Soc*. 1996;79(5):1351-1360. doi:10.1111/j.1151-2916.1996.tb08596.x
262. Kohl FJ, Stearns CA. Identification and dissociation energy of gaseous hafnium mononitride. *J Phys Chem*. 1974;78(3):273-274. doi:10.1021/j100596a016
263. Stearns CA, Kohl FJ. *The dissociation energy of gaseous titanium mononitride*. National Aeronautics and Space Administration; NASA TN D-5207; 1969.
264. Gingerich KA. Gaseous metal nitrides. II. The dissociation energy, heat of sublimation, and heat of formation of zirconium mononitride. *J Chem Phys*. 1968;49(1):14-18. doi:10.1063/1.1669799
265. Gingerich KA. Vaporization of uranium mononitride and heat of sublimation of uranium. *J Chem Phys*. 1969;51(10):4433-4439. doi:10.1063/1.1671809
266. Gingerich KA. Gaseous metal nitrides. III. On the dissociation energy of thorium mononitride and predicted dissociation energies of diatomic group III–VI transition-metal nitrides. *J Chem Phys*. 1968;49(1):19-24. doi:10.1063/1.1669808
267. Granier B, Chatillon C, Allibert M. Thermodynamic activities in the cubic phase Ti-O-N by high-temperature mass spectrometry. *J Am Ceram Soc*. 1982;65(10):465-469. doi:10.1111/j.1151-2916.1982.tb10334.x
268. Kematick R, Myers C. Thermodynamics of the phase formation of the titanium silicides. *Chem Mater*. 1996;8(1):287-291. doi:10.1021/cm950386q
269. Lexa D, Kematick RJ, Myers CE. Thermodynamics of phase formation of the cobalt silicides. *Chem Mater*. 1996;8(11):2636-2642. doi:10.1021/cm9601796
270. Myers CE, Murray GA, Kematick RJ, Frisch MA. *Vaporization Thermodynamics of Chromium Silicides. Report ADRA162-286*. Office of Naval Research; 1985.
271. Markova O, Yakovlev O, Semenov G, Belov A. Evaporation of natural melts in a Knudsen chamber. *Geokhimiya*. 1986;11:1559-1568.
272. Rammensee W, Fraser DG. Determination of activities in silicate melts by Knudsen cell mass spectrometry—I. The system $NaAlSi_3O_8$-$KAlSi_3O_8$. *Geochim Cosmochim Acta*. 1982;46(11):2269-2278. doi:10.1016/0016-7037(82)90200-9
273. Fraser DG, Rammensee W, Hardwick A. Determination of the mixing properties of molten silicates by Knudsen cell mass spectrometry—II. The systems (Na K)$AlSi_4O_{10}$, and (Na-K)$AlSi_5O_{12}$. *Geochim Cosmochim Acta*. 1985;49(2):349-359. doi:10.1016/0016-7037(85)90028-6
274. Lock SJ, Stewart ST, Petaev MI, et al. The origin of the moon within a terrestrial synestia. *J Geophys Res-Planet*. 2018;123(4):910-951. doi:10.1002/2017JE005333
275. Ivanov D, Fitoussi C, Bourdon B. Trace element volatility and the conditions of liquid-vapor separation in the proto-lunar disk. *Icarus*. 2022;386:115143. doi:10.1016/j.icarus.2022.115143
276. Fegley B Jr, Lodders K, Jacobson NS. Chemical equilibrium calculations for bulk silicate earth material at high temperatures. *Geochemistry*. 2023;83(2):125961. doi:10.1016/j.chemer.2023.125961
277. Wolf AS, Jäggi N, Sossi PA, Bower DJ. VapoRock: thermodynamics of vaporized silicate melts for modeling volcanic outgassing and magma ocean atmospheres. *Astrophys J*. 2023;947(2):64. doi:10.3847/1538-4357/acbcc7
278. Bischof L, Sossi PA, Sergeev D, Müller M, Schmidt MW. Vaporisation of group 13 elements from basaltic melts by Knudsen effusion mass spectrometry. *Goldschmidt*. 2021.
279. Bischof L, Sossi PA, Sergeev D, Müller M, Schmidt MW. Quantification of thermodynamic properties for vaporisation reactions above solid Ga_2O_3 and In_2O_3 by Knudsen effusion mass spectrometry. *CAL*. 2023;80:102507. doi:10.1016/j.calphad.2022.102507
280. Farley KA, Hurowitz JA, Asimow PD, Jacobson NS, Cartwright JA. A double-spike method for K–Ar measurement: a technique for high precision in situ dating on Mars and other planetary surfaces. *Geochim Cosmochim Acta*. 2013;110(0):1-12. doi:10.1016/j.gca.2013.02.010
281. Costa GC, Jacobson NS, Fegley B Jr. Vaporization and thermodynamics of forsterite-rich olivine and some implications for silicate atmospheres of hot rocky exoplanets. *Icarus*. 2017;289:42-55. doi:10.1016/j.icarus.2017.02.006
282. Schaefer L, Fegley B. Chemistry of silicate atmospheres of evaporating super-earths. *Astrophys J Lett*. 2009;703(2):L113-L117. doi:10.1088/0004-637X/703/2/L113
283. Miller M, Armatys K. Twenty years of Knudsen effusion mass spectrometry: studies performed in the period 1990-2010. *Open Thermodyn J*. 2013;7(1):2-9. doi:10.2174/1874396X01307010002
284. Piro MH. *Advances in Nuclear Fuel Chemistry*. Woodhead Publishing; 2020.
285. Mathew MD. Nuclear energy: a pathway towards mitigation of global warming. *Prog Nucl Energ*. 2022;143:104080. doi:10.1016/j.pnucene.2021.104080

286. Marques AC, Junqueira TM. European energy transition: decomposing the performance of nuclear power. *Energy*. 2022;245:123244. doi:10.1016/j.energy.2022.123244
287. Ruth TJ. The shortage of technetium-99m and possible solutions. *Annu Rev Nucl Part S*. 2020;70:77-94.
288. https://www.iaea.org/sites/default/files/gc/gc66-inf4.pdf (Accessed Jan 29, 2024).
289. Tosolin A, Beneš O, Colle J-Y, Souček P, Luzzi L, Konings RJM. Vaporization behaviour of the molten salt fast reactor fuel: the LiF-ThF_4-UF_4 system. *J Nucl Mater*. 2018;508:319-328. doi:10.1016/j.jnucmat.2018.05.049
290. Tosolin A, Vigier JF, Mastromarino S, Konings RJ, Luzzi L, Beneš O. Experimental investigation and thermodynamic modelling of the ThF_4-PuF_3 phase diagram. *J Nucl Mater*. 2023;587:154682. doi:10.1016/j.jnucmat.2023.154682
291. Vozárová N, Smith A, Colle J-Y, et al. Thermodynamic determination and assessment of the CsF-ThF4 system. *J Chem Thermodyn*. 2017;114:71-82. doi:10.1016/j.jct.2017.05.008
292. Capelli E, Beneš O, Colle J-Y, Konings RJM. Determination of the thermodynamic activities of LiF and ThF_4 in the $Li_xTh_{1-x}F_{4-3x}$ liquid solution by Knudsen effusion mass spectrometry. *Phys Chem-Chem Phys*. 2015;17(44):30110-30118. doi:10.1039/C5CP04777C
293. Mishra R. Measurement of thermodynamic activities of LiF, NaF and KF in molten FLiNaK. In: *Proceedings of the thirty second ISMAS symposium on mass spectrometry*; 2019.
294. McMurray JW, McAlister A, Mcfarlane J, Kurley JM III. *Thermal analysis of non-actinide bearing salt*. Oak Ridge National Lab.(ORNL); 2020.
295. Beneš O, Capelli E, Morelová N, et al. Cesium and iodine release from fluoride-based molten salt reactor fuel. *Phys Chem-Chem Phys*. 2021;23(15):9512-9523. doi:10.1039/D0CP05794K
296. Taira M, Arita Y, Yamawaki M. The evaporation behavior of volatile fission products in FLiNaK salt. *Open Access J Sci Tech*. 2017;5(5):1-17. doi:10.11131/2017/101315
297. Hania PR, Boomstra DA, Beneš O, et al. SaLIENT-01: preparation and start of irradiation of thorium-bearing molten fluoride salt in graphite crucibles. In: *Proc. Int. Nuclear Fuel Cycle Conf. and TOP FUEL 2019—Light Water Reactor Fuel Performance Conf*; 2020:22-27.
298. Luongo A, Brunetti B, Vecchio Ciprioti S, Ciccioli A, Latini A. Thermodynamic and kinetic aspects of formamidinium lead iodide thermal decomposition. *J Phys Chem C*. 2021;125(40):21851-21861. doi:10.1021/acs.jpcc.1c06729
299. Trinadh V, Manikandan P, Bera S, Rao CB, Narasimhan TL. Thermodynamic properties over < UAl_2(cr)+ U (cr)> two phase region of U-Al system: Knudsen effusion mass spectrometric study. *J Nucl Mater*. 2022;563:153649. doi:10.1016/j.jnucmat.2022.153649
300. Bera S, Trinadh V, Manikandan P, Narasimhan TL, Ananthasivan K, Joseph M. Knudsen effusion mass spectrometric studies on U-Al system: thermodynamic properties over (UAl_2+ UAl_3) biphasic region. *J Nucl Mater*. 2018;509:613-619. doi:10.1016/j.jnucmat.2018.07.028
301. Trinadh V, Manikandan P, Bera S, et al. Thermophysical and thermochemical properties of U-23wt.% Pu-6wt.% Zr alloy fuel: computational and high temperature mass spectrometric studies. *J Nucl Mater*. 2020;539:152251. doi:10.1016/j.jnucmat.2020.152251
302. Trinadh V, Manikandan P, Rao CB, Narasimhan TL. Thermodynamic properties over < $GdAl_2$(cr)+ GdAl (cr)> two phase region of Gd–Al system: Knudsen effusion mass spectrometric study. *J Chem Thermodyn*. 2021;161:106518. doi:10.1016/j.jct.2021.106518
303. Gotcu-Freis P, Colle J-Y, Hiernaut J-P, Konings RJM. (solid+ gas) equilibrium studies for neptunium dioxide. *J Chem Thermodyn*. 2011;43(3):492-498. doi:10.1016/j.jct.2010.10.027
304. Smith A, Colle J-Y, Beneš O, Konings RJM, Sundman B, Guéneau C. Thermodynamic assessment of the neptunium–oxygen system: mass spectrometric studies and thermodynamic modelling. *J Chem Thermodyn*. 2016;103:257-275. doi:10.1016/j.jct.2016.07.040
305. Vorozhtcov VA, Stolyarova VL, Shilov AL, Lopatin SI, Shugurov SM, Karachevtsev FN. Thermodynamics and vaporization of the Sm_2O_3–ZrO_2 system studied by Knudsen effusion mass spectrometry. *J Phys Chem Solid*. 2021;156:110156. doi:10.1016/j.jpcs.2021.110156
306. Stolyarova VL, Vorozhtcov VA, Masaki K, Costa D. High-temperature mass spectrometric study of thermodynamic properties in the UO_2–ZrO_2 system. *Rapid Commun Mass Spectrom*. 2020;34(19):e8862. doi:10.1002/rcm.8862
307. Stolyarova VL, Vorozhtcov VA, Lopatin SI, Shugurov SM, Shilov AL, Karachevtsev FN. Mass spectrometric study of ceramics in the Sm_2O_3-ZrO_2-HfO_2 system at high temperatures. *Rapid Commun Mass Spectrom*. 2021;35(9):e9066. doi:10.1002/rcm.9066
308. Nakajima K, Takai T, Furukawa T, Osaka M. Thermodynamic study of gaseous $CsBO_2$ by Knudsen effusion mass spectrometry. *J Nucl Mater*. 2017;491:183-189. doi:10.1016/j.jnucmat.2017.05.001
309. Braun J, Guéneau C, Alpettaz T, et al. Chemical compatibility between UO_2 fuel and SiC cladding for LWRs. Application to ATF (accident-tolerant fuels). *J Nucl Mater*. 2017;487:380-395. doi:10.1016/j.jnucmat.2017.02.031
310. Trinadh V, Manikandan P, Jain A, Narasimhan TL, Ananthasivan K. Vaporisation studies on Sn-Te-O system by Knudsen effusion mass spectrometry: thermodynamic properties over (SnO_2 + $SnTe_3O_8$) biphasic region. *CAL*. 2019;64:347-353. doi:10.1016/j.calphad.2019.01.008
311. Manikandan P, Trinadh V, Bera S, et al. Knudsen effusion mass spectrometric studies over (U_3Sn_7+ USn_3) phase region of U-Sn system. In: *Proceedings of the Thirty First ISMAS Symposium on Mass Spectrometry*. Vol.491; 2017:31-36. doi:10.1016/j.jnucmat.2017.04.024
312. Stolyarova ALS VL, Sokolova TV, Kurata M, Costa D. Thermodynamics and vapourization of Cs-, Sr-, Ba-containing systems valid for nuclear safety problems. *Russ Chem Rev*. 2023;92(5):92. doi:10.57634/RCR5059
313. Colle J-Y, Wiss T, Dieste O, et al. Comparative study of fission product release of homogeneous and heterogeneous high-burn up MOX fuel by Knudsen effusion mass spectrometry supported by EPMA, SEM/TEM and thermal diffusivity investigations. *J Nucl Mater*. 2023;578:154340. doi:10.1016/j.jnucmat.2023.154340
314. Talip Z, Wiss T, Maugeri E-A, et al. Helium behaviour in stoichiometric and hyper-stoichiometric UO_2. *J Eur Ceram Soc*. 2014;34(5):1265-1277. doi:10.1016/j.jeurceramsoc.2013.11.032
315. Talip Z, Wiss T, Janssen A, Colle J-Y, Somers J, Konings RJM. The dissolution of helium in La-doped UO_2 as a surrogate of hypo-stoichiometric UO_2. *Nucl Mater Energy*. 2015;3:12-16. doi:10.1016/j.nme.2015.01.002
316. Luzzi L, Cognini L, Pizzocri D, et al. Helium diffusivity in oxide nuclear fuel: critical data analysis and new correlations. *Nucl Eng Des*. 2018;330:265-271. doi:10.1016/j.nucengdes.2018.01.044
317. Hilpert K, Gerads H, Kobertz D. Sorption of strontium by graphitic materials. *Ber Bunsen Phys Chem*. 1985;89(1):43-48. doi:10.1002/bbpc.19850890110
318. Hilpert K, Gerads H, Kath D, Kobertz D. Sorption of cesium and its vaporization from graphitic materials at high temperatures. *High Temp-High Press*. 1988;20(2):157-164.
319. Walton KL, Jacobson NS, Kowalski BA, Brockman JD, Loyalka SK. Sorption isosteres and isotherms of silver on NBG-17 graphite. *J Nucl Mater*. 2021;557:153264. doi:10.1016/j.jnucmat.2021.153264
320. Booth A, Markus T, Mcfiggans G, Percival C, Mcgillen M, Topping D. Design and construction of a simple Knudsen effusion mass spectrometer (KEMS) system for vapour pressure measurements of low volatility organics. *Atmos Meas Tech*. 2009;2(2):355-361. doi:10.5194/amt-2-355-2009

321. Kudin LS, Dunaev AM, Motalov VB, Cavallo L, Minenkov Y. Thermochemistry of 5, 10, 15, 20-tetraphenylporphyrin. *J Chem Thermodyn*. 2020;151:106244. doi:10.1016/j.jct.2020.106244
322. Booth AM, Bannan TJ, Benyezzar M, et al. Development of lithium attachment mass spectrometry—Knudsen effusion and chemical ionisation mass spectrometry (KEMS, CIMS). *Analyst*. 2017;142(19):3666-3673. doi:10.1039/C7AN01161J
323. Blanquet E. Thermodynamics simulations applied to gas-sold materials fabrication processes. In: Morales-Rodriguez R, ed. *Thermodynamics—Fundamentals and its Application in Science*. InTech; 2012:191-214. doi:10.5772/51377
324. Violet P, Nuta I, Chatillon C, Blanquet E. Cracking study of pentakis (dimethylamino) tantalum vapors by Knudsen cell mass spectrometry. *Rapid Commun Mass Spectrom*. 2010;24(20):2949-2956. doi:10.1002/rcm.4727
325. Henriques D, Motalov V, Bencze L, Fürtauer S, Flandorfer H, Markus T. Experimental thermodynamic study of the Cu-Li-Sn system by Knudsen effusion mass spectrometry. *J Alloys Compd*. 2016;687:306-311. doi:10.1016/j.jallcom.2016.06.091
326. Henriques D, Motalov V, Bencze L, Fürtauer S, Markus T. Experimental thermodynamics of the Li–Sn system by Knudsen effusion mass spectrometry. *J Alloys Compd*. 2014;585:299-306. doi:10.1016/j.jallcom.2013.09.010

How to cite this article: Jacobson NS, Colle J-Y, Stolyarova V, Markus T, Nuta I. Knudsen effusion mass spectrometry: Current and future approaches. *Rapid Commun Mass Spectrom*. 2024;38(14):e9744. doi:10.1002/rcm.9744